LA-UR 99-424

Title:

SUPERCONDUCTIVITY PROGRAM FOR ELECTRIC SYSTEMS/SUPERCONDUCTIVITY TECHNOLOGY CENTER/LANL - ANNUAL PROGRESS REPORT FOR FISCAL YEAR 1997

Author(s):

Dean E. Peterson, MST-STC
Jeffrey O. Willis, MST-STC
Brian E. Newnam, MST-STC

MASTER

Submitted to:

USDOE, EERE, Office of Utility Technologies

DISTRIBUTION OF THIS DOCUMENT IS UNLIMITED

Los Alamos
NATIONAL LABORATORY

DISCLAIMER

Superconductivity Program for Electric Systems

Superconductivity Technology Center
Los Alamos National Laboratory

Annual Progress Report for Fiscal Year 1997

Dean E. Peterson, Center Director and Program Manager
Jeffrey O. Willis and Brian E. Newnam, Editors

Contributors:

P.N. Arendt
J.F. Bingert
B.L. Bingham
H.J. Boenig
L.N. Bulaevskii
J.C. Cooley
[+]D.L. Cottrell
J.Y. Coulter
[*]W. Dai
D.E. Daney
M.A. Daugherty
R. DePaula
P.C. Dowden
[+]T.H. Falconer
M. Fitzgerald
[†]S. Fleshler
S.R. Foltyn
J.R. Groves
[§]R. Hammond
D.D. Hill
T.G. Holesinger
Q.X. Jia
W.L.Hults
[†]Q. Li
M.P. Maley
[†]A.P. Malozemoff
[*]K. Marken
M.C. Martinez
D.D. Padilla
D.E. Peterson
E.J. Peterson
F.C. Prenger
[†]G.N. Riley, Jr.
J.M. Roper
E.W. Roth
[†]M.W. Rupich
[¶]H. Safar
[+]J.A. Selvaggi
J.L. Smith
[†]M. Teplitsky
N.V. Vo
[§]C. Wang
J.O. Willis
L.A. Worl
Y.T. Zhu

[†]American Superconductor Corporation
[+]Eriez Magnetics
[*]Oxford Superconducting Technology
[#]Pirelli Cable
[§]Stanford University
[¶]University of Illinois-Chicago

Work supported by the
United States Department of Energy
Office of Energy Efficiency and Renewable Energy /
Office of Utility Technologies

STC
Superconductivity Technology Center

Los Alamos
NATIONAL LABORATORY

Foreward

The goal of the Superconductivity Technology Center (STC) at Los Alamos National Laboratory is to support development of electric power applications of High-Temperature Superconductors (HTS). Our industrial partnerships, established through cooperative research and development agreements (CRADA), have accelerated progress towards demonstrating the practical HTS tapes and prototype devices. These collaborative efforts have included studies of both first-generation BSCCO oxide-powder-in-tube (OPIT) tapes as well as second-generation YBCO coated conductors. Los Alamos has made major contributions during this review period in Superconducting Partnership Initiative (SPI) projects to develop HTS fault current limiters and power transmission cables as well as demonstrating magnetic separators based on HTS magnets. The combination of the extensive technical expertise and facilities at Los Alamos with the marketing insights and engineering abilities of our industrial partners has advanced possible HTS applications. These partnerships serve as excellent models for future government-industry interactions.

Dean E. Peterson, Leader

Superconductivity Technology Center

Table of Contents

List of Figures

List of Tables

Glossary of Acronyms

ANL	Argonne National Laboratory
ASC	American Superconductivity Corporation
BEI	Backscatter Electron Imaging
Bi-2212	$Bi_2Sr_2CaCu_2O_8$
Bi-2223	$(Bi,Pb)_2Sr_2Ca_2Cu_3O_8$
BNL	Brookhaven National Laboratory
BSCCO	Forms of BiSrCaCuO
EBPS	Electron Back-Scattered Patterns
FCL	Fault Current Limiter
HGMS	High-Gradient Magnetic Separator
HTS	High-Temperature Superconductivity
IBAD	Ion Beam-Assisted Deposition
IGC	Intermagnetics General Corporation
IMP	Isothermal Melt Processing
I_c	Critical current for superconductivity, A
J_c	Critical current density for superconductivity, A/cm^2
LANL	Los Alamos National Laboratory
3M	Minnesota Mining and Manufacturing, Inc.
ORNL	Oak Ridge National Laboratory
OSTI	Oxford Superconductivity Technology, Inc.
PLD	Pulsed-Laser Deposition
PMC	Prototype Multi-Strand Cable
RBS	Rutherford Backscattering Spectroscopy
RHEED	Reflection High-Energy Electron Diffraction
SCE	Southern California Edison
SEM	Scanning Electron Microscopy
SNL	Sandia National Laboratories
SPI	Superconductivity Partnership Initiative
STC	Superconductivity Technology Center (Los Alamos)
T_c	Critical temperature for superconductivity, degrees K
TEM	Transmission Electron Microscopy
XRD	X-Ray Diffraction
YBCO	$YBa_2Cu_3O_{7-\delta}$
YSZ	Yttria-Stabilized Zirconia

1. Introduction

Development of high-temperature superconductors (HTS) has undergone tremendous progress during the past year. Kilometer tape lengths and associated magnets based on BSCCO materials are now commercially available from several industrial partners. Superconducting properties in the exciting YBCO coated conductors continue to be improved over longer lengths. Our SPI projects to develop HTS fault current limiters and transmission cables have demonstrated that HTS prototype applications can be produced successfully with properties appropriate for commercial applications. Research and development activities at LANL related to the HTS program for Fiscal year 1997 are collected in this report.

LANL continues to support further development of Bi2223 and Bi2212 tapes in collaboration with American Superconductor Corporation (ASC) and Oxford Superconductivity Technology, Inc. (OSTI), respectively. Our tape processing studies involving novel thermal treatments and microstructural characterization have assisted these companies in commercializing these materials. Our research on second-generation YBCO-coated conductors produced by pulsed-laser deposition (PLD) over buffer template layers produced by ion beam-assisted deposition (IBAD) continues to lead the world. Our applied physics studies of magnetic flux pinning by proton and heavy ion bombardment of BSCCO and YBCO tapes have provided many insights into improving the behavior of these materials in magnetic fields.

Sections 4 to 7 of this report contain a list of 29 refereed publications and 15 conference abstracts, a list of patent and license activities, and a comprehensive list of collaborative agreements in progress and completed.

2. Highlights of Fiscal Year 1997

- *We report the first successful efforts in the U.S. to produce high-I_c and high-J_c YBCO coated conductors by a scaleable process. A 12-cm-long tape section with an I_c of 80 A and an average J_c of 0.8 MA/cm^2 was fabricated on Hastelloy using pulsed-laser (PLD) and ion-beam-assisted deposition (IBAD) techniques.*

- *High-rate (>100 Å/s) deposition of YBCO films with PLD was demonstrated with some degradation of J_c. High-temperature annealing recovered most of this loss, suggesting the limitation is caused by cation disorder.*

- *Pulsed-laser deposition of YBCO on Hastelloy substrates with an MgO template film produced at Stanford University and suitable buffer layers resulted in critical current density J_c values in the 200-400 kA/cm^2 range.*

- *The use of heavy-ion and high-energy proton irradiations to create pinning sites in YBCO coated conductors was evaluated. Thicker films exhibited a peak along the c axis that resulted in stronger high-field performance for H||c. Heavy ion irradiation resulted in strong enhancements of J_c for the field along the direction of irradiation. High-energy protons produced splayed columnar defects that enhanced performance with near isotropy of J_c in an applied field.*

- *Isothermal melt processing led to less bubbling and improved microstructures in Bi-2212 multifilament tapes, and therefore very good J_c characteristics, because of shorter process times and lower temperatures than can be used in conventional processes.*

- *High-resolution transmission electron microscopy of high-J_c Bi-2223/Ag sheathed tapes revealed many details of the microstructure from dense, well-aligned grains near the silver interface to more porous, less-aligned grains in the middle of the filaments. Also evident were dislocations within grains, permitting grain bending, and the structure of colony boundaries.*

- *Electron Back-Scattered Patterns (EBPS) measured in the scanning electron microscope on commercial Bi-2223/Ag multifilament tape permitted mapping of the grain-to-grain orientation and the determination of in-plane texture, which was observed near the edges of some filaments.*

- *The efficacy of high-energy proton-induced fissions to produce flux pinning near the splayed columnar defects was investigated by irradiations of Bi-2223/Ag multi- and monofilament tapes, YBCO coated conductors, and a Bi-2223/Ag pancake coil.*

- *Tests of two prototype multistrand conductors produced by ASC were successfully completed, including dc critical current, ac loss for two different 3-phase conductor spacings at currents up to 1100 A rms, and the axial magnetic field variation along the conductor.*

- *Pulsed and dc tests of a pre-prototype superconducting coil for the 500-MVA Superconducting Fault Current Limiter SPI demonstrated transient redistribution of current within the inner and outer windings in agreement with predictions of the electrical and thermal model.*

- *Our cryocooled HTS High-Gradient Magnetic Separator system successfully separated uranium from a water solution and from a simulated soil containing water and kaolin clay. Concentrations dropped from 200 or 400 ppm for the two solutions, respectively, to near the detection limit of 1 ppm after one pass.*

3. Technical Activities

3.1 Wire Technology

3.1.1 Ion Beam-Assisted Template Films

(P.N. Arendt, J.R. Groves, J.M. Roper, and R.F. DePaula)

Deposition of IBAD films requires a balance between the vapor and ion fluences at the substrate. Heretofore, the ion fluence was limited because the linear ion-assist gun was operated near its Child-Langmuir limit. That is, for a fixed assist-beam voltage, current density J is limited by the gun optics and voltage V according to the Child-Langmuir relationship as $J \propto V^{3/2}$. During this year, we established new deposition parameters where the assist gun operating voltage was increased which, in turn, allowed higher ion (and vapor) fluences at the substrate. The net effect was that the IBAD film deposition rate increased by 75%. A side benefit of operating in this higher assist-gun-voltage regime is that the frequency of maintenance operations, e.g. plasma discharge filament replacements, is reduced.

The nickel alloy substrates used for the YBCO tape program had poor as-received surface finishes with typical surfaces roughness of 300 to 500 nm rms. Improving the finish of these surfaces was necessary to improve the in-plane texture of the IBAD yttria-stabilized zirconia (YSZ) buffer layer and subsequent overcoated YBCO films. A fixture was designed and built to polish 1.1-meter-long by 1-cm-wide substrates. The fixture accommodated substrate tapes with thicknesses varying from 25 to 125 µm. After polishing, the surface roughness of the tape surfaces was reduced to 15 to 20 nm rms. Subsequent IBAD YSZ films deposited on these tape surfaces had in-plane mosaic spreads as low as those obtainable with films deposited on polished single-crystal silicon, i.e., <12°.

Recent YSZ IBAD films made using the linear assist gun had x-ray ϕ-scan values under 13° FWHM over tape lengths of 15 cm. In turn, this resulted in high quality overcoated YBCO films that had critical currents of 60 A (75 K) over a 12-cm length as described in the next section of this report.

Finally, a vacuum chamber was modified to perform continuous magnetron sputter deposition coatings onto tapes up to 1.1 m in length. This capability may be used to sputter metal oxide buffer layers onto the IBAD YSZ films or silver overlayers onto the YBCO films for making low-resistivity electrical contact to the superconductor films.

A tape drive was designed, built, and installed in the 23-cm linear IBAD system. This drive can accommodate two, 1-cm-wide by 1.1-m-long tapes. The tapes are spot welded together into loops so that multiple passes in the IBAD zone may be done during a deposition run. This results in very uniform film texture along the entire 1.1-m length of tape. Such film uniformity is vital for the optimization of subsequent deposition processing steps in the fabrication of YBCO coated conductors. To date, our best films have an in-plane mosaic spread of 20° FWHM as measured by x-ray φ scan. Further optimization of the tape drive system is being undertaken in order to reduce the amount of in-plane rotated crystals. This optimization consists of shielding experiments to ensure that cubic zirconia vapor is not deposited in regions where the ion-assist beam can not orient the film.

A second linear ion-assist system was brought on line during this year. It consisted of a 50-cm linear assist gun and a 16-cm-diameter rf ion sputter gun. Early experiments yielded poor in-plane alignment of the films. Several first-order improvements were made to this system to get the alignment to be equal to that obtained in our smaller 23-cm system. When this system became operational, our capacity for providing IBAD films increased by approximately a factor of five.

Because of expansion of other programs at the STC, the silver tape coater had to be relocated into the thick films deposition lab. Approximately two man weeks of effort were involved in this effort. The small-area sputter deposition system was also moved to a new area in the thick films lab to accommodate a new box coater that was received from 3M Corporation. This move is not complete pending installation of new utilities to accommodate both of the latter systems. The 3M Corp. also lent us a large area (5" x 12" [~13 x 31 cm]) rectangular sputter-deposition gun and a 1-kW rf supply to power the gun. We also received a 23-cm linear ion gun and associated power supply. These were used in the large IBAD system as a vapor source in conjunction with the 50-cm assist gun.

A main program focus has been to supply 1-cm wide by 1.1-m-long tapes with IBAD YSZ template films for subsequent deposition of buffer layer and HTS YBCO films in the PLD laboratory. These 1.1-m tapes, as well as shorter sections of tapes, were used in the core program and also by the LANL CRADA partners. For these 1.1-m tapes, there was limited success in obtaining YSZ films with in-plane FWHM texture much less than 20°. However, with non-moving tapes of lengths ~20 cm, in-plane FWHM values <15° were readily obtained. Experiments indicated that the problem with coating the moving tapes occurred at the edges of the shield that separated the coating region from the non-coating region of the tapes. It was found that the vapor plume extended a short distance beyond the shield edge, whereas the ion-assist beam did not extend beyond this edge. This non-assisted vapor was suspected to be a major reason for the fundamental limitation seen to date on the moving template films in-plane texture. Subsequently, the shield edges were modified appropriately to eliminate this non-assisted vapor and the quality of the template texture on the longer, moving tapes was improved.

The remaining activities in the IBAD template film laboratories involved work for our various CRADA commitments. The following non-proprietary activities are related to equipment improvement issues.

The silver tape coater in the thick films deposition lab was modified to include the capability to coat intermediate buffer layers on the IBAD tapes. This capability is needed for one of the CRADAs. This upgrade is scheduled to be finished early in the next reporting period.

The 16-cm-diameter rf ion sputter gun in the second linear IBAD system was replaced with the 23-cm linear ion gun and associated power supply. Replacing the microwave cavity driven rf ion gun with the filament driven linear gun allows the system to operate at greatly reduced pressures, which should improve the ultimate quality of the in-plane texture of the IBAD films made in this system. Several modifications had to be made to this gun and its power supply to allow it to operate in this deposition system.

A large fraction of the activities in the IBAD template film laboratories involved work for the 3M and American Superconductor CRADA commitments.

Core program and nonproprietary activities were as follows. Design modifications for the IBAD deposition augmented with an in-situ reflection high-energy electron diffraction (RHEED) monitoring system were completed. This system utilizes a box coater supplied to LANL by 3M Corporation. Components were installed in the system as completed by the machine shops. New equipment needed to complete the system will be ordered early in FY98, and the first film depositions with this system are planned for mid-December, 1998.

3.1.2 YBCO Coated Conductors: High-Rate Deposition and Annealing

(S.R. Foltyn and P.C. Dowden)

During the past year, we continued to optimize long tapes (10-20 cm) that were coated first with a textured YSZ layer by IBAD (using a 20-cm linear ion-assist gun) and then with YBCO. The superconductor coating is applied by PLD as the tape moves over a heated roller in a system capable of coating a continuous loop up to 115 cm long. For the optimization runs described here, we have been using the 20-cm IBAD-coated lengths (sometimes cut in half) spot-welded to a longer length of bare tape to complete the loop. The substrate tape material used in these tests was either Inconel 600 (50 µm thick) or Inconel 625 (100 µm thick); the widths of the tapes were all 1 cm.

In early trials of the YBCO tape-coating system, J_c values of up to 380 kA/cm^2 were achieved on 5-mm-long bridges, with micrometer-thick films. These values were consistent with, and even exceeded, what would be obtained for conventionally coated, i.e., glued to a stationary heater, samples with the same degree of YBCO alignment. However, the best J_c for a longer length of 7 cm was ~100 kA/cm^2. Since there was a considerable difference between the best J_c values for short bridges and the J_c for long lengths, a 20-cm-long tape was coated and then cut into 1-cm lengths for detailed analysis. The results are shown in Fig. 1. Each 1-cm x 1-cm sample was patterned to bridge dimensions of ~1 mm wide x 5 mm long; average film thickness was 1.2 µm. There were fewer than 20 samples because the spot-welded joint at each end consumed some of the tape. As the figure shows, the measured J_c ranged from ~30 to 300 kA/cm^2: Assuming that 30 kA/cm^2 is the limiting J_c for current through the entire tape length, then I_c would be only 3.6 A. Alternately, if each segment had the tape's average J_c of 150 kA/cm^2, I_c would be 18 A. This illustrates the importance of improving J_c uniformity – all segments are in series, and the poorest one controls the performance of the entire tape.

To attempt to determine the cause of the low J_c values in segments 10-13, the texture of each sample was measured, with results shown in Fig. 2. The YSZ (111) FWHM ranged from 16° to 26° (the variation is attributable to roll-off of vapor flux and assist beam current at the ends of the tape) with, as usual, the YBCO alignment being 5° to 6° better. Overlaying the YBCO texture with the J_c values (Fig. 3) showed that a weak correlation existed between the two. However, the minor FWHM increase in segments 10-13 was not enough to cause the dramatic drop in J_c for these segments, nor could texture have been responsible for the low J_c values of segments 17 and 18 with respect to adjoining segments.

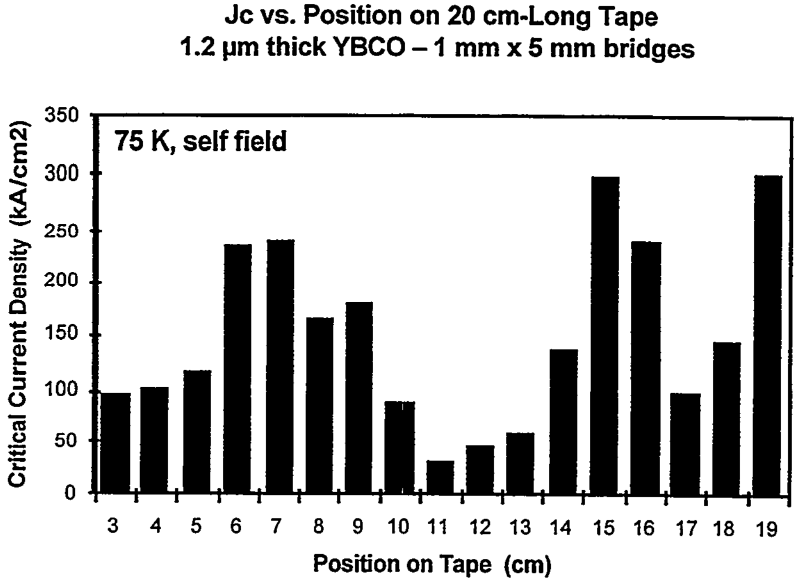

Figure 1. Critical current density as a function of position along a 20-cm YBCO tape.

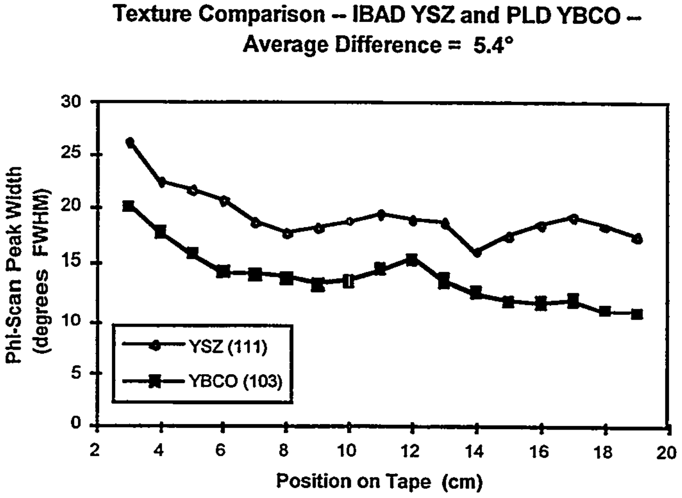

Figure 2. Comparison of texture of the IBAD YSZ buffer layer and the PLD YBCO layer. Average difference is 5.4°.

If the 10x J_c variations cannot be explained by differences in texture, then another possibility is that the temperature of the tape as it moved over the roller was not constant during the YBCO deposition step. To check this, resistive transition temperatures of each patterned sample were measured. This was considered a valid test because both T_c and J_c depend upon deposition temperature in the same way. Deposition at substrate temperatures either 25°C above or below the optimum temperature will noticeably degrade T_c and J_c. Transition temperatures are overlaid on the J_c data in Fig. 4. Although the values of T_c are low in general – this is probably the result of a non-optimal O_2 anneal step – there is no correlation between T_c, which is essentially constant, and J_c.

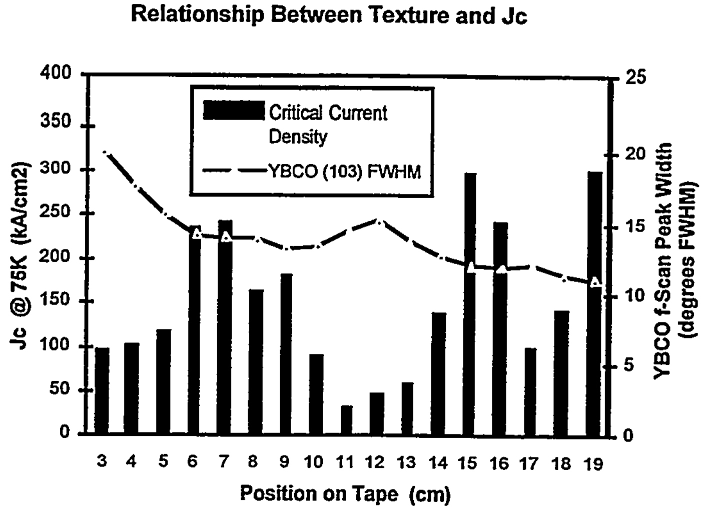

Figure 3. Relationship between J_c and YBCO texture as determined from φ-Scan FWHM as a function of position along the tape.

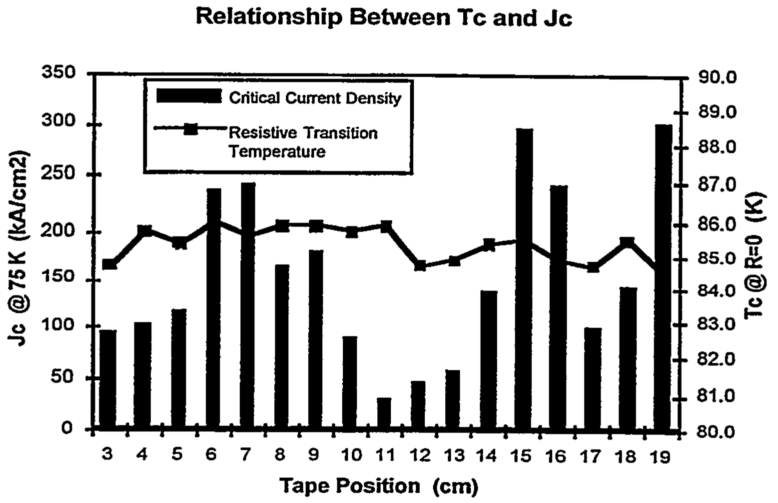

Figure 4. Relationship between T_c and J_c along the length of a 20-cm YBCO tape.

At this point, then, the cause of low J_c in segments 10-13 has not been pinpointed, although texture and temperature control problems have been ruled out.

In an attempt to improve the J_c uniformity without actually knowing the cause of the variations, we made several tapes on which the YBCO was deposited in two passes over the roller. It was thus hoped that the event producing low J_c would not occur at the same place on the tape in the second pass. Initial results were promising: The results for the three tapes produced in this series are shown in Table 1.

Table 1. Critical Current for YBCO Coated Conductors Deposited in Two Passes

Gauge Length (cm)	I_c(A)
7.5	38
6.3	35
12.0	70

The high I_c of the last tape in the table is due partly to an intentional increase in thickness – to 1.7 µm – and partly to very good texture in the IBAD film, and subsequently good alignment in the YBCO; average FWHM angles were 12.1° and 6.8°, respectively. In addition, improvement in the O_2 anneal raised T_c to an average of 87 K. The overall J_c of this tape is over 400 kA/cm^2, and the highest J_c so far for an individual segment is 800 kA/cm^2. These results imply that the 10x variation in J_c reported originally has been reduced to a 2X variation by double-passing the tape.

3.1.3 Continuous Processing of YBCO/IBAD Coated Conductors on Flexible Substrates

(S.R. Foltyn, P.N. Arendt, P.C. Dowden, J.R. Groves, J.Y. Coulter, E.J. Peterson)

A number of groups have produced thick YBCO films capable of carrying over 100 A per centimeter width at 77 K. Our group, for example, has achieved a critical current of nearly 200 A (75 K, self field) on a 1-cm-wide x 4-cm-long Ni-alloy strip. Coatings on this strip consisted of a textured YSZ layer produced by IBAD and a 2-µm-thick YBCO film produced by PLD. The strip was fabricated in a batch process, with both the IBAD and PLD layers coated on stationary substrates, a process not amenable to scaling to long lengths. To demonstrate that high-current coated conductors can be produced in a continuous process, we have developed a system capable of coating meter lengths of 1-cm-wide tape with high-quality YBCO.

For these initial experiments the IBAD layer was not produced continuously, but rather a 21-cm long stationary tape was coated using a 5-cm-diameter ion-beam sputtering source and a 23-cm x 2.5-cm linear ion-assist gun. Significant modifications were required, however, for the YBCO layer, dictated primarily by the need to deposit the superconductor at elevated temperature. Shorter samples can simply be pasted to a heater, but a continuous deposition process requires heating a moving tape to between 700 and 800°C in the area where deposition is occurring. This was accomplished at Fujikura and Sumitomo Electric in Japan by sliding the tape over a heated block. In the present work we describe a different technique, involving deposition on a tape that is both conductively heated and driven by a hot roller. An experimental schematic is shown in Fig. 5. To simplify this prototype, it was configured to coat a continuous loop (as opposed to using reel-to-reel tape transport), and was constructed of standard vacuum hardware with 6-inch flanges. The heater consists of a 2.5-inch (6.3-cm)-diameter nickel disk with a coaxial heating element brazed inside; thermocouple and power leads exit the vacuum chamber through a rotating hollow shaft that is driven by an external stepper motor through a worm gear. The stepper motor speed range provided linear tape speeds of 1 to 24 mm/minute. A 1-µm-thick film could be deposited at 1 cm/minute at relatively low laser power. The target is attached to a magnetically coupled rotating feedthrough that can be translated into a load lock (not shown in Fig. 5) to permit target changes without breaking the main vacuum.

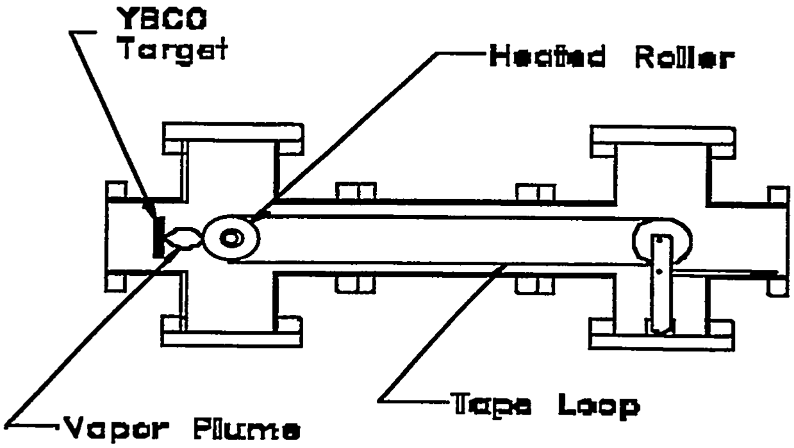

Figure 5. Schematic diagram of continuous-loop tape coater.

During deposition, the typical roller temperature was 840°C, giving a tape temperature – determined separately by a thermocouple spot-welded to a bare tape, or by optical pyrometry during deposition – of ~790°C. The deposition pressure was 0.2 Torr oxygen, and since the tape cools to room temperature as it comes off the roller, a separate anneal at 450°C in 1-atm O_2 was required to convert the YBCO to the superconducting orthorhombic phase. To coat the 21-cm-long tape strip produced with the linear-gun IBAD system, it was spot-welded to a length of bare tape to make up a loop of the proper length. The tape used in this study was Inconel 625 of 100-µm thickness that had been mechanically polished to a rms roughness of 100 Å.

The best result to date from this system is an I_c of 70 A over a 12-cm measurement length. (Some of the original 21-cm length was lost due to spot welding the ends, removal of end pieces after deposition for checking transition temperature (T_c), and attachment of current leads). To prepare the strip for this measurement, it was first coated with 1 µm of silver, which was annealed at 550°C for 30 minutes to improve adhesion and contact resistance. Then current leads and voltage taps were attached with indium solder, and a standard 4-point I-V curve was generated.

To investigate uniformity of electrical properties along the sample length, the silver was then removed from the strip, it was cut into 1-cm lengths, and each segment was patterned into a 0.5-mm x 5-mm bridge for critical current density (J_c) and resistance vs. temperature measurements. X-ray ϕ-scans on both the YSZ (111) and YBCO (103) peaks were also conducted with the results shown in Fig. 6. Because of roll-off of both vapor flux and assist ion current in the IBAD system, the YSZ in-plane alignment was slightly degraded at the tape ends, but is excellent in general. As usual, the YBCO texture was 5-6° sharper than that of the YSZ template; slight deviations may be due to measurement of the YBCO on patterned bridges, while the full area of YSZ, which was not affected by patterning, was available for the x-ray analysis. Figure 7 is a plot of segment-by-segment transport J_c measurements on the microbridges. The YBCO thickness was 1.7 µm. Given the 70-A I_c of the overall tape, the average J_c is somewhat in excess of 400 kA/cm^2, and is indicated by the solid line in Fig. 7. Considerable variation in J_c is evident – the highest segments are in the range of 800 kA/cm^2, while the lowest is 290 kA/cm^2. One question is why the lowest individual J_c is below the average for the tape as a whole. A possible explanation is that of a sampling error: The tape is not perfectly uniform in the lateral direction, and a 0.5-mm-wide bridge is not adequately representative of a 10-mm-wide tape. Nonetheless, the non-random appearance of the variations, i.e., fairly uniform J_c except for the dip in the middle of the tape, suggests that the higher values of J_c are indicative of the potential of this coating process once the cause of the weak areas is identified and removed. If this is the case, then I_c values well in excess of 100 A can be expected.

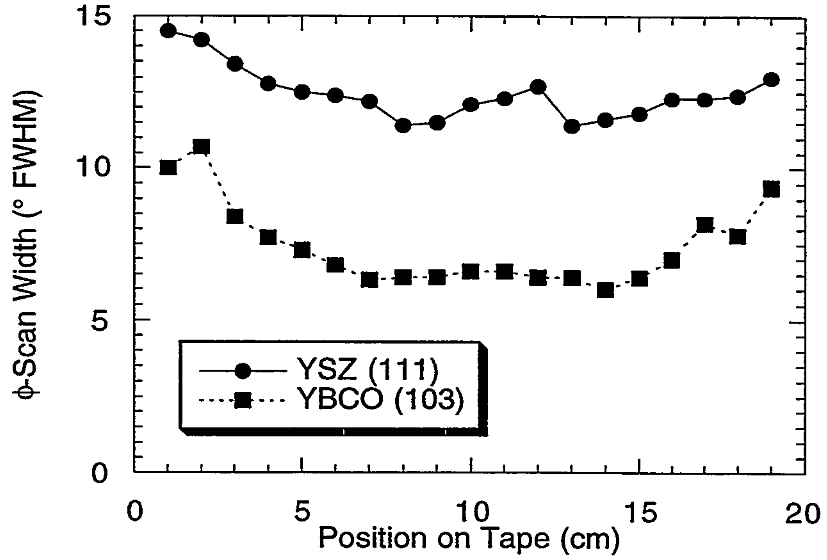

Figure 6. Variation of the in-plane texture along the tape length.

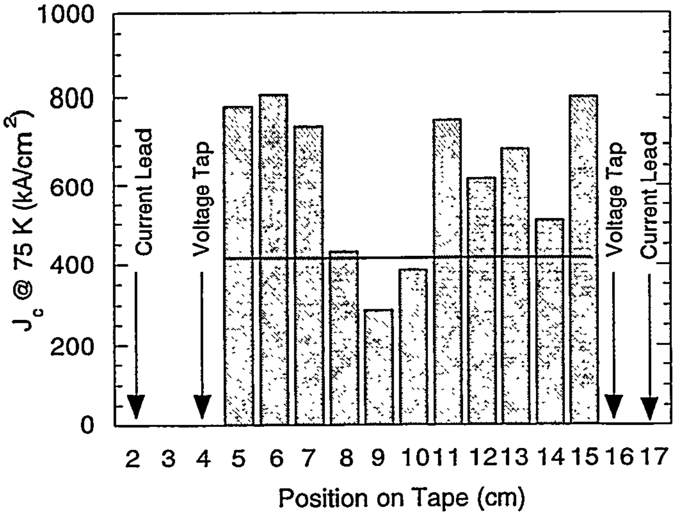

Figure 7. Critical current density for a 12-cm tape with an I_c of 70 A. Bars represent segment by segment J_c, the solid line is the average J_c for the entire tape. Film thickness is 1.7 μm.

The task, then, is to search for and eliminate the cause(s) for J_c reduction in the center of the tape. One obvious possibility is that, because of incomplete contact between roller and tape, the substrate temperature during deposition fell outside of the range necessary for high J_c. This seems unlikely for several reasons, including the uniform appearance of the coating (low temperatures produce black shiny films, while the surface is gray and rough if the temperature is too high). Experiments with a thermocouple spot-welded to a moving tape, which measured temperature variations within ±10°C; and the results shown in Fig. 8, which demonstrate that the lowest J_c segments are not correlated with drops in T_c, as would be the case for deposition outside the optimum temperature range.

Other possible causes for low J_c in segments 8-10 include poor texture (already ruled out in Fig. 6), oxygen deficiency (ruled out by x-ray analysis of c-axis lattice constants), a-axis film growth (ruled out by x-ray θ-scans), cracks (ruled out by SEM examination), and contamination due perhaps to film-substrate interdiffusion. The latter is currently under examination by transmission electron microscopy (TEM), and will also be investigated by surface analysis techniques such as secondary ion mass spectroscopy (SIMS).

In evaluating the change from a batch, paste-up process for YBCO to a continuous one with a moving substrate, it is useful to compare the present results to those achieved previously with pasted substrates. Our group has previously determined from I_c values on 1-cm x 4-cm strips of IBAD-coated Hastelloy indicate that J_c varies with in-plane texture as:

$$J_c(\phi) = 3.25\, e^{-0.23\varphi}\ (\mathrm{MA/cm^2}). \qquad (1)$$

The average YBCO texture over the 12-cm measurement length is 6.9° FWHM, so the expected J_c is 665 kA/cm^2. However, the film thickness in this study was 1 μm, and the thickness for the long tape was 1.7 µm. We also have found that J_c for YBCO on single-crystal YSZ decreases with film thickness as:

$$J_c(t) = 4.7\, e^{-1.2t} + 1.05,\ (\mathrm{MA/cm^2}). \qquad (2)$$

Thus, J_c for a 1.7-µm film should only be 67% of that for a 1-µm film. Therefore, for the same texture and thickness as on the 12-cm tape, we would have expected 450 kA/cm^2 from a batch-processed sample, which compares favorably with the average value of 410 kA/cm^2 that was actually achieved with the continuous process.

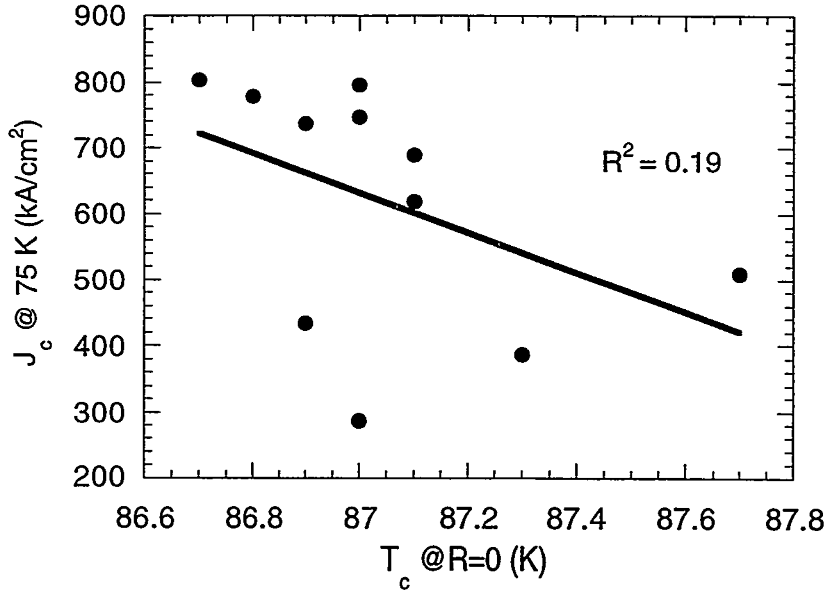

Figure 8. Critical current density as a function of critical temperature for all film segments shown in Fig. 7. R^2 is the least-squares linear-regression coefficient for these data.

In summary, we have demonstrated that the production of high-current YBCO coatings on flexible substrates can be scaled from a batch to a continuous process for the fabrication of long lengths. Future work will center on improving I_c uniformity and developing a continuous IBAD process leading to tape lengths in excess of 1 meter.

3.1.4 Influence of Deposition Rate on the Properties of PLD Thick YBCO Films

(S.R. Foltyn, E.J. Peterson, J.Y. Coulter, P.N. Arendt, Q.X. Jia, P.C. Dowden, M.P. Maley, X.D. Wu, and D.E. Peterson)

We have investigated high-rate deposition of YBCO films which will be required for commercial success. In a recent study, R. Hammond of Stanford University, determined that the minimum requirements for an economically feasible manufacturing process will be a YBCO deposition rate of 100 Å/s, yielding a coating with a critical current density (J_c) of 1 MA/cm^2 for a film thickness of 1 µm.

Previous work performed at the STC in 1990-91 showed that, indeed, YBCO can be laser-deposited at rates up to 145 Å/s while maintaining nearly the same J_c as films deposited at very low rates. However, even though the films in this earlier study were only 0.2 μm thick, channeling-mode Rutherford Backscattering Spectrometry (RBS) revealed a decrease in crystallinity with increasing deposition rate, accompanied by growth of a-axis oriented grains. This suggests that a kinetic limit to epitaxial film growth is being approached. So, we investigated the effect of a possible decreasing crystalline order at higher rates.

As in the earlier study, YBCO films were deposited on $SrTiO_3$ substrates PLD. In the present case, however, the excimer laser wavelength was 248 nm (as opposed to 308 nm), and the film thickness was 1 μm. The deposition rate was varied by adjusting laser pulse repetition frequency from 2 to 100 pulses per second, and was determined by dividing the total film thickness by deposition time. This provided an *average* rate for film deposition, but it must be noted that PLD is characterized by brief periods with extremely high *instantaneous* rates (perhaps 10^4 Å/s) interspersed with periods of 10 - 1000 ms in which no deposition is occurring.

Before beginning the study, several series of films were deposited to optimize substrate temperature, target-substrate distance, and background oxygen pressure. Some compromises were required. For example, as shown in Fig. 9, the highest transition temperature (T_c) was obtained at a substrate temperature of around 840°C, while the highest J_c was achieved at 790°C; the latter was used for these experiments. Critical current density was also found to vary with target-substrate distance (Fig. 10), peaking at 6 cm, and dropping by about 50% at 3.5 cm and 10 cm. However, since the deposition rate was also affected by target-substrate distance – varying as $d^{-1.6}$ – and since high deposition rates were required in this work, a T-S distance of 4 cm was chosen as the best compromise between high rate and high J_c. All films were deposited in 0.2 torr of pure oxygen; the chamber was then backfilled with 250 torr of oxygen and the sample heater turned off. The 5-mm x 10-mm samples were then patterned, yielding bridges 5 mm long and 150-200 μm wide. Evaporated Ag pads were annealed at 550°C for 30 minutes to assure adherence and low contact resistance, and J_c was measured at 75 K, self field, in the usual four-point configuration.

The main results are shown in the lower curve of Fig. 11. Although the data are somewhat scattered, the trend is clear: As the deposition rate was increased from 2 Å/s to over 200 Å/s, J_c dropped by more than a factor of two. For comparison, the earlier results for 0.2-μm films are also plotted in this figure. The offset of the two data series can be attributed to a previously reported decrease in J_c with increasing YBCO film thickness. Interestingly, however, both sets of data have approximately the same negative slope from linear regression analysis; this is in contrast to the conclusions of the earlier work, which suggested that J_c for the thinner films was constant over the range 1 - 145 Å/s. The discrepancy may simply result from the small number of measurements and the more limited range of the earlier set. Nonetheless, the significance of these results – in addition to their obvious relevance to manufacturing economics – is that they may signal a fundamental limit to the rate at which the YBCO structure can be assembled in film form.

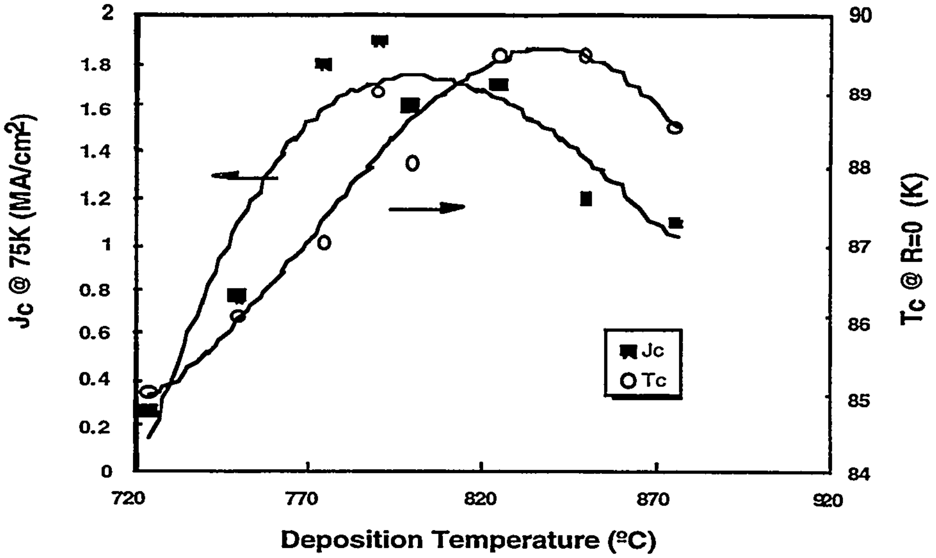

Figure 9. Dependence of the superconducting transition temperature T_c and of the critical current density J_c on the substrate temperature during deposition.

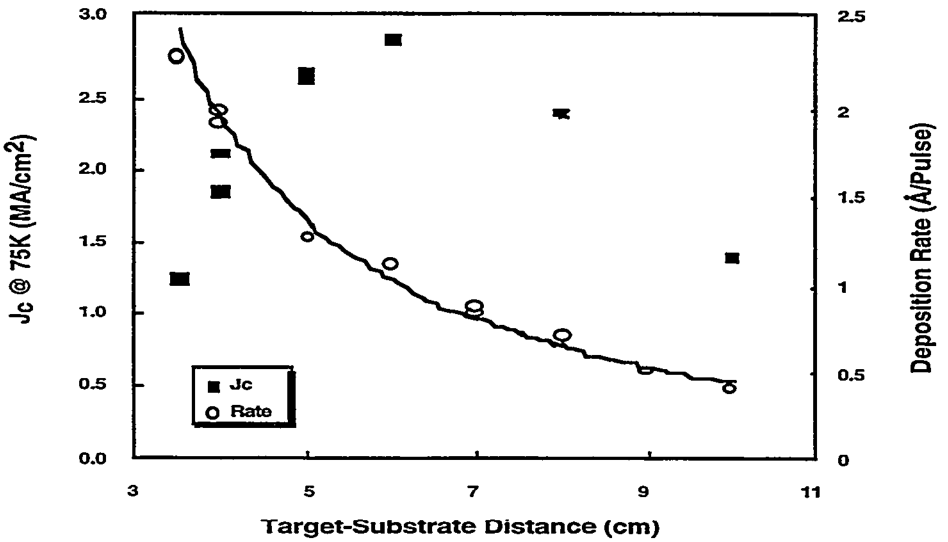

Figure 10. Dependence of the superconducting transition temperature T_c and of the critical current density J_c on the target-to-substrate distance.

In order to investigate the cause for J_c reduction with deposition rate, we considered that at least three basic criteria of high-T_c superconductors must be met to achieve high critical current density: morphology, crystallinity, and stoichiometry. All three aspects of high- and low-rate films from the 1-µm set were studied.

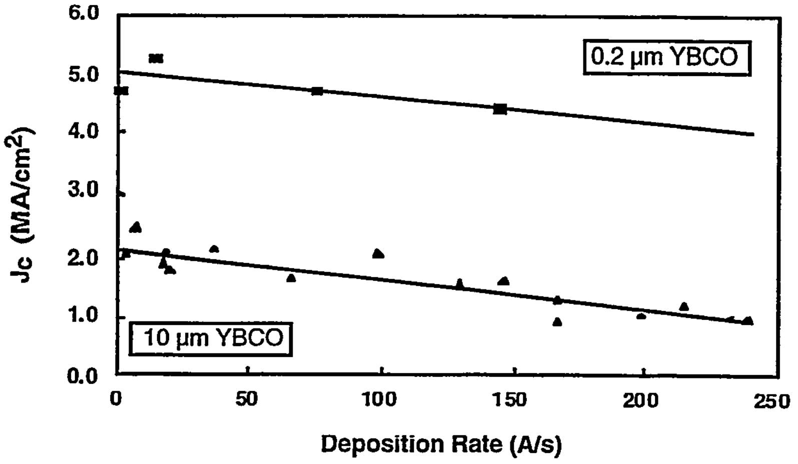

Figure 11. Dependence of critical current density J_c on deposition rate for thin (top) and thick (bottom) films.

The first of these, film morphology, was investigated with scanning electron microscopy, and the results (Fig. 12) were nearly identical to those for the thinner films of the previous work. At low deposition rates of 4 and 8 Å/s the surfaces were characterized by voids between film grains (indicating incomplete coalescence of film grains), while at rates ≥20 Å/s outgrowths became more numerous as deposition rate increased. At 220 Å/s outgrowths covered a large fraction of the surface. At moderate rates, the coating was dense and relatively smooth. This morphological evolution follows from a nucleation and growth model in which the degree of nuclei coalescence depends on both deposition rate and final film thickness. At a constant thickness, low rates result in incomplete coalescence, leaving voids between nuclei. At high rates, outgrowths appear at the triple-points where nuclei have grown together. According to this hypothesis, for each thickness there is an optimum deposition rate for producing a smooth surface: for 0.2-µm films, this rate was found to be 40 Å/s; in the present work with 1-µm films, the rate is 10-20 Å/s. These results are qualitatively consistent with the model, which proposes that a lower deposition rate leads to coalescence at a greater film thickness.

Next, film crystallinity was examined by x-ray diffraction (XRD). The results, shown in Table 2, indicate no significant difference in the crystalline texture of films deposited at 4 Å/s and 220 Å/s. Neither rate produced a measurable a-axis oriented component, the c-axis mosaic spread was the same for both films, and there was only a slight increase in in-plane disorder for the high-rate sample, but not enough to significantly affect J_c according to the rocking curve–J_c correlations we had determined previously.

This brings us to the issue of stoichiometry. Cation ratios in laser-deposited films usually reflect those of the ceramic target, and since the same target, laser energy, and number of laser pulses were used for all films, these ratios were not checked. Unlike the cations, however, oxygen in superconducting films is only partly derived from the target. A background pressure of 100 to 200 millitorr of oxygen is required during deposition to make up for what is lost during target vaporization, but typical deposition conditions (high temperature and low pressure) only yield the oxygen-deficient, nonsuperconducting tetragonal phase of YBCO. To fully oxygenate films they are generally cooled from the deposition temperature in a few hundred torr of oxygen, easily converting them to the superconducting orthorhombic phase.

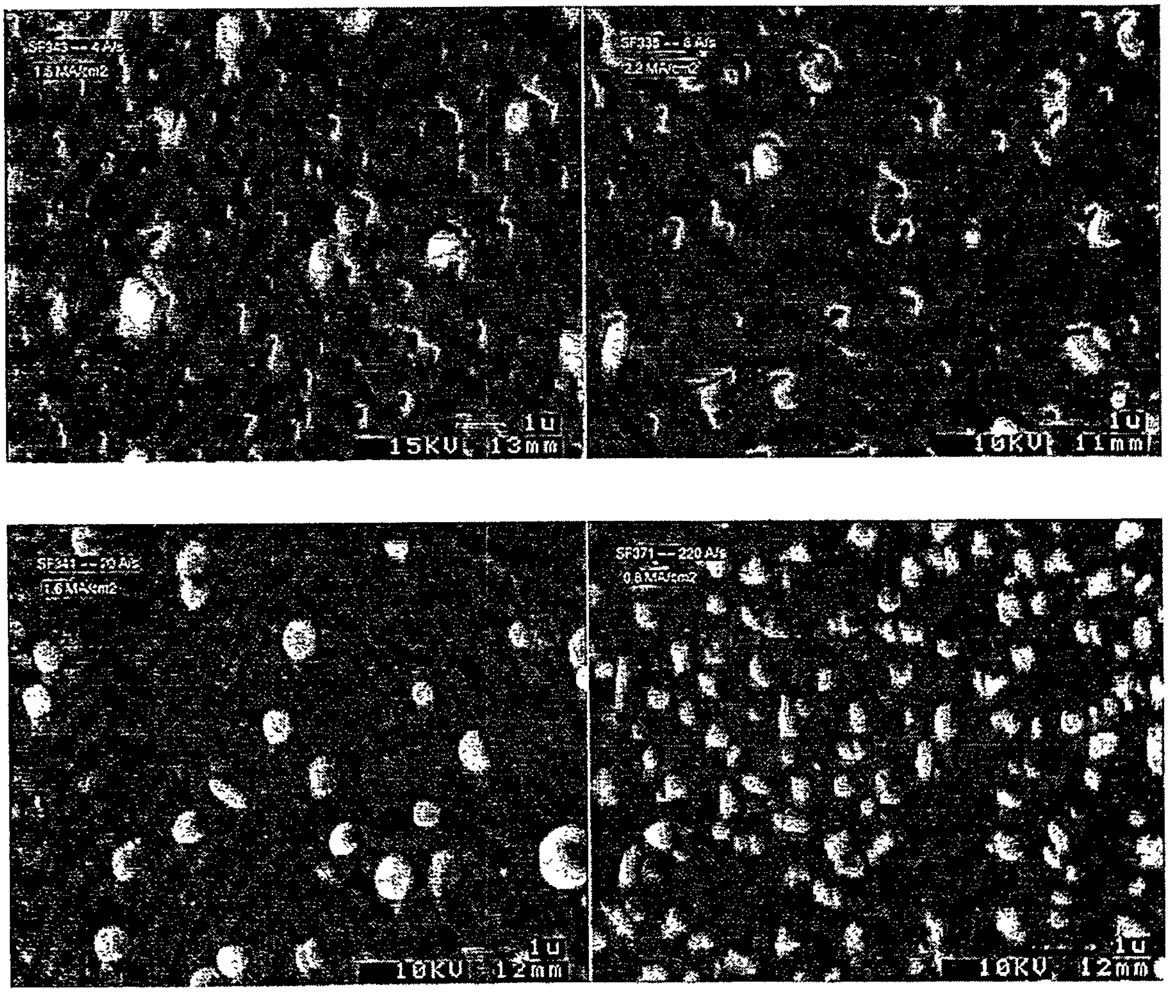

Figure 12. Scanning electron micrographs of 1-mm-thick YBCO films produced at four different deposition rates: (a) 4 Å/s, (b) 8 Å/s, (c) 20 Å/s, and (d) 220 Å/s.

Table 2. Structural Comparison by X-Ray Diffraction of YBCO Films Produced at Different Deposition Rates

	4 Å/s	**220 Å/s**
χ Scan on (102)	no a-Axis	no a-Axis
Rocking Curve on (005)	0.29° FWHM	0.29° FWHM
ϕ Scan on (103)	0.84° FWHM	1.11° FWHM
c-Axis Lattice Constant	11.677 ± 0.002 Å	11.715 ± 0.005 Å

Table 2 also lists the c-axis lattice parameters, which can be used to determine the YBCO oxygen content for low- and high-rate films. The lattice constants shown would correspond to an oxygen stoichiometry of 6.93 for the 4-Å/s film, which is nearly ideal, and 6.65 at 220 Å/s. The latter value indicates a significant oxygen deficiency that could be responsible for the reduced J_c at high deposition rates. At first, this seems plausible because of the dramatically different periods of time during which the films were exposed to deposition conditions – less than a minute at high rate, and nearly an hour at low rate. However, conversion to the fully oxidized state from O >~6.4 occurs at low temperatures and high O_2 pressures, relative to deposition conditions, and should have been completed during the cooldown after deposition, and/or annealing of the silver pads.

Another possible cause for a shift in the c-axis lattice parameters is Y-Ba cation disorder. This is also plausible since at very high deposition rates incident vapor can quench the motion of vapor condensed on the growing film surface before equilibrium diffusion processes can assure assembly of the correct crystal structure.

Either case – O_2 deficiency or cation disorder – should be reversible by annealing at elevated temperature. Since the Ag-anneal at 550°C failed to improve J_c, three different treatments were tried at 790°C, the temperature used for deposition. The first anneal involved simply soaking a high rate film for 20 minutes at deposition pressure (0.2 torr O_2) after the coating was completed and before cooldown. The second test involved cooling the film in the usual way, then in a separate chamber reheating and soaking for 1 hour (also in 0.2 torr O_2), followed by another cooldown in 250 torr O_2. The final test was similar to the second except that the ex-situ anneal took place in a furnace in 1 atm of flowing O_2.

All three tests produced similar improvements in J_c and T_c, as shown in Figs. 13 and 14, respectively. While still an average of 20% below the zero rate intercept, the annealed-film values of J_c are significantly higher than for high-rate films without the anneal. Annealing also improved (lowered) film resistivity (Fig. 15), although the degree of improvement was not as dramatic as for J_c. For comparison with the c-axis lattice parameters in Table 2, annealing a 220 Å/s film at 750°C in 1 atm O_2 for 30 minutes, reduced the lattice constant to 11.688 ± 0.002 Å.

Considering the effect of deposition rate on film morphology (Fig. 12), and the expected influence of morphology on flux pinning, a series of measurements was made with an external magnetic field applied parallel to the c-axis, i.e., perpendicular to the film plane. The results are shown in Fig. 16. For a film deposited at 8 Å/s, with a low-density population of both voids and outgrowths (see Fig. 12b), J_c dropped by about two orders-of-magnitude at 5 T, which is consistent with previously published results for YBCO films on $SrTiO_3$ substrates. The drop is ten times greater at the same field for a film deposited at 240 Å/s. Again, however, Fig. 16 shows that annealing reversed the effect(s) of high-deposition rate. It is not yet known whether annealing changes the morphology of high-rate films, so no correlation can be made between surface morphology and flux pinning at this point. It may be that the differing behavior in field of these films is influenced simply by changes in T_c (Fig. 14) for the different processing conditions.

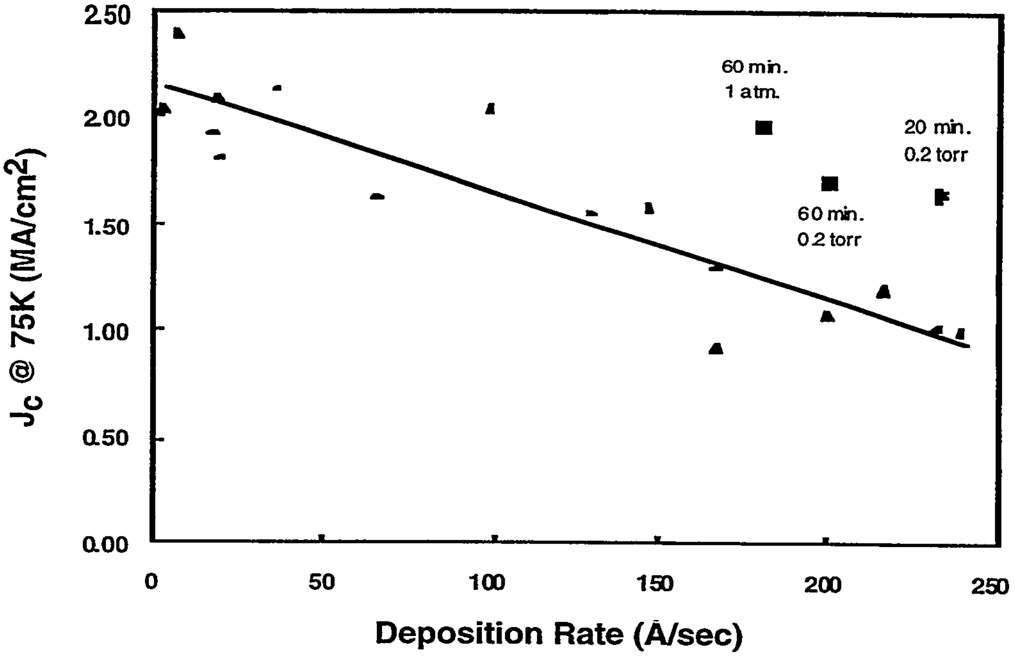

Figure 13. The critical current density varied with deposition rate for YBCO films deposited on $SrTiO_3$ substrates. Annealing the rapidly deposited films in oxygen resulted in a substantial recovery of the current density at high deposition rates.

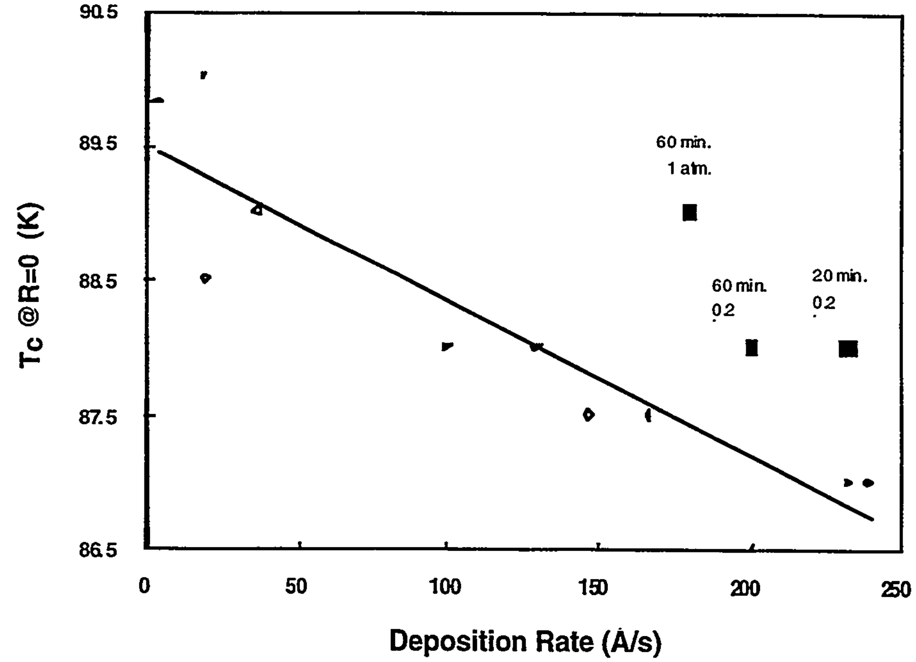

Figure 14. Superconducting critical temperature T_c for films made at different deposition rates and annealed in oxygen at different pressures and for different times.

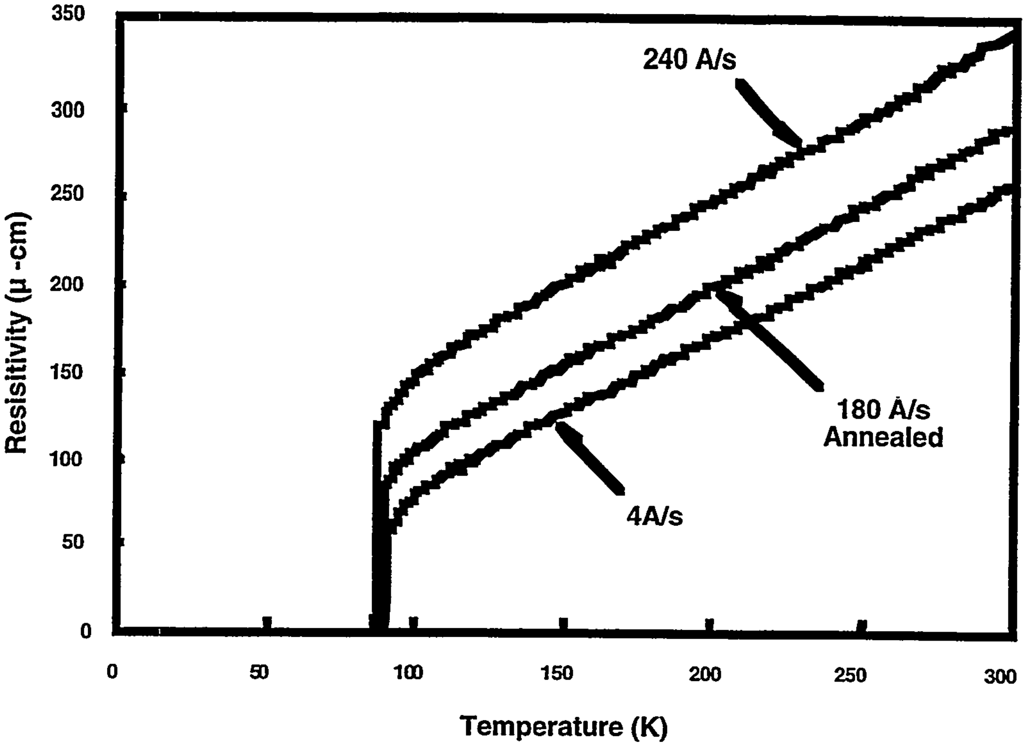

Figure 15. Resistivity as a function of temperature for films deposited at high and low deposition rates and for one film at an intermediate rate and annealed.

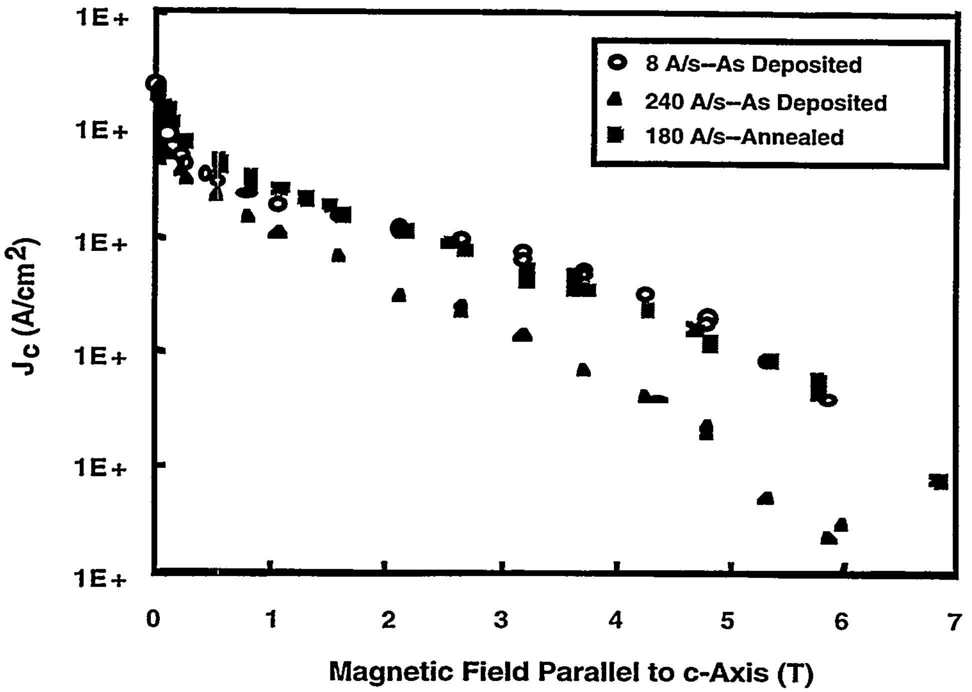

Figure 16. Critical current density J_c as a function of magnetic field for tapes deposited at high- and low-deposition rates and for one film at an intermediate rate and annealed.

A question remains as to whether the degradation in film performance at high deposition rate is due to oxygen deficiency or cation disorder. The observation that a 790°C anneal improves properties, while a 550°C anneal does not, implies that cation disorder is the problem. There is further evidence for this in the earlier work on thin films; specifically, a trend toward higher minimum yield (χ_{min}) in channeling mode RBS. (It should be noted that in the earlier work, there was also an observation of a-axis film growth at high rates, accompanied by a jump in χ_{min}. This is probably a result of the lower deposition temperature, 730°C, used in that work; in any event, χ_{min} was increasing with rate prior to a-axis formation.) This increase in χ_{min} is a sensitive indicator of the onset of crystalline disorder and is not affected by oxygen deficiency. The final resolution of this question, however, will require additional analysis to independently evaluate oxygen content and cation order.

Finally, returning to the issue of the manufacture of YBCO coated conductors, it appeared at first that the goal of 1 MA/cm^2 for 1-μm films deposited at 100 Å/s was easily reached, even without post-deposition annealing. However, the results presented here are for YBCO deposited on single-crystal substrates, which yields higher J_c than the flexible metal substrates necessary for most applications. YBCO texture on flexible substrates is imperfect at best, with in-plane rotation of grains leading to reduced J_c across the grain boundaries. Also, film-substrate interdiffusion at elevated deposition temperatures, especially with metallic substrates, can contaminate the YBCO, further reducing performance. This point is illustrated in Fig. 17. The highest values of J_c that we have measured on polycrystalline metal substrates with a textured buffer layer are only 50 to 70% of comparable values for YBCO on single-crystal substrates, leaving us very close to the minimum manufacturing criteria. Clearly, more effort is needed in this area.

In summary, a series of 1-μm thick YBCO films has been produced by PLD at deposition rates from 2 to 240 Å/s, and J_c of these films was found to decrease from 2.2 MA/cm^2 at low rate to about 1 MA/cm^2 at high rate. Other film properties such as T_c, resistivity, and J_c in an external magnetic field were degraded at high rate as well. We found that these film properties could be largely restored by a high-temperature anneal, suggesting that the degradation was caused by cation disorder in films produced at high-deposition rates.

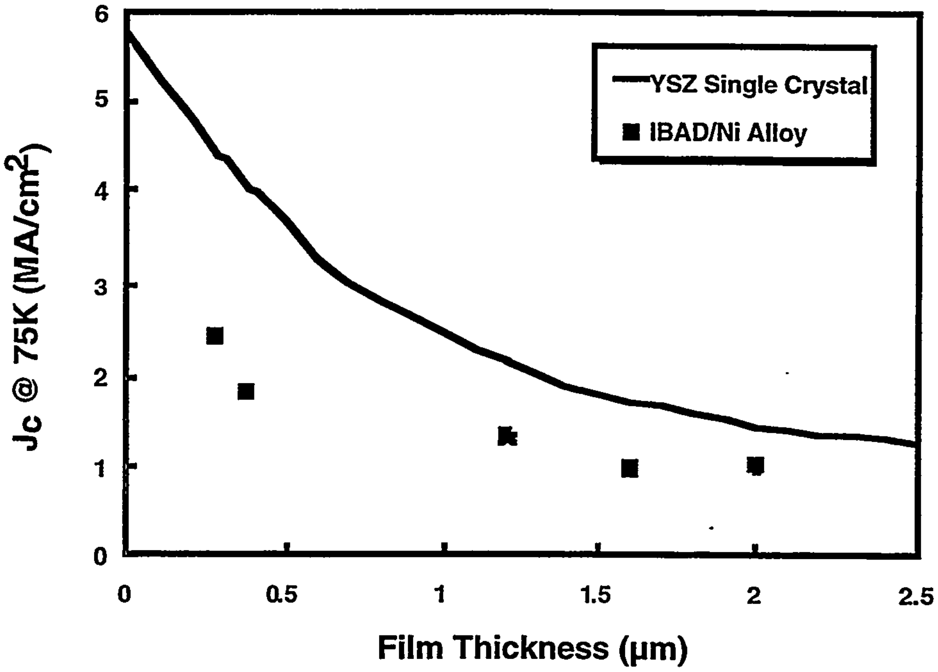

Figure 17. Comparison of the effects of thickness on the critical current density for films deposited on YSZ single-crystal substrates and on polycrystalline Ni alloy with an IBAD buffer layer.

3.1.5 MgO Buffer Layers for YBCO Films

(S.R. Foltyn and P.N. Arendt, LANL; C. Wang and R. Hammond, Stanford Univ.)

During the past quarter, we had an opportunity to deposit YBCO on a few samples of IBAD MgO, which were provided by C. Wang and R. Hammond at Stanford University. The substrate material was polished Hastelloy 242. The Stanford MgO process is significant in that texture is developed in the growing film in less than one minute, resulting in a dramatic increase in the IBAD deposition rate as compared to IBAD of YSZ. Prior to this quarter's work, however, there had been no demonstration that high-current YBCO could be deposited on the thin, textured MgO. The details of the MgO IBAD process were presented by C. Wang at the Spring 1997 Materials Research Society meeting, and will soon be published by the Stanford group.

Since MgO can be a tricky substrate material because of its 4.2Å lattice constant, a buffer layer sequence that was previously developed at Los Alamos for single-crystal MgO was employed. First, a layer of YSZ was deposited, followed by Y_2O_3, and then YBCO. All three layers were produced by pulsed-laser deposition in a single run by sequentially switching targets through a load-lock. The YBCO thickness was between 1.2 and 1.3 µm.

Although the MgO texture was difficult to determine due to low x-ray count rates, the φ-scan peak width for the IBAD layer was approximately 13° FWHM. Unlike IBAD

YSZ, however, the sample with the highest J_c exhibited little or no texture improvement in successive layers: the YSZ was 12.8° FWHM, and the YBCO was 12.5° FWHM. There was none of the 45° YBCO rotation that is sometimes observed, nor did an x-ray χ-scan reveal any a-axis oriented YBCO.

Following deposition, the 1 cm^2 sample was patterned with two isolated 5 mm long bridges of approximately 200 μm width. After the evaporation and annealing of silver contact pads, the bridges were characterized. From R(T) measurements (Fig. 18), the room temperature resistivity was about 300 μΩ-cm with an extrapolated intercept (T = 0 K) of 5~8 μΩ-cm. The T_c (R = 0) values were somewhat low – at 86.5 K – implying that some optimization is in order.

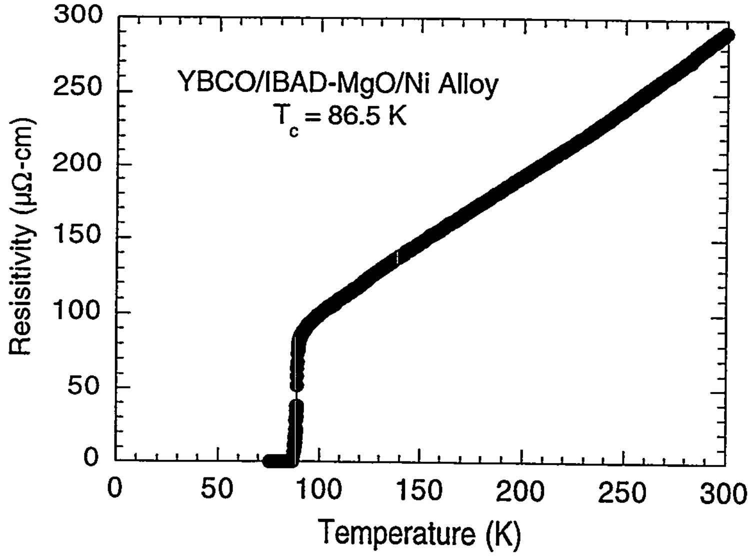

Figure 18. Resistance vs.temperature for a YBCO film on an IBAD-MgO template layer.

Critical current density values (Fig. 19) at 75 K and self field were 270 and 360 kA/cm^2, which are well within the range of values that we typically achieve for YBCO with a ϕ-scan FWHM of 12.5° on IBAD YSZ.

Finally, a single-crystal MgO substrate was also included in the run as a control sample. From the R(T) curve: T_c (R = 0) was about 1 K higher than the IBAD sample at 87.6 K; ρ_{extrap} (0 K) = 4 μΩ-cm; ρ(300 K) = 211 μΩ-cm; and J_c = 2.8 MA/cm^2. These results, being fairly typical for single crystal substrates (with the caveat that our experience with MgO is very limited), imply that the YBCO part of the run was unexceptional.

These results are quite exciting, in that they constitute the first validation of the Stanford research on ion-beam assisted deposition of MgO, which, by virtue of its inherently higher rate of texture formation, greatly enhances the commercial viability of the IBAD process.

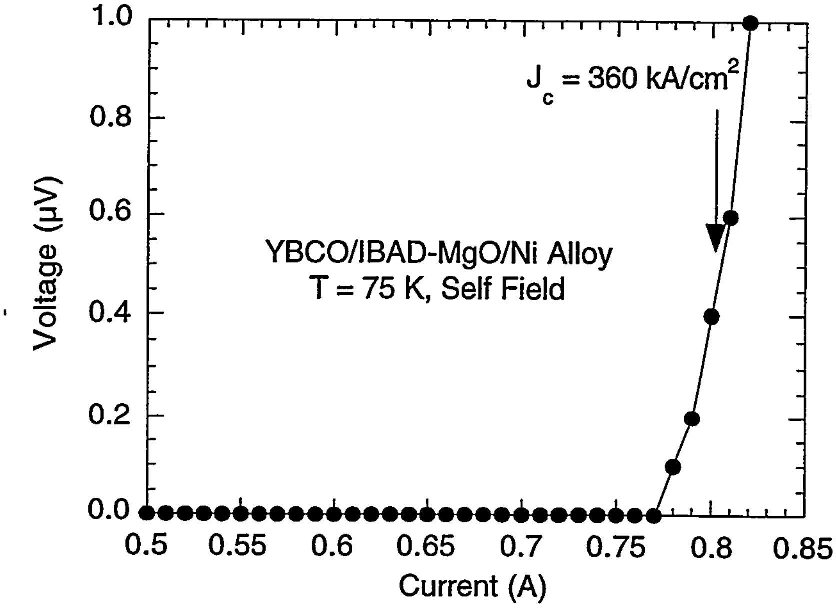

Figure 19. Current-voltage characteristic at 75 K and self field for a high-J_c YBCO film on an IBAD-MgO template layer.

3.1.6 Critical Current and Flux Pinning in Biaxially Textured YBCO Coated Conductors

(J.O. Willis, M.P. Maley, J.Y. Coulter, S.R. Foltyn, P.N.Arendt, and H. Safar)

The STC Physics Group has been investigating the dependence of critical current density J_c on material properties of the YBCO films produced by PLD. In particular, we have looked at the dependence of J_c on the magnitude and direction of an applied magnetic field. In FY95 we investigated the J_c dependence of YBCO films up to 9 T (Fig. 20) and then 18 T. The J_c for the field in the tape plane was significantly larger for the field parallel to the current direction than perpendicular to the current, showing that current flows along streamlines in these well connected, nearly single-crystal like YBCO films. This is in contrast to the results on Bi-2212/Ag or Bi-2223/Ag tapes, for which there is no dependence on the relative angle between the current and applied field for the field in the plane, indicating that the current flows along a percolative, tortuous path. Furthermore we noted that the YBCO/IBAD-YSZ/Ni alloy films show a field dependent peak in J_c for the field along the c axis.

In FY97 we continued our investigations into the source of this c-axis peak. In particular, we looked at the influence of extended defects, such as twin planes, on pinning. TEM investigation of these YBCO films show grain sizes of 2-5 μm and twin boundary spacing of ~0.2 μm. In the "I-Z" experiment, two bridges were patterned on one sample to have two different twin plane orientations with respect to current flow, as shown in Fig. 21. The volume pinning force should be proportional to the total area of extended defects perpendicular to the direction of current flow. Thus, there should be an enhancement by a factor √2 for the I case. The J_c values in field indicated that, indeed, there was enhanced pinning for this configuration (Fig. 22), and, thus, we concluded that the twin boundaries are a likely source of pinning for the field along the c axis.

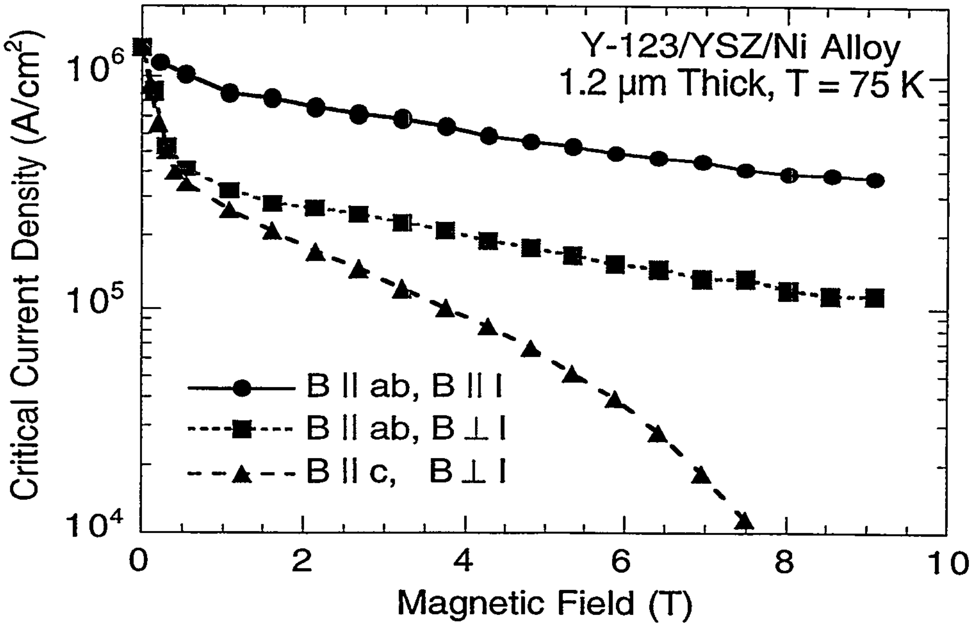

Figure 20. Critical current density for a YBCO film on an IBAD-YSZ buffer layer. The film shows streamline and thus Lorentz force free-current flow for B||ab and B||I. It also exhibits very little field dependence for B||ab with B⊥ I and high J_c ~10^5 A/cm^2 at 4 T.

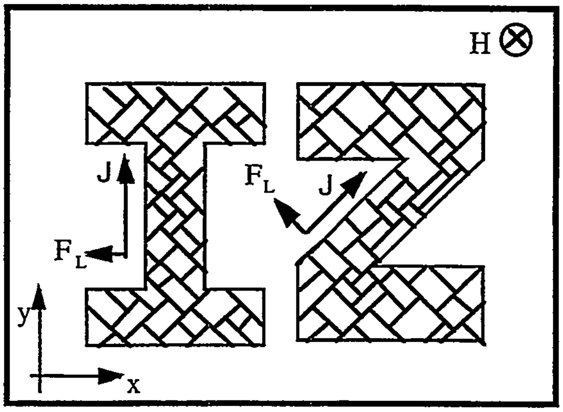

Figure 21. Bridge patterns "I" and "Z" of YBCO on a YSZ buffer layer. The parallel and perpendicular lines within the I and Z represent the twin planes schematically.

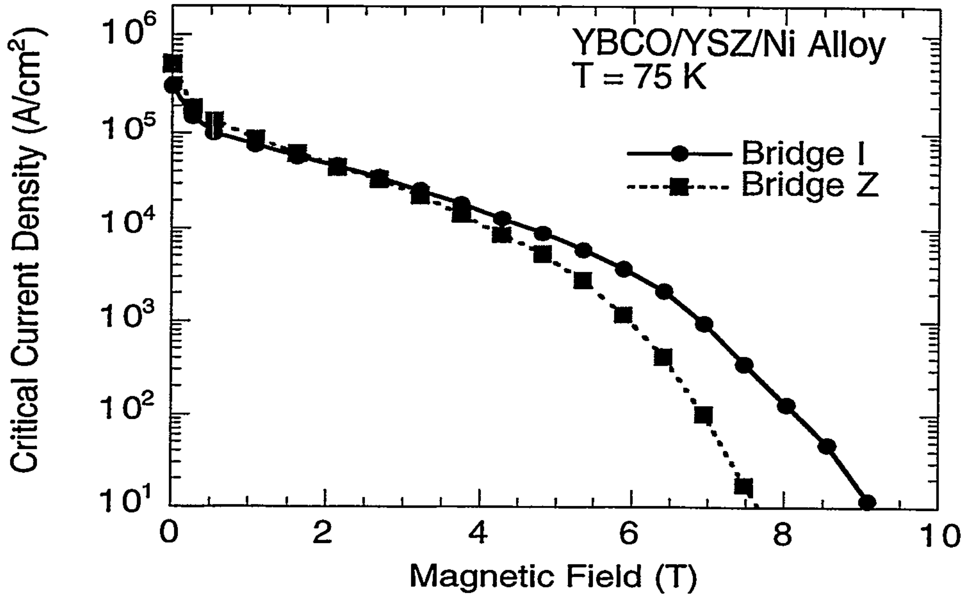

Figure 22. Critical current density vs. applied magnetic field for "I" and "Z" bridges deposited on a YSZ buffer layer on a Ni-alloy substrate. Pinning is enhanced for the I bridge.

Continuing our investigation into the source of c-axis pinning in YBCO films, we examined the thickness dependence of the anisotropy of J_c in an applied field. In all cases, the angles are defined with respect to the tape normal, i.e., at 0° the field is along the c axis and at 90° the field is in the ab plane. To eliminate some of the less well-controlled variables, these films were deposited on single crystal YSZ substrates with CeO buffer layers. Figure 23 shows a comparison of two films of thicknesses 0.13 and 1 μm. It is clear that the thinner film has almost no extra pinning along the c axis, whereas the thicker film has a pronounced feature near the c axis. The intrinsic pinning by the ab Cu-O planes, which is usually the strongest source of pinning in HTS materials, is much more sharply peaked than the c-axis feature.

The comparison of the J_c of these two films is even more striking when performed on an unnormalized basis. Figure 24 shows this comparison for the field along the c axis at 75 K. Even though the J_c of the thinner film is a factor-of-two greater at 0 T, there is a crossover at 4 to 5 T above which the J_c of the thicker film is greater. This implies that the strong pinning feature near the c-axis direction leads to enhanced performance in thicker films. We presume the extended defects that produce this pinning feature are related to the twin boundaries and that more are produced as the film gets thicker. We are currently investigating the microstructure of these films to confirm this thesis.

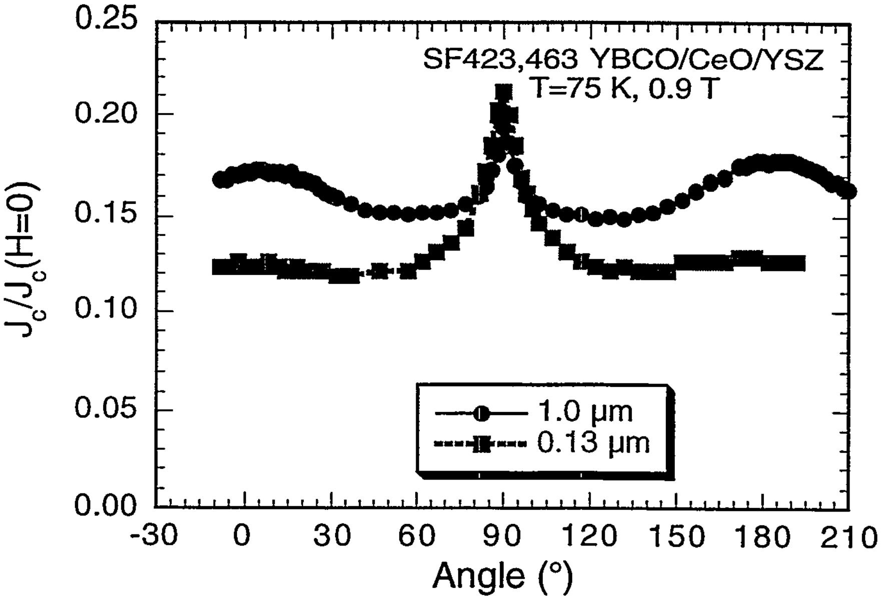

Figure 23. Comparison of the critical current density of two YBCO films of different thicknesses. J_c is normalized to the zero field value at 75 K. Both samples show a sharp intrinsic pinning peak for the field along the ab plane (90°), but only the thicker film shows a significant c-axis peak (0° and 180°).

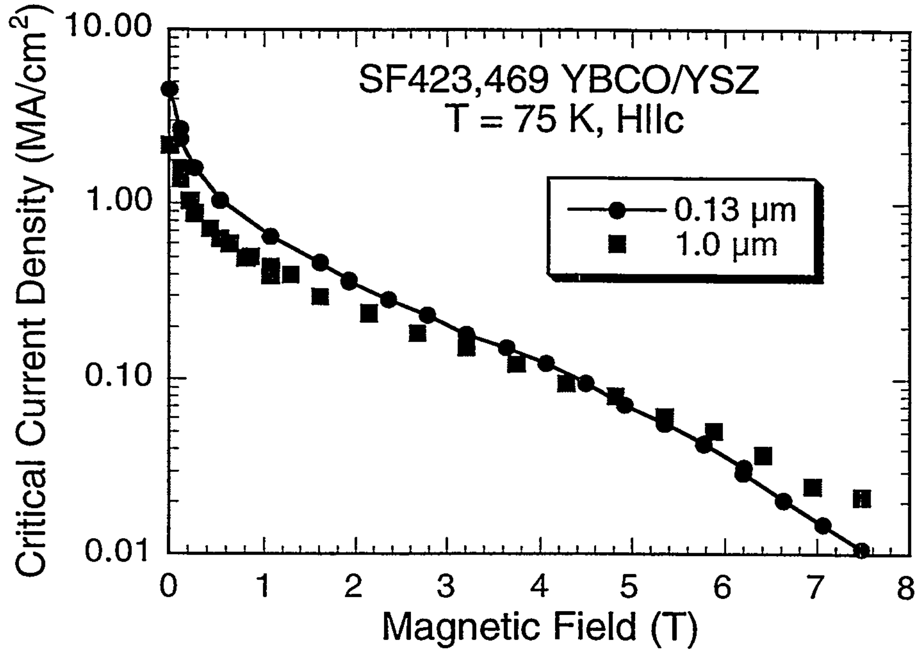

Figure 24. Critical current density J_c as a function of applied magnetic field along the c-axis direction for two YBCO films of different thickness. The thinner film starts off at twice the J_c of the thicker one, but a crossover occurs near 4-5 T that demonstrates the efficacy of extended pinning defects along the c-axis direction in the thicker film.

We next explored the effect of putting extrinsic defects into the YBCO films. We used ^{238}U ions produced by the Atlas accelerator facility at Argonne National Laboratory to irradiate the samples to various defect densities characterized by a matching field $B\varphi$ at which the number of defects is equal to the number of flux quanta. The parallel columns are extended defects like twin boundaries and should affect J_c in a similar fashion. Most of the work done with heavy ion irradiation focused on bulk single crystals of YBCO or Bi-2212, which have very low defect densities and therefore low J_c values. Thin films, however, have very strong pinning from growth defects, twin planes, and other types of defects. Thus, it is likely to be more difficult to produce the same dramatic improvement in properties that are seen in single crystals.

We irradiated films of different thicknesses to several different defect densities at angles of 0°, 15°, and 45°. Here we look only at a sample irradiated along the c axis, that is, at 0°. This is a film deposited on a IBAD-YSZ layer on a Ni alloy substrate. In Fig. 25 we see a very strong enhancement of J_c for the field parallel to the columnar defects.

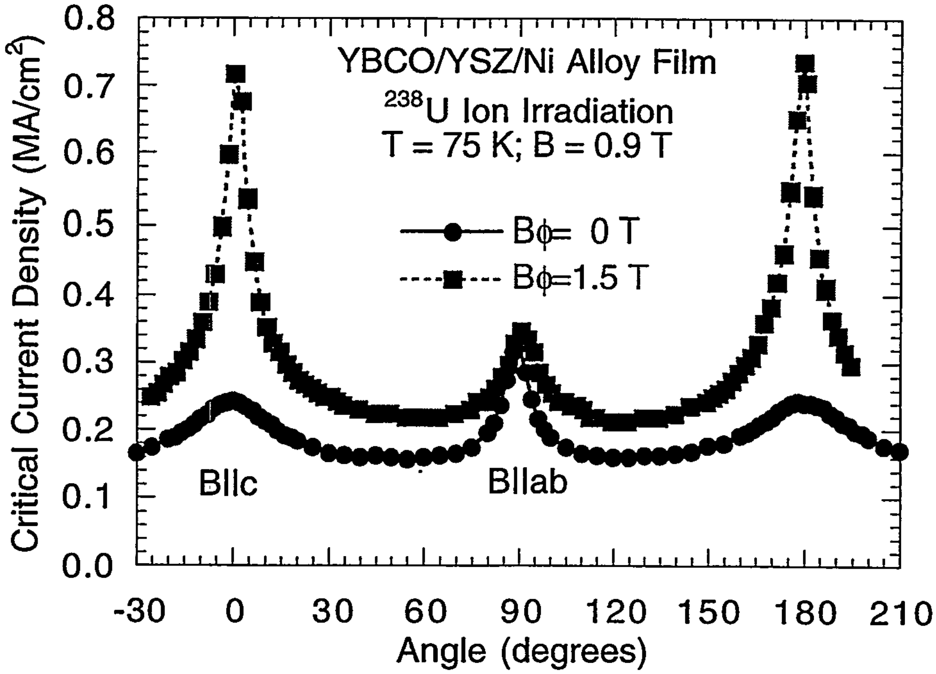

Figure 25. Critical current density J_c for different angles of the applied magnetic field of 0.9 T at 75 K. Results are shown for two initially similar but not identical films, so that the absolute values of J_c should not be compared directly. One of the films was irradiated to a defect density $B\varphi$ of 1.5 T along the c axis, and it shows a very strong enhancement when the applied field is parallel to the columnar defects.

When we examined the field dependence of the irradiated sample, we again saw the very strong effect of the columnar defects for the field along the c direction, especially at higher fields. As in the case of the thin/thick film comparison shown in Fig. 23, there is a kind of crossover behavior shown in Fig. 26, but in the present case it is a crossover in the relative strength of pinning for different field orientations as a function of field magnitude. Contrary to the intrinsic case (unirradiated YBCO), at low fields the pinning is actually stronger for H||c than for H||ab. Finally, above about 5 T, the intrinsic pinning wins out over the artificial pinning centers. This was expected, because above one or two times the matching field Bφ, all the defects are occupied with flux lines and they lose their effectiveness to pin more.

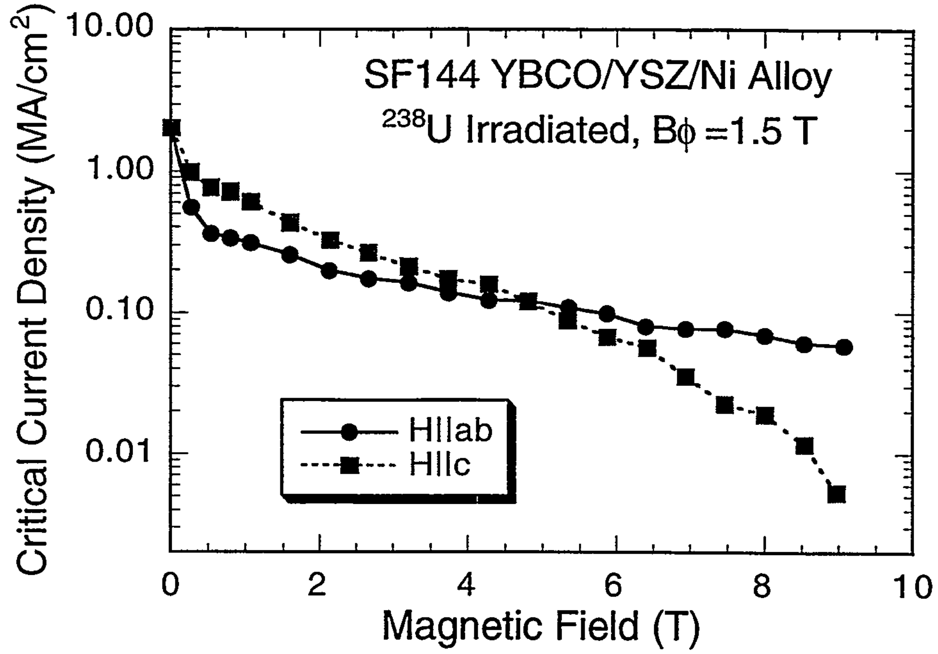

Figure 26. Critical current density J_c as a function of magnetic field for a YBCO film irradiated along the c axis with U ions to a defect density Bφ of 1.5 T. Pinning along the c axis is strongly enhanced at all fields and exceeds the ab plane intrinsic pinning below ~5 T.

Our final investigation in this series was to examine the effect of splayed columnar defects on YBCO films. We reported on the irradiations above. For the last several years we have been investigating the effect of high-energy proton irradiation on Bi-2223/Ag tapes and have reported on our progress periodically in these reports. High-energy (800 MeV) protons induce fission in Bi and Pb nuclei resulting in energetic (~200 MeV) fission fragments that recoil several micrometers through the lattice creating randomly oriented, splayed columnar defects with amorphous cores surrounded by strain fields. The cores are roughly 5-10 nm in diameter and 5 μm long. Bi-2223 tapes show a very strong enhancement for magnetic fields applied normal to the tape plane, i.e., along the c axis for the well-aligned grains. Because there are no heavy nuclei in YBCO to act as a source of fission reactions, we used a 1-mil (25-μm) thick Au foil as a driver, or source, or fission reactions. Thus, any reactions that occur within a few micrometers of the rear surface of the Au foil will emerge from it and completely penetrate the YBCO film.

Figure 27 shows the results of irradiation of a 0.13-μm-thick YBCO film with 800-MeV protons to a defect density $B\varphi$ of ~0.5 T. Before irradiation, there is the normal degree of anisotropy in J_c; this is almost completely suppressed after irradiation.

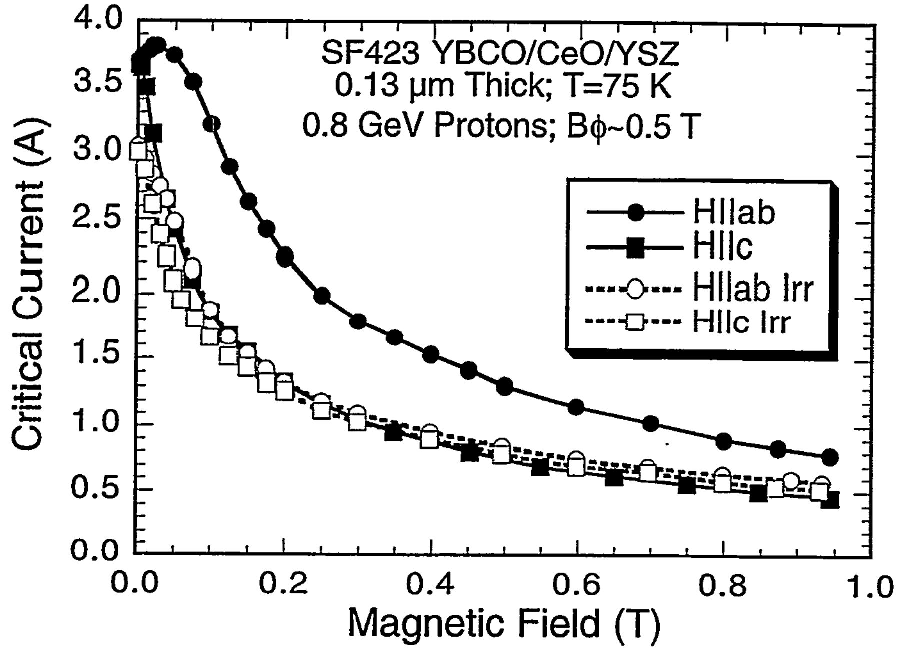

Figure 27. Magnetic field dependence of a YBCO film for H||ab and H||c before and after irradiation (labeled Irr) with 800-MeV protons to a matching field $B\varphi$ of ~0.5 T. The unirradiated sample shows a significant anisotropy, the result of the strong intrinsic pinning parallel to the ab plane. This is almost completely suppressed after irradiation.

Figure 28 shows the source of this loss of anisotropy in a different way. Here we can see very clearly that not only was the intrinsic pinning peak strongly depressed (from a peak-to-valley ratio of 1.73 to one of only 1.11), but that the J_c everywhere away from the ab plane was enhanced by the irradiation processing even at this low defect density.

This result was in contrast with what has been observed in an earlier study of parallel columnar defects in YBCO films produced by the Siemens group. Although they also saw a decrease in the magnitude of the ab plane pinning, Holzapfel et al. [Phys. Rev. B48, 600 (1993.)] observed that J_c is depressed everywhere away from the direction of the irradiation as revealed in Fig. 29. Thus, in the present case of irradiation with splayed columnar defects, the random orientation of these defects was advantageous in improving the performance of the material for almost every orientation of external magnetic field, and in decreasing the anisotropy of the material.

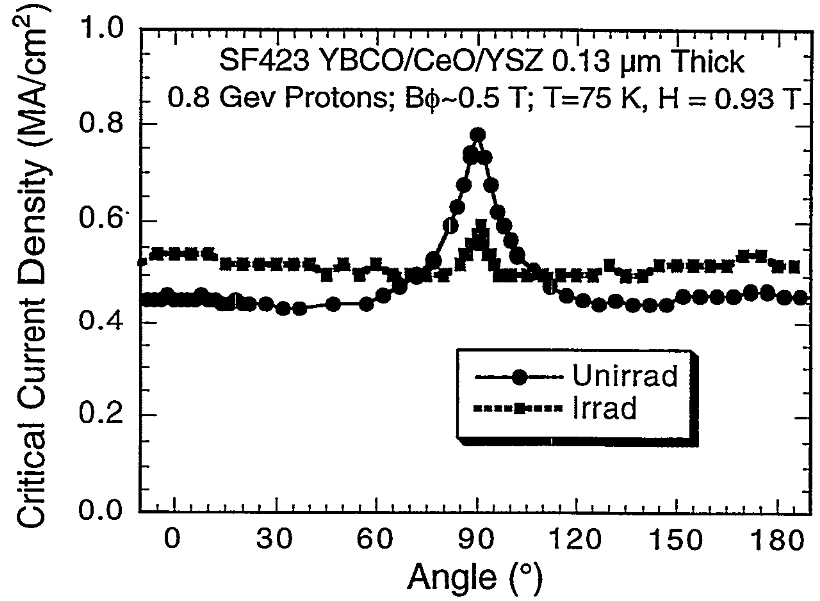

Figure 28. Angular dependence of the critical current density J_c at 75 K and 0.93 T for a YBCO film before and after irradiation with 800-MeV protons to a matching field Bφ of ~0.5 T. The intrinsic pinning peak is almost completely suppressed with the introduction of splayed columnar defects. However, J_c for all other angles away from the ab plane is enhanced by this low level of irradiation.

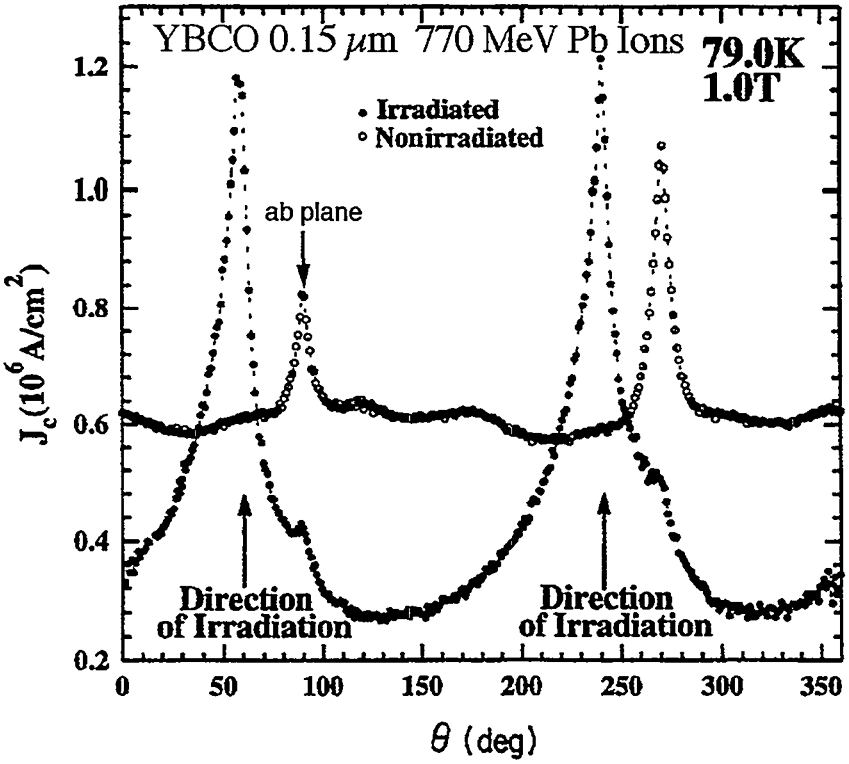

Figure 29. J_c is enhanced along the direction of irradiation but degraded for all other orientation for a thin film of YBCO irradiated with 770-MeV Pb ions. The figure is from B. Holzapfel, et al., Phys. Rev. B 48, 600 (1993.)

To summarize, we have shown that thick, biaxially textured films of YBCO generally contain c-axis oriented extended defects that provide strong pinning for H||c up to fields ~5 T. This results in a prominent peak in $J_c(\theta)$ near the c axis. Patterned film studies indicate a substantial contribution to pinning from twin planes. A comparison of thick films with thin films of YBCO not exhibiting the peak in $J_c(\theta)$ for H||c showed that the presence of this peak is correlated with a slower decline of $J_c(H)$ at fields above 1 T. Columnar defects created by heavy ion irradiation showed strong directional pinning when the field was oriented in the track direction, in agreement with previous studies on single crystal YBCO thin films. The columnar tracks produce pinning peaks in $J_c(\theta)$ that are stronger than the intrinsic peaks at low fields, making $J_c(H||c) > J_c(H||ab)$. At fields above the matching field there is a crossover to $J_c(H||ab) > J_c(H||c)$. Finally, we showed that randomly oriented columnar tracks produced by high-energy proton irradiation enhance J_c over an extended range of field orientation, but depress $J_c(H||ab)$, resulting in near independence of J_c on field orientation.

3.1.7 Bi-2212 Melt Processing of Tapes

(T.G. Holesinger, LANL; W. Dai and K. Marken, OSTI)

Recently, isothermal melt processing (IMP) was successfully applied to the processing of Bi-2212 tapes in the temperature range of 800°C to 840°C. The Bi-2212 85-filament tapes were supplied by OSTI. Several oxygen partial pressures were examined to determine an optimal oxidation atmosphere for the solidification step of IMP. It was found that long (≈ 15-20 cm), multifilament tapes could be processed between at least 820°C and 840°C with critical current density J_c in excess of 150 kA/cm^2 at 4 K and self field. Shown in Fig. 30 are the IV curves of one tape isothermally melt processed at 840°C for 15 hours using 20%O_2/Ar as the oxidizing atmosphere. Critical currents I_c of almost 300 A were obtained in this particular sample. The I_c value of 295 A translates into a J_c value of 175 kA/cm^2 at 4 K and self-field. The field dependence at 4 K of a Bi-2212 multi-filamentary tape is shown in Fig. 31. The latter tape was processed at 820°C for 15 hours again using 20%O_2/Ar as the oxidizing atmosphere. As is typical of most BSCCO tapes, the I_c values decrease faster for H oriented parallel to normal of the tape, or c-axis of the Bi-2212 grains in the tape.

The microstructure of these tapes is shown in Fig. 32. In general, the microstructure was composed primarily of the Bi-2212 phase with only small amounts of Bi-2201 and a few alkaline-earth cuprates. A few areas were found that locally contain excessive amounts of secondary phases. In the latter cases, it was surmised that localized inhomogenities are present in parts of the multi-filamentary tapes. Overall, none of the tapes processed by IMP showed signs of excessive bubbling. This latter observation, coupled with the relatively low processing temperatures, suggests that IMP could offer advantages over conventional melt processing of Bi-2212 tapes for commercial applications.

In summary, isothermal melt processing of Bi-2212 multi-filamentary tapes suggests that this process could offer several advantages over conventional melt-processing of Bi-2212 tapes. The lower processing temperatures and low-bubbling characteristics of IMP will be beneficial for the scale-up to the longer lengths needed for producing coils.

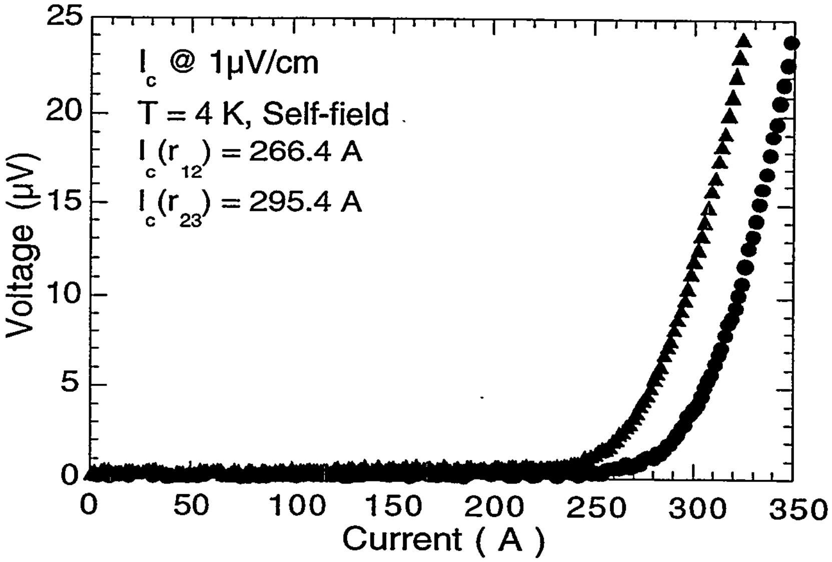

Figure 30. Current-voltage curves of a Bi-2212 isothermally melt processed at 840°C for 15 hours using 20%O2/Ar for solidification.

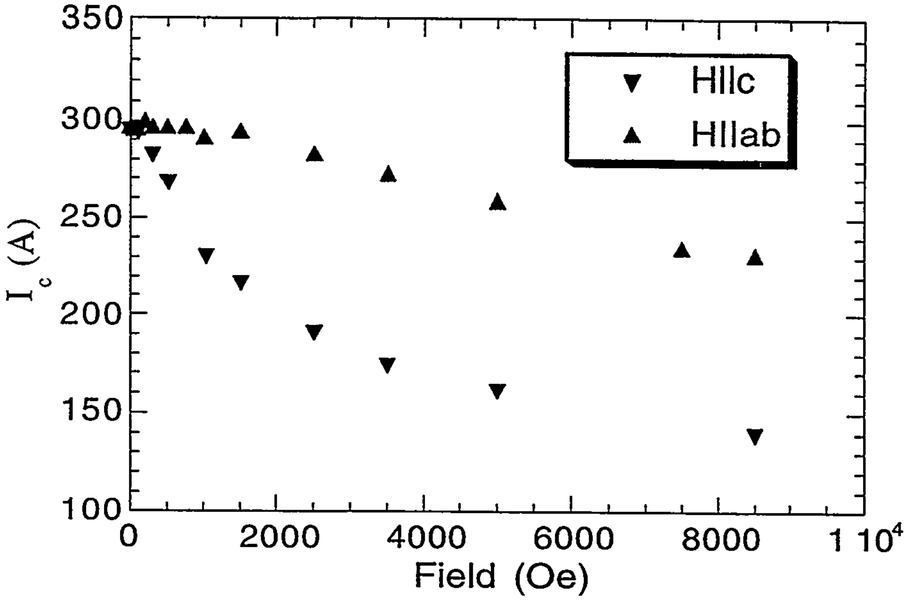

Figure 31. Field dependence at 4 K for a Bi-2212 multi-filamentary tape isothermally melt processed at 820°C for 15 hours using 20%O_2/Ar as the oxidizing atmosphere.

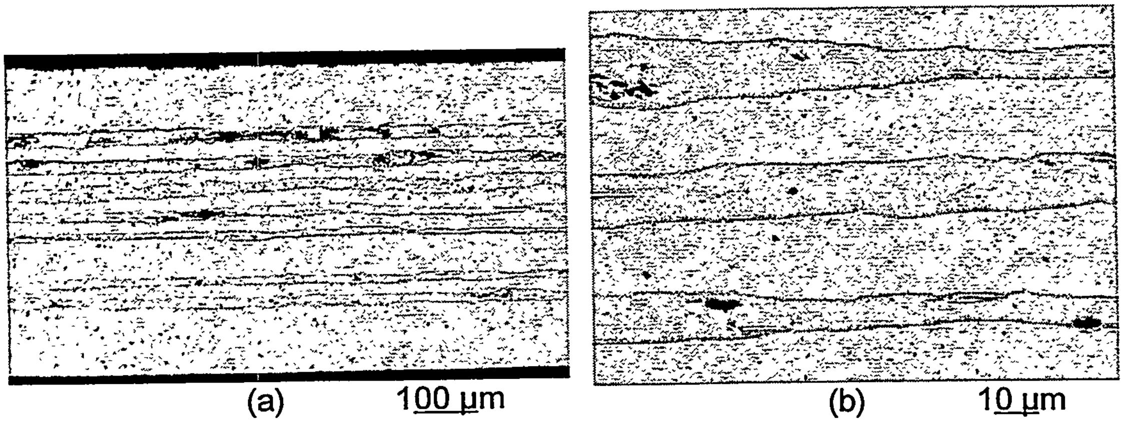

Figure 32. Backscattered electron micrographs of (a) long transverse cross-sections of a Bi2212 tape isothermally melt-processed at 840°C for 15 hours with 20% O_2/Ar.

3.1.8 Isothermal Melt Processing of Multifilamentary Bi-2212 Tapes

(T.G. Holesinger, LANL; W. Dai and K. Marken, OSTI)

Recently, isothermal melt processing (IMP) was successfully applied to the processing of Bi-2212 tapes in the temperature range of 800°C to 840°C. The Bi-2212 55-filament tapes were supplied by OSTI. It was found that long (≈ 15-20 cm), multifilament tapes could be processed between at least 820°C and 840°C with critical current density J_c more than 150 kA/cm^2 at 4 K and self field. Shown in Fig. 33 are the J_c data of Oxford 55 filament tapes as a function of time spent in the partial melt during processing at 820°C. The oxidation atmosphere used was 10% O_2/Ar. A wide range of melting times occurred where high-J_c tapes could be obtained. The highest I_c measured was 341 A at 4 K, which translates to a J_c value of 245 kA/cm^2.

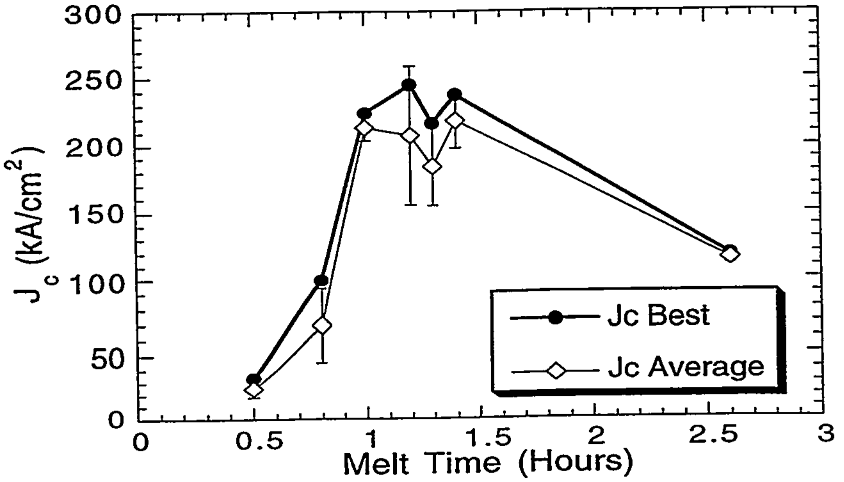

Figure 33. J_c values of OSTI 55-filament Bi-2212 tapes isothermally melt processed at 820°C with variable times spent in the partial melt. 10% O_2/Ar was used for oxidation. The best values were from 3-cm sections of the tapes; average values were derived from measurements of three or more sections from two or more tapes.

The lower J_c values obtained for short and long melting times could be correlated with changes in the tape microstructure. Shown in Figs. 34a and 34b are scanning electron microscopy/backscatter electron imaging (SEM/BEI) of tapes processed at 820°C using melting times of 0.5 and 2.6 hours, respectively. For the sample melted for only 0.5 hours, a very clean phase assemblage was found. However, grain sizes were small with very little alignment of the grains relative to each other. Hence, short times in the partial melt result in nearly phase pure material, but little grain alignment. On the other hand, long times in the partial melt lead to enhanced grain growth of the Bi-2212 and other secondary phases. The large alkaline-earth cuprate grain seen in Fig. 34b nearly spans the entire filament width. In short, long times spent in the partial melt resulted in enhanced grain growth and poor phase purity.

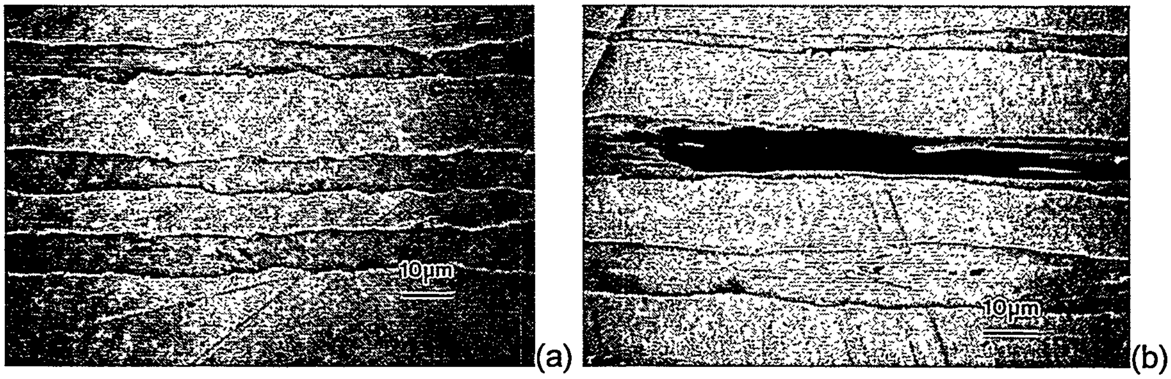

Figure 34. Long, transverse SEM/BEI images of Bi-2212 tapes processed at 820°C with melting times of (a) 0.5 hours and (b) 2.6 hours. 10%O_2/Ar was used for oxidation.

One aspect of isothermal melt processing is the ability to process at low temperature. This is important since at high temperatures, grain growth into the sheath can occur. The microstructure of a tape isothermally melt processed at 865°C using oxygen is shown in Fig. 35. The large colony of Bi-2212/Bi-2201 grains that cut the filament is noteworthy. The filament cross-cut colony microstructure was common in samples processed above 840°C, but was rarely found in tapes processed below this value.

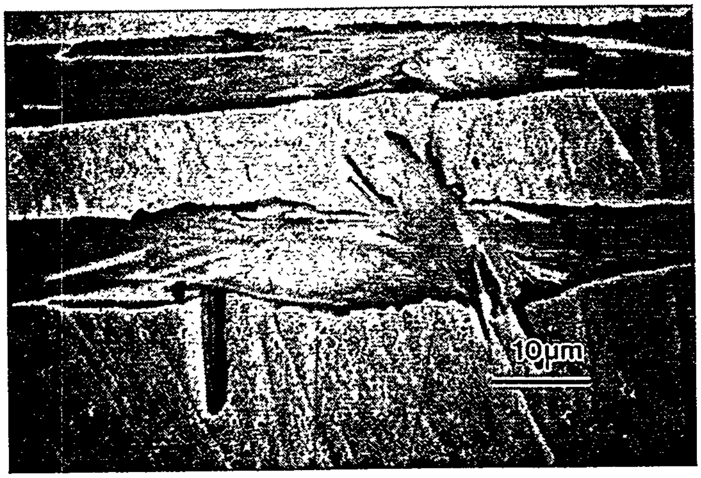

Figure 35. Long transverse SEM/BEI image of a Bi-2212 tape processed by IMP at 865°C in oxygen. Time spent in the partial melt was 0.9 hours.

3.1.9 High Resolution TEM of High J_c Bi-2223 Tapes

(T.G. Holesinger, LANL; G.N. Riley, Jr., A.P. Malozemoff, Q. Li, S. Fleshler, M. Teplitsky, and M.W. Rupich, American Superconductor Corp.)

Recent work on the microstructure of high-J_c (55 kA/cm^2), multifilamentary Bi-2223 tapes produced by American Superconductor Corporation (ASC) has revealed some key insights into the types of structures within the individual filaments. This microstructure was probed by analytical and high-resolution transmission electron microscopy. There are two types of overall microstructure within the filaments: a highly aligned, dense, well-connected colony structure near the silver interface and a porous, somewhat disconnected and misaligned colony structure in the middle of the filaments. These two types of general microstructure are shown in Figs. 36a and b.

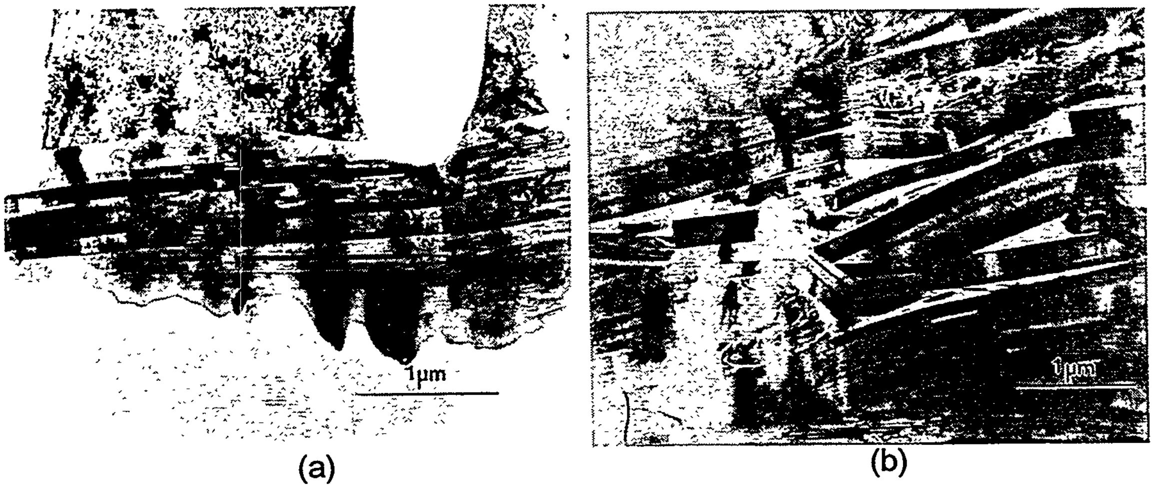

(a) (b)

Figure 36. TEM micrograph of the overall microstructure (a) near the silver sheath and (b) in the middle of the filament.

The microstructure within the grains and colonies was also complex. Within grains, dislocations were present to accommodate grain bending. Grains were found to be bent to accommodate the changes in the filament dimensions. Figure 37 shows the alignment of several dislocations that make up a bend boundary in one such grain. Also found at grain boundaries are small pores. These pores may represent the residual defects from cracks that are healed during heat treatment. Typical pore structures are shown in Figs. 38a and b.

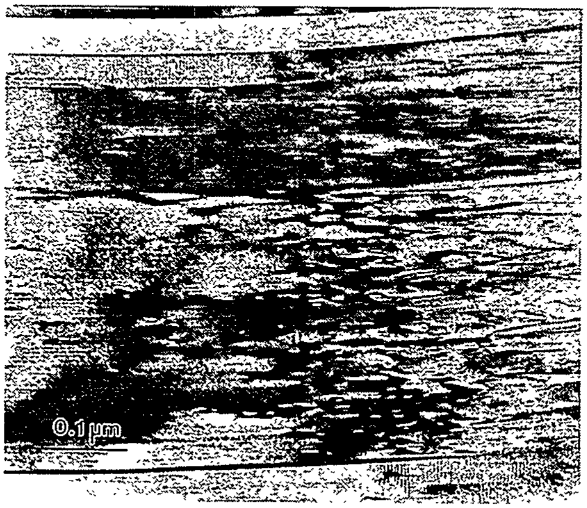

Figure 37. TEM micrograph of a bend boundary within a Bi-2223 grain.

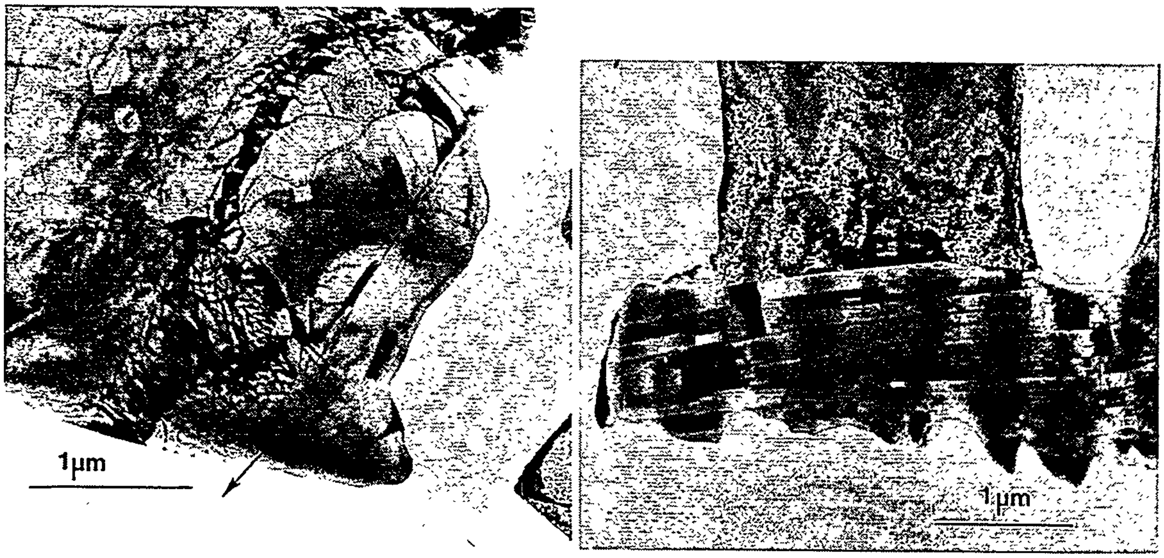

Figure 38. TEM micrographs of the pore structure found between grains as viewed in (a) plan view and (b) short transverse.

Even in these high-J_c samples, many secondary phases still exist. In general, the presence of secondary phases can coincide with high J_c values provided the placement of the secondary phases is not detrimental to colony alignment. A currently held belief is that the highest amount of transport current is carried in the interfacial region where the alignment is very good. Unfortunately, some secondary phases do end up in the interfacial regions where they cause disruptions in the colony-to-colony alignment. Shown in Fig. 39 is a TEM micrograph of a "3221" phase embedded in the silver/Bi-2223 interface. Large amounts of porosity are part of this phase assemblage and disruptions in the underlying Bi-2223 colony alignment are evident.

High-resolution TEM has been used to look at boundaries between grains within a colony and between adjoining colonies. The high-resolution micrograph shown in Fig. 39a is of an amorphous phase sandwiched between the basal-plane faces of two adjacent Bi-2223 grains. In Fig. 39b a distinct Bi-2212 grain can be seen as part of the colony microstructure. Clearly, the presence of such defects define a type of gating mechanism for current flow in the c-direction between grains and colonies. Figure 40 shows two colonies that are joined at a small angle relative to their basal planes. Changes in lattice spacing at the interface suggest some sort of compositional modulation is occurring to accommodate this particular grain boundary. Also note the presence of a terminating Bi-2212 intergrowth region in the bottom grain and close to the interface. Again, these types of colony structures are thought to limit current flow in the c-axis direction and could be considered as a type of gating mechanism for current flow in these high performance tapes.

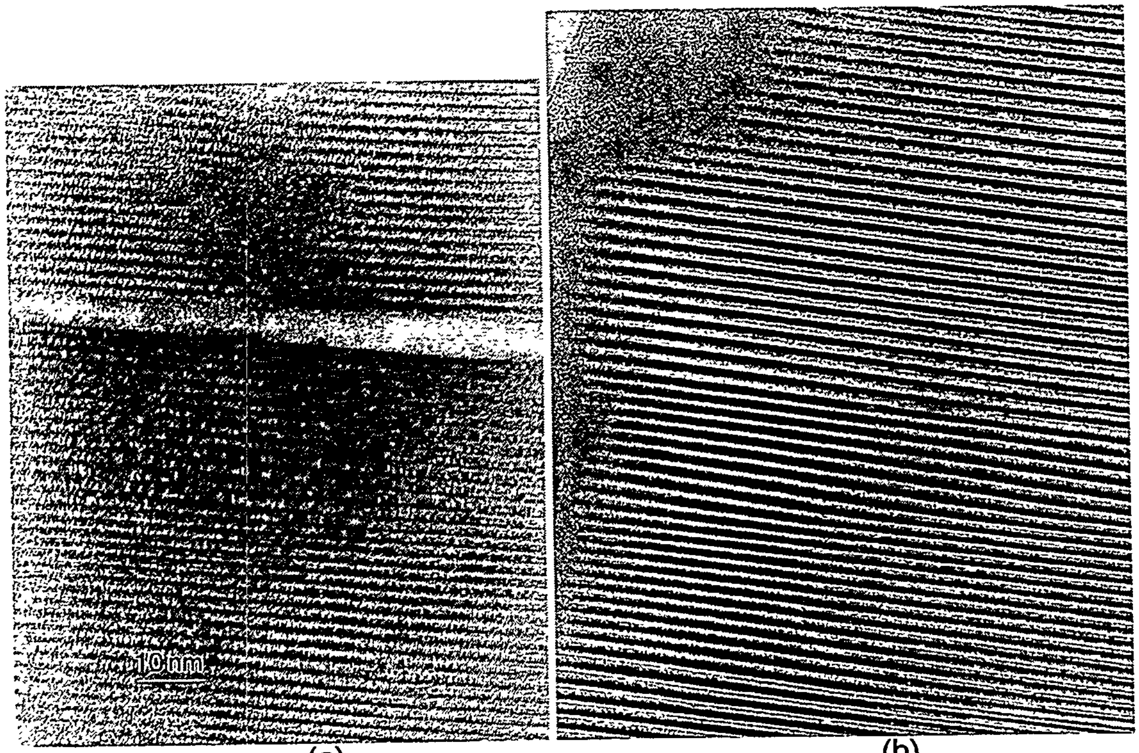

(a) (b)

Figure 39. High-resolution TEM micrograph of the boundary between two adjoining colonies.

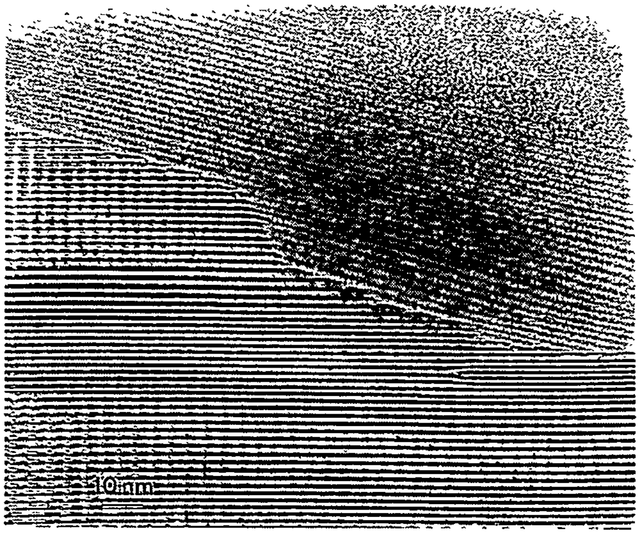

Figure 40. High-resolution TEM micrograph of the boundary between two adjoining colonies.

3.1.10 Microtexture Characterization of a Bi-2223 Tape

(J.F. Bingert, LANL; G.N. Riley, Jr., ASC)

The local texture in a 19-filament Bi-2223 tape from ASC was interrogated via the indexing of Electron Back-Scattered Patterns (EBSP) in the scanning electron microscope. The EBSP technique provides a means of mapping spatially specific orientation and misorientation relationships. The tape sample was prepared by etching away the silver sheath, exposing the top layer of HTS grains, i.e., those grains formerly at the silver/HTS interface. Figure 41 shows the relative position of two regions of a tape that underwent further characterization, the edge of an edge filament (edge region) and midsection of a centrally positioned filament (center region).

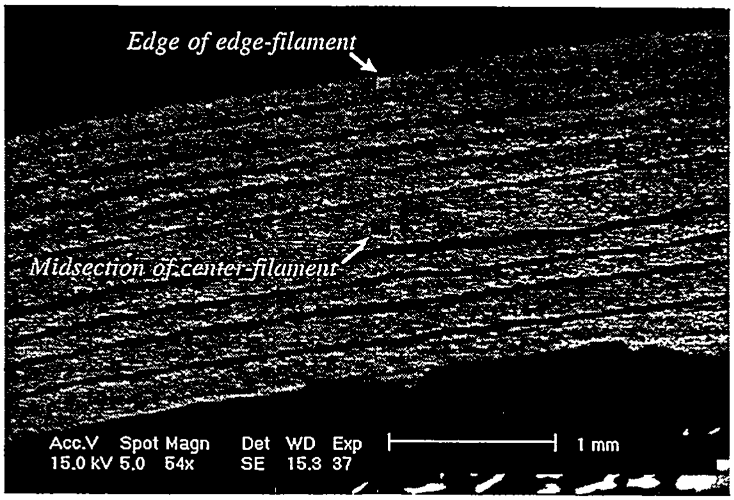

Figure 41. Relative positions of characterized regions within multifilament tape. Rolling plane-normal section.

The positions of discrete orientation measurements collected for the edge and center regions are shown in Fig. 42 superimposed on SEM micrographs. Considering the sample preparation along with the structure of Bi-2223, each orientation measurement represents the surface grain in a colony of grains bounded by <001> twist boundaries. Each measurement was taken on a spot that was clearly distinct from its neighboring colonies.

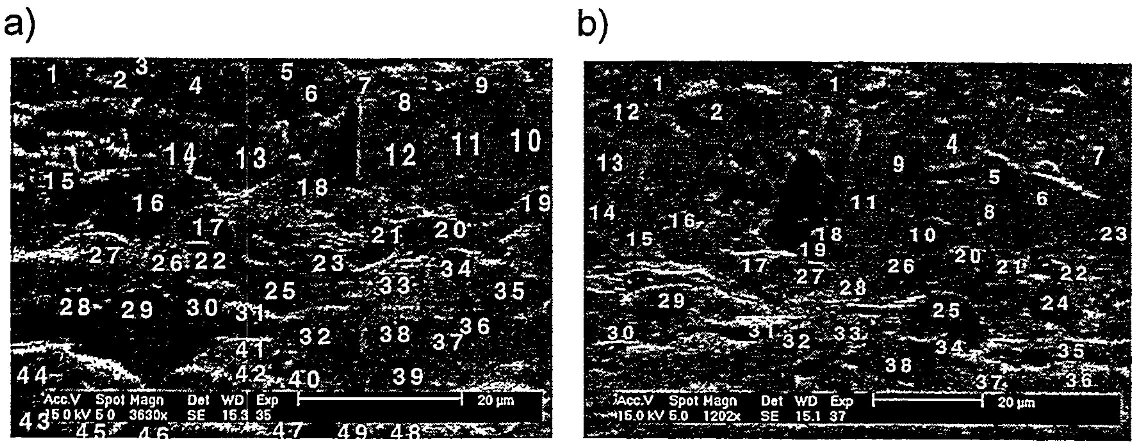

Figure 42. SEM micrographs showing discrete orientation sampling locations for a) an edge region and b) the center region of a multifilament tape.

Figure 43 presents two representations of the texture from the edge region. The {001} (basal plane) and {100} pole figures (Fig. 43a) show a tight distribution of basal planes aligned with the rolling plane of the sample, and a non-fiber distribution of rotations about the basal plane, respectively. This suggestion of some degree of ab plane (in-plane) texture is reinforced by the correlated misorientation distribution (Fig. 43b). This histogram bins misorientation angles about the <001>-axis between adjacent colonies as a fraction of the total number of colony boundary segments. A random distribution, representative of no in-plane texture, is suggested by the dashed line. The results suggest a tighter misorientation between colonies than a random assemblage.

Figure 44 shows a reduced section from the edge region, including a projection of the basal plane for each colony, and boundary segments highlighted by their relative misorientation. Once again, the results show a preference toward smaller misorientations about the c axis than a {001}-textured assemblage with random in-plane texture, and suggest that an orientation correlation exists between colonies at a local scale.

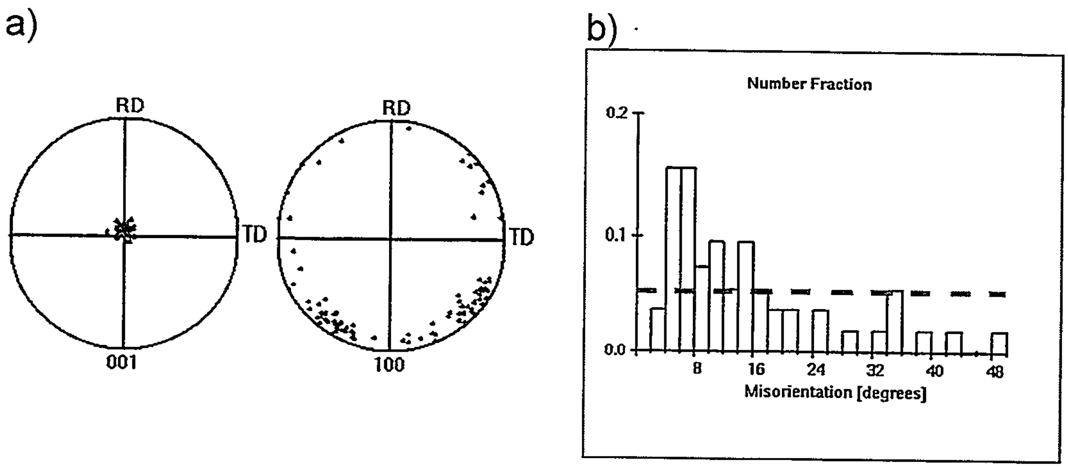

Figure 43. Texture data from the edge region presented as a) plane normal {001} and {100} pole figures and b) a histogram of the correlated misorientation distribution about <001>-axis.

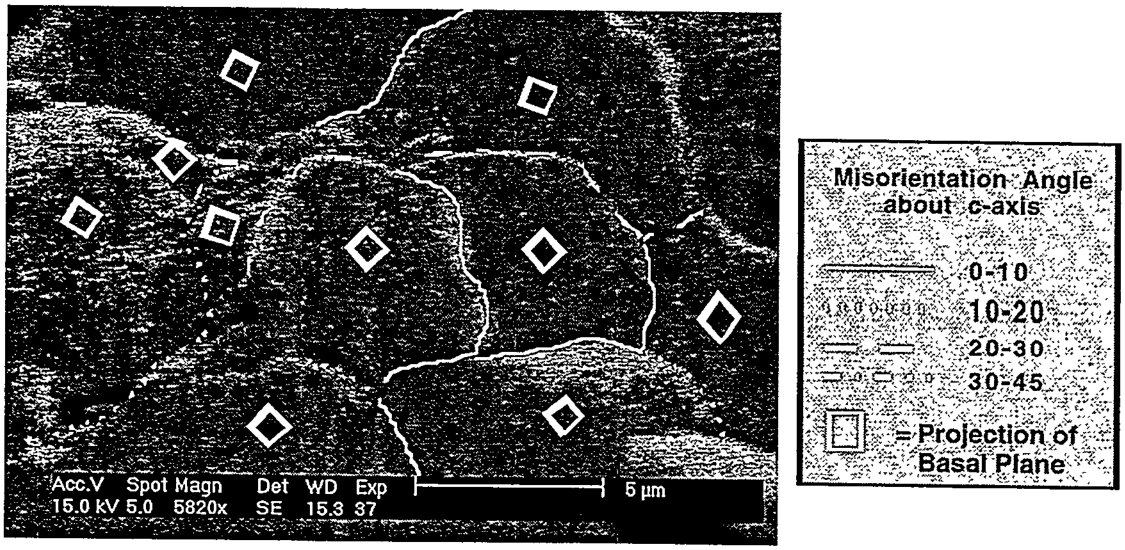

Figure 44. SEM micrograph with orientation information; boundary misorientations about the <001>-axis and relative basal plane orientations from selected area within an edge filament.

However, this degree of local in-plane texture was not universal, as indicated by the texture data shown in Fig. 45, measured on the center filament (Fig. 43b). In this region, the {100} pole figure suggests a nearly symmetric distribution about the <001>-axis, and the misorientation distribution is close to random. Questions such as whether the difference between the two regions is related to their relative position, and the relative frequency of local in-plane alignment within tapes, await further investigation.

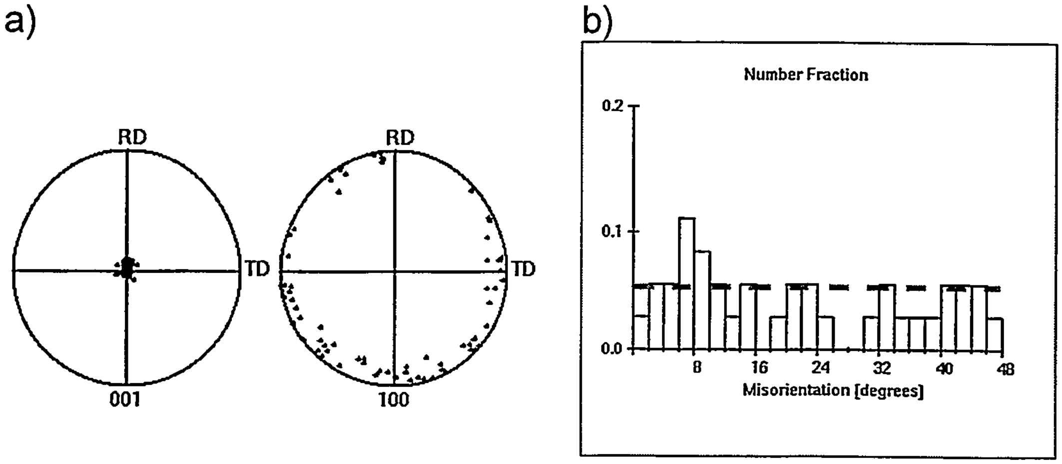

Figure 45. Texture data from the center region presented as a) plane normal {001} and {100} pole figures and b) a histogram of the correlated misorientation distribution about <001>-axis.

3.1.11 High-Energy Proton Irradiation and Annealing of Bi-2223/Ag Tapes

(J.O. Willis, J.Y. Coulter, H. Safar, M.P. Maley, M. FitzGerald, M.C. Martinez, LANL; G.N. Riley, Jr. and S. Fleshler, ASC)

During this quarter we prepared for and conducted the irradiations of a new series of Bi-2223/Ag tapes, a Bi-2223/Ag pancake coil, and several YBCO coated conductor samples. Table 3 lists the samples type, the proton dose (1 Mμpulse ~ 3.8 x 10^{14} protons) with a Gaussian full width at half maximum of ~0.6 cm, the proton beam current in nA, and the nominal columnar defect density. At a defect density equivalent to 1 T, the number of defects is equal to the number of flux quanta in a 1-T magnetic field. The tape and crystal samples were mounted on a wheel (see Fig. 46) with 12 positions, including a clear hole for tuning the proton beam and a phosphor for monitoring the position and shape of the beam remotely with a video camera. The samples were located at indexed positions 30° apart at a fixed radius on the wheel. The samples could easily be changed remotely using a stepper motor and monitored with the video camera. Because the protons easily penetrate through ~50 cm of material, multiple samples were mounted behind one another. Our experiments last year on a stack of nine tapes showed that the dose and performance of all the tapes were nearly identical.

Table 3. Samples Irradiated with 800-MeV Protons

Wheel #	Sample	Proton Dose (Mμpulse)	Current (nA)	Nominal Defect Density (T)
1	4 pieces 85 filament Bi-2223 crystals	100	275	1.4
3	1 HiJ$_c$ multifilament 4 pieces 85 filament 2 pieces monofilament	80	218	1.1
4	4 pieces 85 filament Bi-2223 crystals	50	326	0.7
5	1 HiJ$_c$ multifilament 4 pieces 85 filament 2 pieces monofilament	123.5	216	1.7
6	2 pieces monofilament Bi-2223 crystals	172	488	2.4
7	YBCO, t= 0.64 μm	27	488	0.5
11	YBCO, t= 0.13 μm	35	395	0.6
12	YBCO, t= 1 μm	60	488	1.0
–	Pancake Coil	653	493	1.0

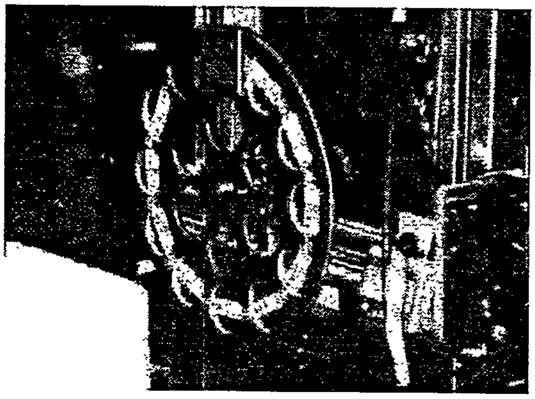

Figure 46. Sample wheel mounted on stepper motor rotation and translation system. The phosphor is mounted at the top of the wheel.

There were six main goals for the experiments begun this year. The first of these was to fine-tune the irradiation dose to optimize the J$_c$ at 75 K in an applied field of 1-2 T applied normal to the tape plane. This set of experiments used 85-filament production Bi-2223/Ag tape (I$_c$ ~30 A, J$_c$ ~20 kA/cm^2) produced by ASC, very similar to the tapes irradiated by our group in previous years. Four tapes each were irradiated to produce nominal defect densities Bφ of 0.7, 1.1, 1.4, and 1.7 T. These tapes will be characterized for defect density spatial profile, half life, and J$_c$ performance.

The second set of experiments is designed to examine the effect of proton irradiation induced columnar defects in the latest generation, high-performance research-grade Bi-2223/Ag tape. These tapes are also multifilament conductors produced by roll only deformation processing and have I_c ~55 A and J_c ~45 kA/cm^2. Specifically, we wish to study the effect of the in-field enhancement of J_c (relative to that of unirradiated tape) on the absolute value of J_c in self field. The reference samples are the production 85-filament tape of the first experiment described above. One tape each at nominal defect densities of 1.1 and 1.7 T has been produced.

The third experiment was a study of the role of percolation paths for supercurrent in tapes with a very high density of columnar defects. In our previous set of experiments (irradiation and measurements in FY96), we found that multifilament tapes irradiated to doses higher than $B\varphi$ ~1.5 T showed decreases in the self field J_c and rapid decrease in J_c at low fields, evidence of weak link behavior. We postulate that the diameter of the columnar defect may increase at grain boundaries, which are regions of high energy, relative to the grain interior, and that while the intragranular pinning may still be increasing with increasing defect density, the grain boundary degradation ultimately leads to poorer performance. We also showed in FY96 that some of this grain boundary damage could be removed by careful annealing of the tapes.

However, our purpose in the Nov. 1996 irradiations, performed on monofilament Bi-2223/Ag tapes from IGC (nominal I_c ~ 30 A), was to determine if these tapes would behave like the multifilament ones. As more grain boundaries become damaged, the percolation path for supercurrent becomes more restricted. Because the filament size in 85-filament tapes was only 15 μm x 120 μm, weak link behavior might set in at lower defect densities than in a monofilament tape with one to two orders-of-magnitude greater cross-sectional area for current flow. We irradiated monofilament tapes (two each) to defect densities $B\varphi$ of 1.1, 1.7, and 2.4 T to test this hypothesis.

The fourth experiment was the scale-up to irradiation of a component, a double pancake coil made from Bi-2223/Ag tape. This coil had dimensions of 3" OD, 2.25" ID, and 0.25" high (7.6 cm OD, 5.7 cm ID, 0.64 cm high) and a preirradiation I_c of 19.5 A at 77 K. It was irradiated while placed horizontally on a nonmetallic platform (see Fig. 47) that was rotated in the beam at 1 rpm. The beam passed completely through both sides of the coil irradiating the front and back simultaneously. The ~20-hr irradiation resulted in a nominal defect density $B\varphi$ of 1 T.

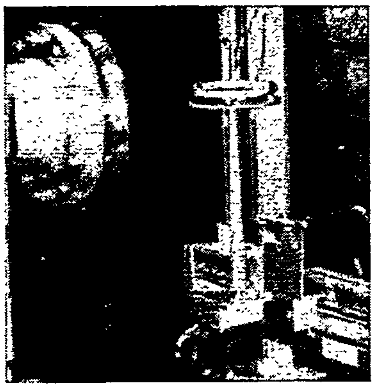

Figure 47. Bi-2223/Ag double pancake coil shown mounted on a support. A clock motor rotates the coil at 1 RPM. The beam tube is visible on the left.

The fifth experiment was to determine the effect of splayed columnar defects on Bi-2223 single crystals grown by Shaoyan Chu in Michael McHenry's group at Carnegie Mellon University. Magnetization experiments on these crystals will allow determination of the intragranular pinning. All of our measurements to date on proton-irradiated specimens have been on polycrystalline Bi-2223/Ag tapes or on single crystal Bi-2212. For the former, it is difficult to deconvolute the intragranular from intergranular contributions to the pinning. For the latter, the physical properties are sufficiently different from those of Bi-2223 that a direct measurement is required to fully interpret the effect of the splayed columnar defects.

The final experiment was to study the effect of splayed columnar defects YBCO films deposited on YSZ single crystal substrates and subsequently patterned into 0.2 mm wide by 5-mm-long bridges. We used a gold driver foil 100-µm thick placed immediately in front of the YBCO samples to generate fission fragments that would penetrate the superconductor. This was necessary because the fission cross for the nuclei in YBCO are all too small to generate an appreciable number of fission reactions. We will study the effects of the splayed columnar defects on both thin and thick films, which from earlier measurements appear to have different kinds or numbers of intrinsic defects. We will also compare these results to that of complementary experiments we are performing, in collaboration with ANL, using heavy ion irradiation to produce parallel columnar defects.

3.2 Systems Technology

3.2.1 AC Loss by Temperature-Difference Calorimetry

(D.E. Daney, H.J. Boenig, J.Y. Coulter, and M.P. Maley, LANL; S. Fleshler, ASC)

Loss measurements on the prototype multi-strand conductor (PMC) provided by ASC were continued this year. The following measurements were completed:

1) With a 2000-A dc power supply we drove the cable into the resistive mode with losses comparable to the ac losses measured previously. Comparison of the I•V product with the calorimetric measurement provided a check on the calorimeter calibration.

2) We passed ac current through the PMC while subjecting it to a dc magnetic field generated by running dc current through the normal conductors. These tests helped clarify our understanding of the large coupling losses we observed in the three-phase configuration.

3) We measured the axial magnetic field inside the PMC. The axial field inside the cable is a measure of imbalance of current between the two helically wound layers; no magnetic field corresponds to equal current sharing.

Figure 48 compares the measured I•V product to the calorimetric measurement. The calorimetric measurement ranged from 15 to 24% greater than the I•V measurement of the loss. We believe the calorimetric measurement more accurately represents the true loss of the cable for two reasons. First, we measured about ±3% noise in the voltage drop that we associate with switching noise in the power supplies. Because the measurement is made on the very steep portion of the I-V curve, positive excursions in current have a much greater contribution to the loss than the reduction caused by negative excursions. Second, with four pairs of voltage taps on 38 tapes, our measured average voltage may differ from the true effective average. The deviation in the measured voltage drop was ±7%.

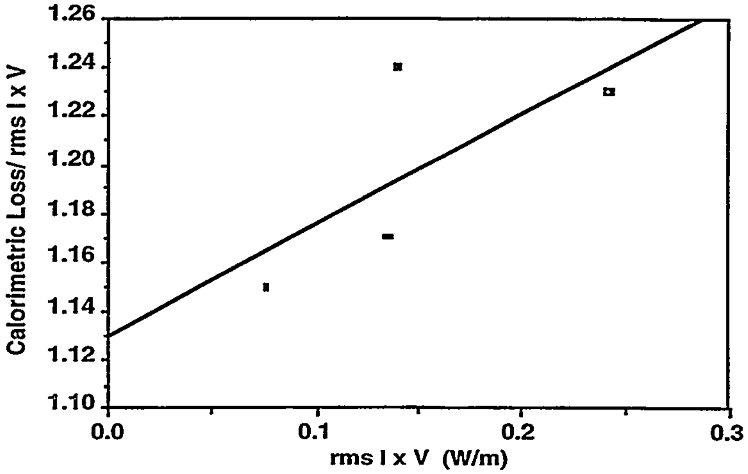

Figure 48. Ratio of calorimetric loss to the measured I•V product versus I•V for PMC#1.

We investigated the effect of dc magnetic fields on ac losses by passing current (in the same direction) through the two normal conductors. The calculated field at the PMC was 2.8 Oe/100 A with current in both conductors. Figures 49 and 50 show the results of the measurements. Previously, we had observed a doubling of the ac loss in going from single-phase to balanced three-phase ac current. In contrast, the ac loss increased by only a few percent in the presence of comparable dc fields.

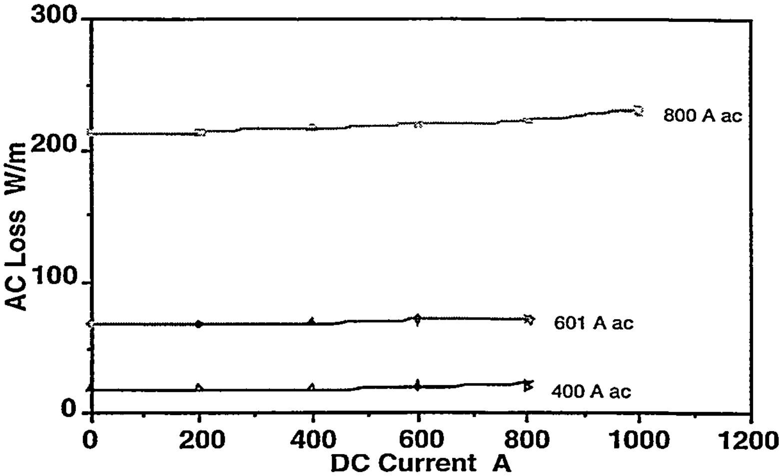

Figure 49. Effect of dc field on ac losses for various PMC ac currents. The field at the PMC was 2.8 Oe/100 A dc.

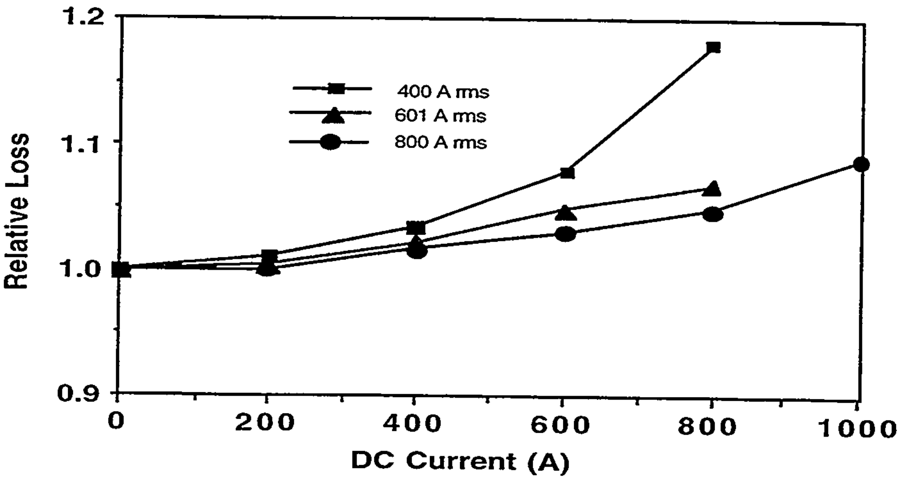

Figure 50. Effect of dc field on ac losses in terms of relative loss (loss with dc field/loss with zero field). The field at the PMC is 2.8 Oe/100 A DC.

The measurements of the ac magnetic field inside the PMC are shown in Fig. 51 for single-phase ac current through the PMC. The mG field levels indicate that the current balance between conductor layers was within 1%. Thus, current sharing between layers in our 1-meter-long PMC was sufficient to justify use of this length cable in the calorimeter.

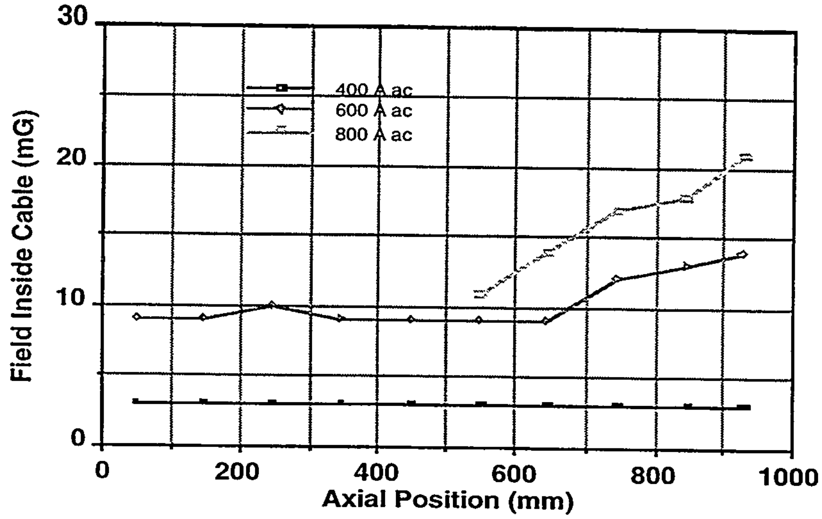

Figure 51. Magnetic field inside PMC#1 versus axial position for several ac currents.

We measured the ac losses of prototype multi-strand conductor number 2 (PMC#2) provided by ASC. This prototype cable differed from PMC#1 in that it had a layer of Kapton® insulation between its two counter wound layers. Otherwise, the construction of the two cables was identical – two helically wound layers of HTS tape (19 tapes per layer) wrapped with opposite pitch on a 28.6-mm diameter G-10 glass-epoxy mandrel. The dc critical current for PMC#2 was 3.7% lower than for PMC #1 (~1300 A compared to 1350 A at 75.5 K). Figure 52 summarizes the results of the single-phase measurements, and Figure 53 presents the results of the 3-phase measurements of ac loss. The conductors are spaced on a 10-cm equilateral triangle.

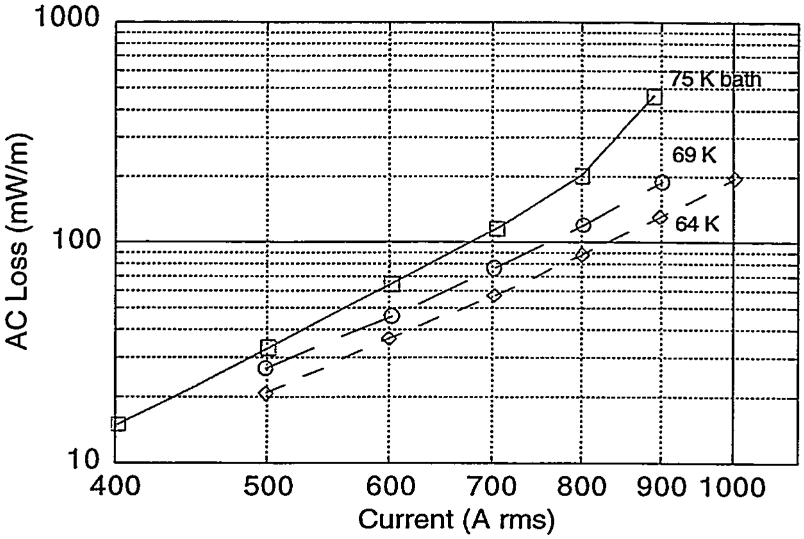

Figure 52. Single-phase losses of PMC#2.

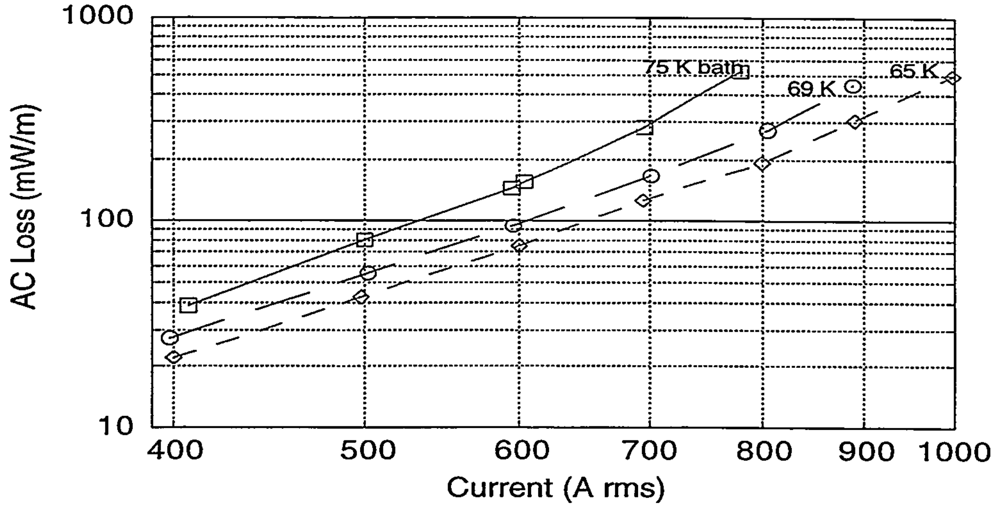

Figure 53. Three-phase losses of PMC#2.

Figure 54 compares the ac losses of the two cables for a 75 K bath temperature. As illustrated by the figure, the performance of the two cables is nearly identical. The upturn in the loss curves at higher currents is primarily due to the rise in the average cable temperature with rising current. Both the cable end temperature and the temperature rise in the cable increase with current.

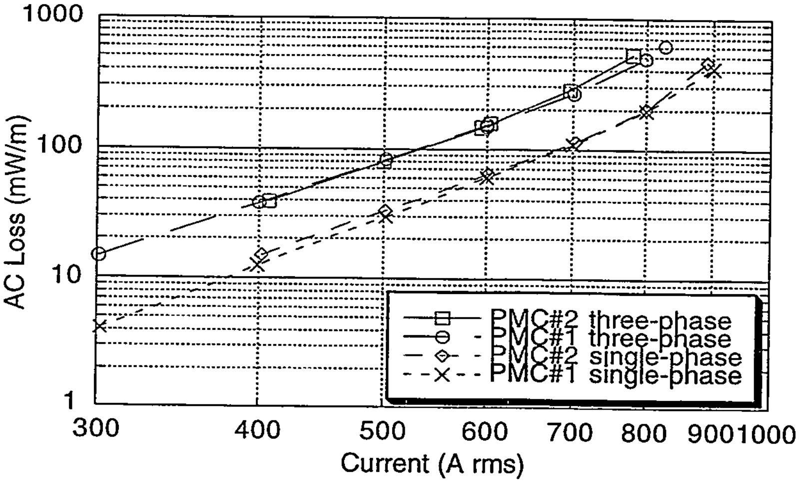

Figure 54. Comparison of ac losses of PMC#1 and PMC#2 for a 75 K bath temperature.

Figures 55a-c give the three-phase loss measurements corrected to constant cable temperature. The corrected single-phase loss measurements are similar. The corrections to constant cable temperature were generated empirically. A table of dq/dT was generated from the uncorrected data, and the correction was obtained by multiplying the difference between the average cable temperature and the correction temperature by the appropriate dq/dT.

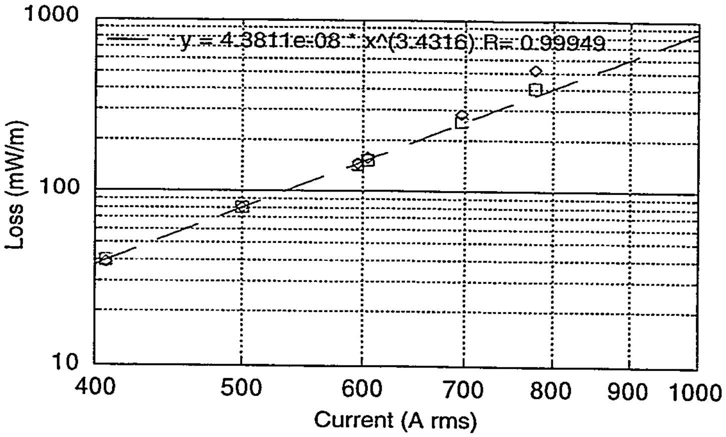

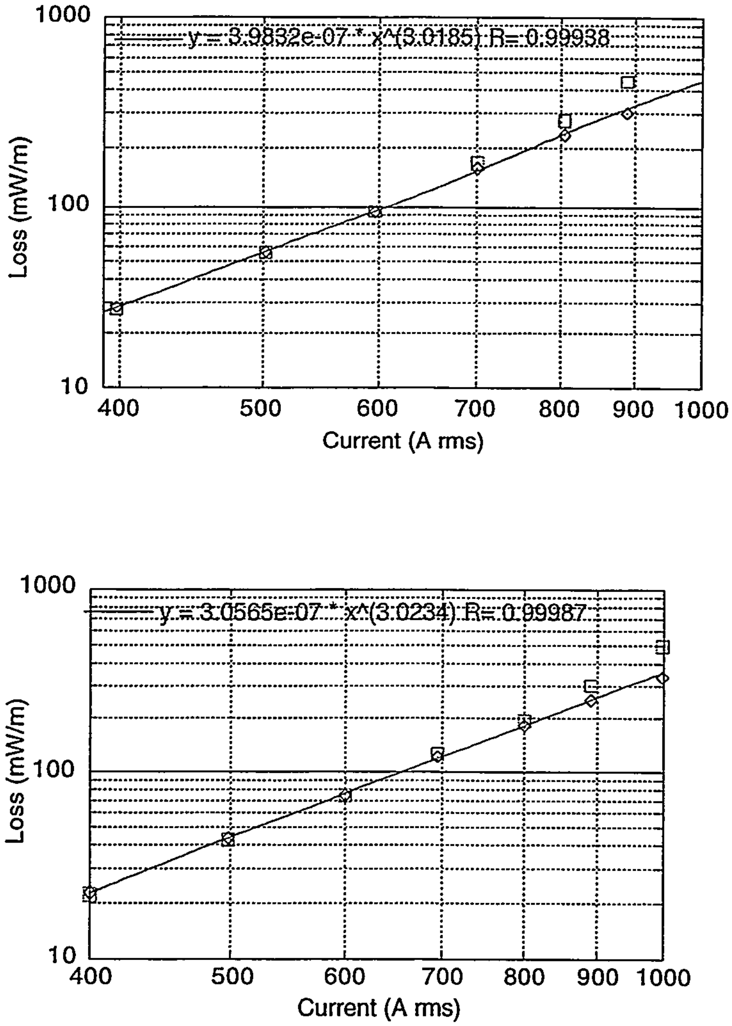

Figure 55. Three-phase losses measured with: a) a 75 K bath temperature (corrected to 76 K), b) a 69 K bath temperature (corrected to 70 K), c) a 64 K bath temperature (corrected to 65 K). The diamonds are uncorrected data, the squares are corrected. The highest point was omitted from the curve fit because of its large correction.

The calibration of the calorimeter by means of an electrical heater located at the cable mid-point is illustrated in Fig. 56. The details of the calorimeter theory have been discussed in previous reports, and the quantity determined by the calibration is the effective product of the thermal conductivity times the cross sectional area of the composite cable. This calibration is performed daily to maintain accuracy in the results.

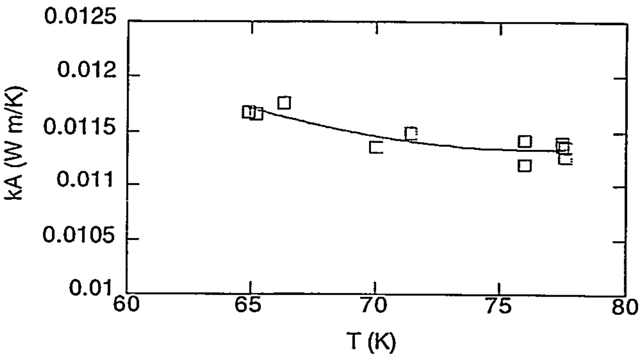

Figure 56. Calibration of the calorimeter with PMC#2.

We completed our characterization of prototype multi-strand conductor No. 2 (PMC#2) provided by ASC. Measurements included dc critical current of the cable over the temperature range 65 K to 77 K, three-phase losses with conductors spaced on 20-cm centers (previous three-phase measurements were with 10-cm spacing), and axial magnetic field inside the cable. An eight-layer cable fabricated by Pirelli Cavi S.p.A. is now installed in the calorimeter, ready for testing.

I-V measurements on PMC#2 taken at a temperature of 65 K are illustrated in Fig. 57, and the dc critical current measurements are summarized in Fig. 58.

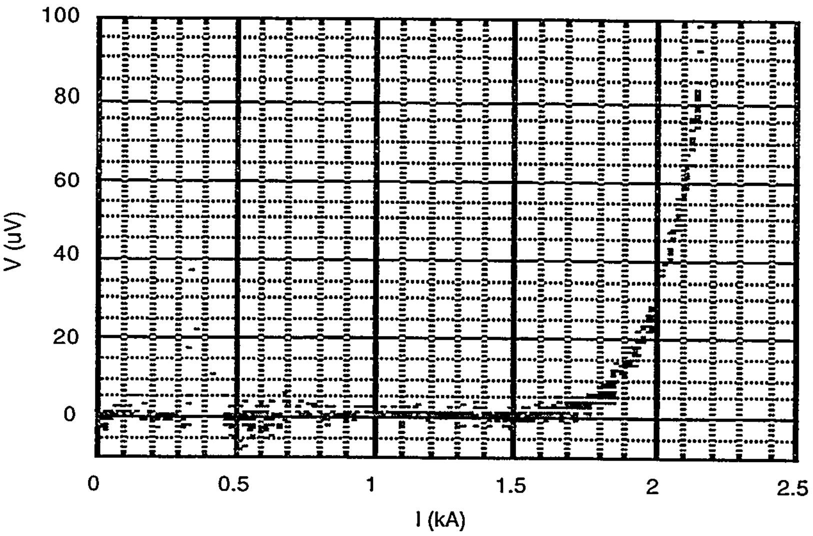

Figure 57. Measured I-V curve for PMC#2 at 65 K. Spacing between voltage taps is 67 cm, and the 1 µV/cm dc critical current is 2115 A.

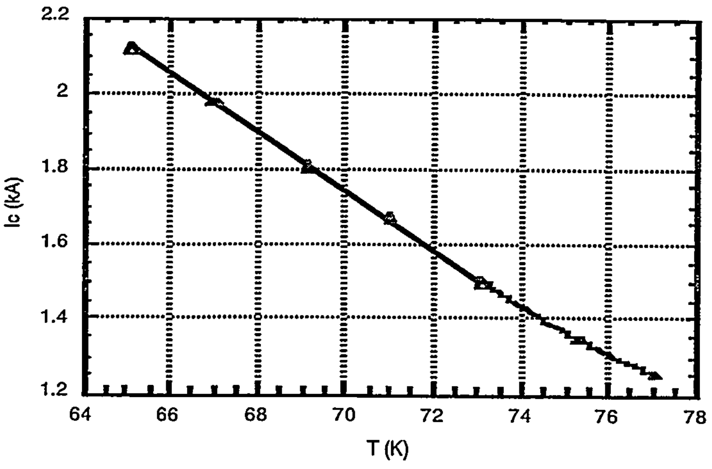

Figure 58. DC critical current for PMC#2 as a function of temperature.

We measured three-phase losses at 75 K and 69 K bath temperatures. The 69 K bath measurements, corrected to a fixed cable temperature of 70 K, are given in Fig. 59. The normalized ac loss (loss/single-phase loss) versus $1/R^2$ is presented in Fig. 60 for a current of 700 A rms. Here, R is spacing of the conductors, which are arranged in an equilateral triangle, and $1/R = 0$ is single phase. The field imposed by the other two phases goes as $1/R$, but the loss scales as $\sim I/R^2$.

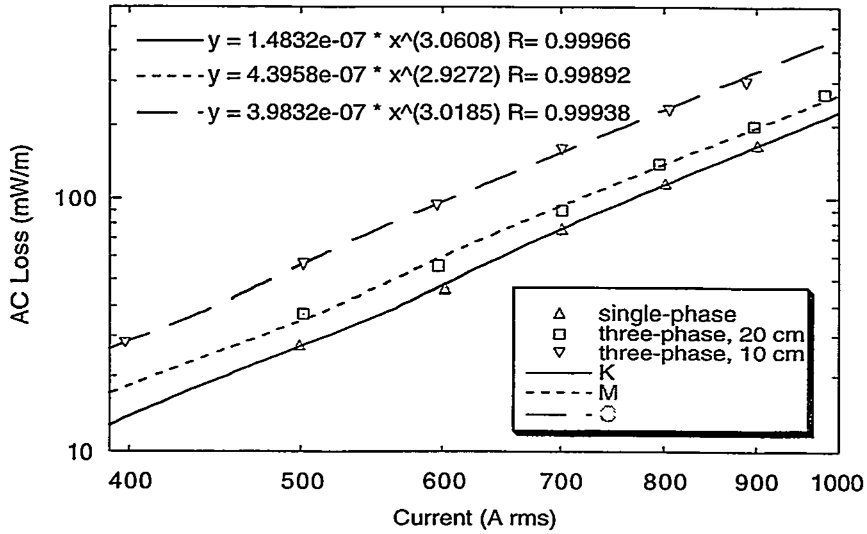

Figure 59. AC loss in PMC#2 for 10- and 20-cm three-phase conductor spacings and for single-phase current. The measurements are corrected to a fixed cable temperature of 70 K.

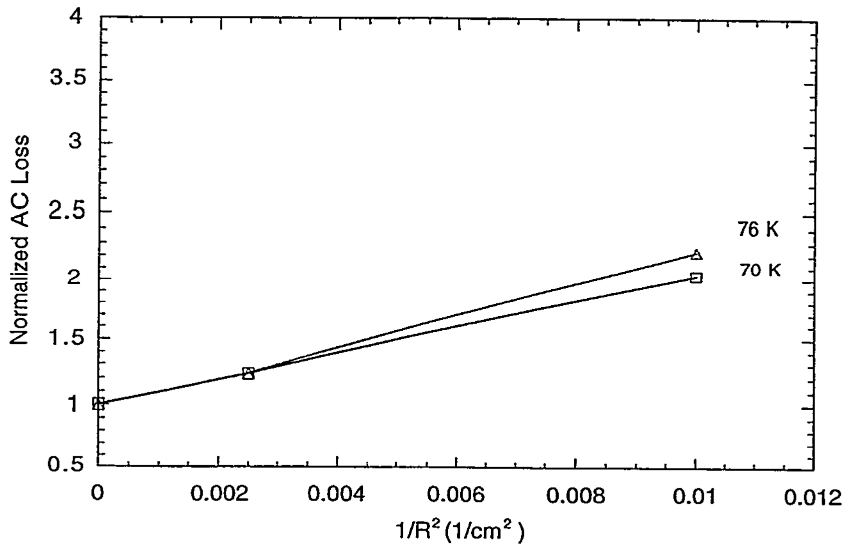

Figure 60. Normalized ac loss versus I/R^2.

The axial magnetic field inside the cable is a function of the current imbalance between conductor layers. We calculate that 1 Gauss equals an imbalance of 25 A in PMC#2. Figure 61 shows the measured axial magnetic field at the axial mid-point of the 1-meter-long cable as a function of current. The measurements are made with an 800-turn pick-up coil. Figure 62 shows the measured variation of field with axial position.

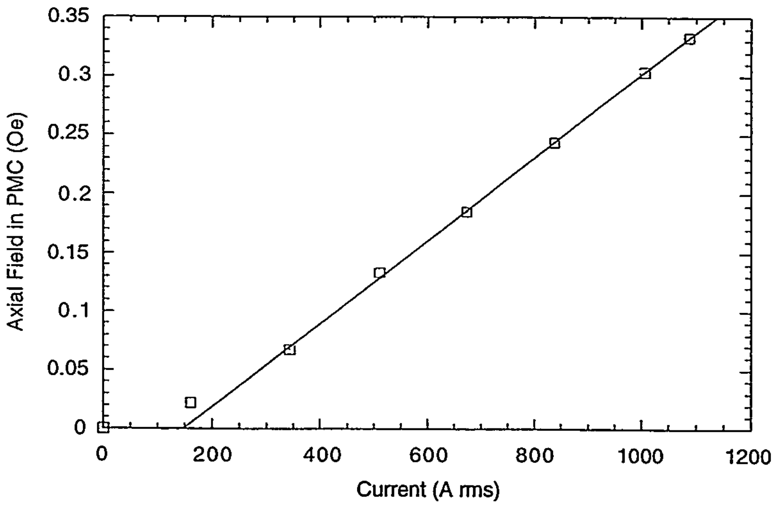

Figure 61. Axial magnetic field near the axial center of PMC#2.

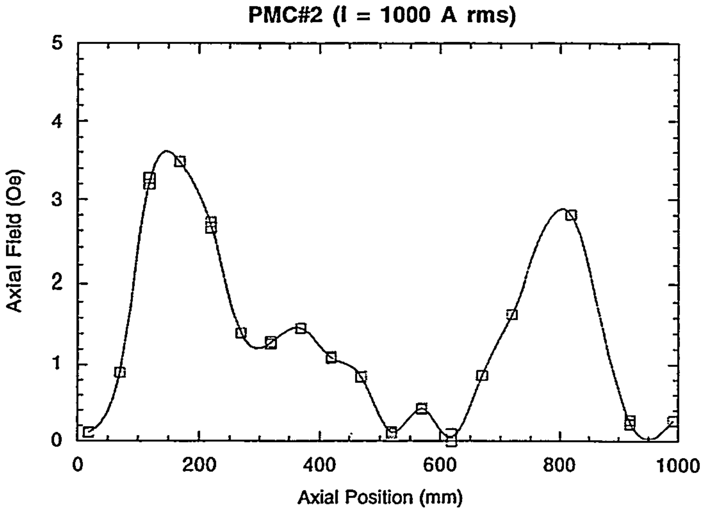

Figure 62. Axial field in PMC#2 at 1000 A rms as a function of axial position.

We began measurements on the Pirelli 8-layer cable. It is composed of eight helically wound layers (15 tapes per layer) with alternate layers wrapped with opposite pitch so that the net azimuthal component of current in the cable is zero. As with the two-layer PMC's tested previously, the cable is 1-meter long, and the tapes are soldered to copper end connectors. Because the test cable is a section taken from a longer, machine-wrapped cable, the tape packing density is somewhat lower than for the hand-wrapped PMC's.

Figure 63 compares single-phase losses on the Pirelli 8-layer cable to those for PMC #2 prepared at ASC. The measurements were made with a 75 K bath temperature, and corrected to a constant cable temperature of 76 K. The slope of the 8-layer cable loss curve is 3.3 compared to 3.8 for the 2-layer PMC. At higher currents, the losses in the 8-layer cable fall below those for the 2-layer PMC.

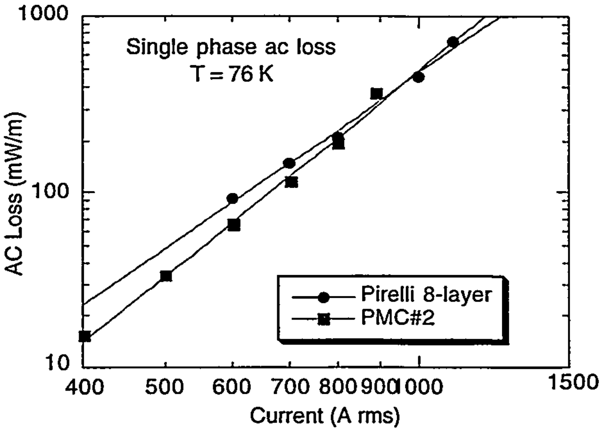

Figure 63. Comparison of ac losses for eight-layer and two-layer cables. The measurements are corrected to a cable temperature of 76 K.

In the next year we plan to measure the losses at reduced temperatures with eight layers, then strip off the top four layers and repeat the measurements.

3.2.2 Development of a HTS Fault Current Limiter

(J.L. Smith, W.L. Hults, and J.Y. Coulter, LANL; E.M. Leung and G.W. Albert, Lockheed Martin; J.G. Hoehn, Jr., Intermagnetics General Corp. [IGC]; S. Ahmed, Southern California Edison [SCE])

The overall goals of this DOE Superconductivity Partnership Inititative project (Phase 2) are the development and demonstration of a utility-class, three-phase, 15-kV fault current limiter (FCL), which uses in each phase a Bi2223 high-temperature superconducting coil operating at 40 K. The FCL will be rated at 17 kV and 45 kA, that is 765 MVA, and will reduce a fault current by 80%. The device should double as a fast half-cycle circuit breaker for bus-tie applications. A team of four institutions is contributing to this effort: Lockheed Martin is the system integrator with collaborators IGC as the manufacturer of the HTS coils, SCE for specification development and FCL field evaluation, and LANL for design analysis and prototype testing. With its high-power rating, successful operation of this FCL over several months on the SCE substation should qualify the HTS FCL for practical use by electrical utility companies.

In the past year, LANL's testing program included evaluation of a large-diameter Bi2223 pre-prototype coil for transient dc electrical and thermal properties at liquid-nitrogen (LN2) temperature and determination of the current distribution amongst the flat untwisted conductors. Testing was directed towards verifying coil and conductor design features and integrity. We determined that the inner coil windings take the initial charging current when charging at a rate of 14 A/s, and that current moves to the outer winding with period of 20 s. As charging current exceeded ~60% of the critical current I_c, the current level in the inner windings saturated and additional current was uniformly distributed amongst the windings. Below I_c, dc current sharing between the inner and outer windings was determined by inductance. Particulars on these experiments are presented in the following section.

The results from the coil evaluation were incorporated into the design of the larger, prototype HTS coil. Plans for further development of a large coil test facility were defined. In addition, modeling of the current limiter was successfully conducted.

LANL plans for FY1998 are to develop a capability for characterization of large HTS coils as a function of current, temperature, and magnetic field.

3.2.2.1 Pulsed-Current Test of Pre-Prototype Fault-Current-Limiter Coil

(J.L. Smith, W.L. Hults, and J.Y. Coulter)

The pre-prototype coil was wound from 36 layers of silver-sheathed, powder-in-tube Bi-2223 superconductor in 54 turns. It was 48 cm in height and diameter, and the critical current exceeded 228 A in LN2.

Because powder-in-tube conductors cannot be twisted, there was a concern that so much current will flow in the innermost conductor in the stack, because of its lower inductance, that it would burn out before the current could distribute more uniformly amongst all of the conductors. The pre-prototype coil was constructed with an insulator between the 18th and 19th layer of conductor so that the current distribution could be measured.

Testing of the coil was conducted within a custom-made dewar of 66-cm inner diameter. A pair of current leads was made from 40 strands of 14-gauge insulated copper wire, and current sensors were assembled from Honeywell sensors with Lake Shore cryogenic Hall probe replacements and calibrated at LN2 temperature. One current sensor was put on each half of the conductor stack. The coil was slowly cooled until it was submerged in liquid nitrogen.

A comb of current pulses of increasing magnitude was applied to the coil. The pulses were on and then off with ~40 seconds allowed for the currents to settle down. The current was changed as fast as the supply would adjust at a rate of 14 A/sec. For low currents, the current in the inner turns redistributed into the outer turns with a time constant of ~20 s, as shown in Fig. 64. As expected, the current went negative in the inner turns when the overall current was changed to zero. Figure 65 shows the current behavior in the outer coils, and Figure 66 shows the sum of the two currents compared to what is supplied.

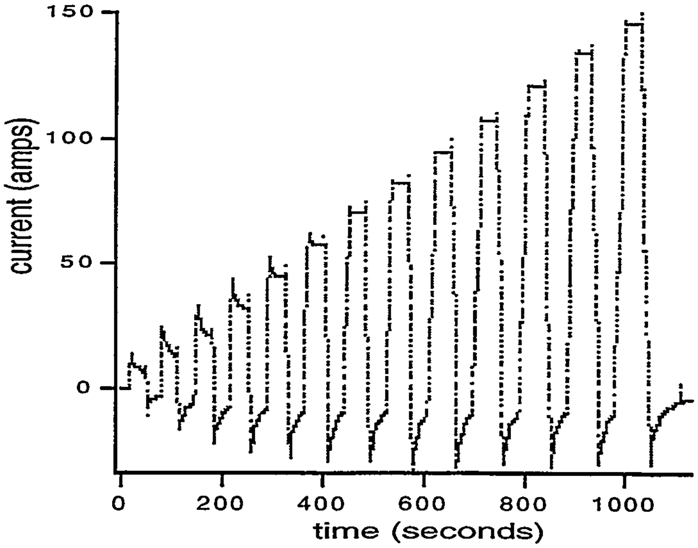

Figure 64. Current versus time in the inner turns of the coil, which have relatively low inductance. The transients show the current transferring to the outer turns at low values and becoming increasingly uniform close the critical current near 100 A.

At currents below about 70 A, these experiments exhibited how two nested coils behave under transient conditions. Above ~80 A in each coil, the transient induced some voltage drop on turns carrying higher than their individual critical currents. A uniform current distribution was evident between the inner and outer turns, that is, the pulses above ~80 A had flat tops as seen in each of the figures. This was the desired result, and these tests confirmed that twisted conductors were not necessary. As the current approached I_c anywhere in the coil, the increasing resistance shifted the current into other turns. The coils performed as designed.

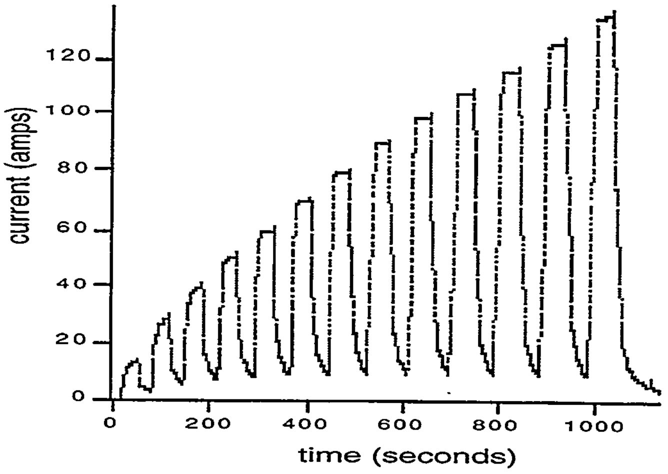

Figure 65. Current versus time in the outer turns of the coil, which have relatively high inductance. The transients at low currents show the current transfer from inner to outer turns.

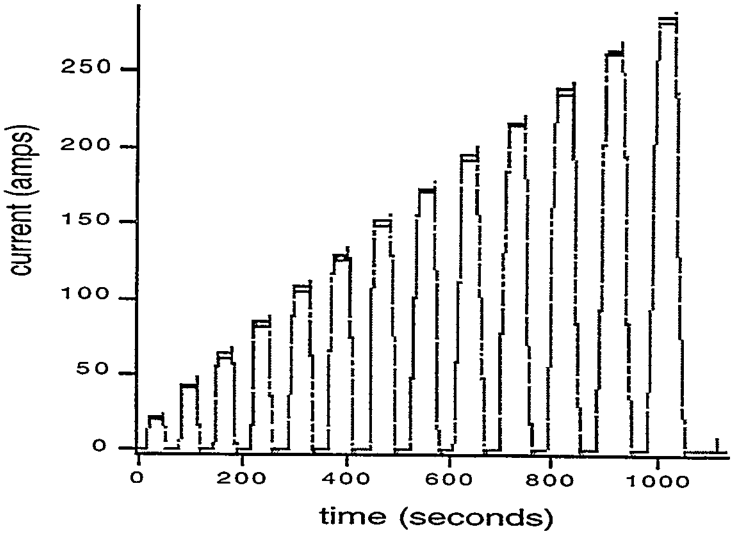

Figure 66. Comparison of two currents: 1) Sum of current plotted in Figs. 64 and 65 and 2) the current supplied to the coil. The two agree within the accuracy of measuring the currents.

3.2.3 HTS High-Gradient Magnetic Separation

(M.A. Daugherty, F.C. Prenger, E.W. Roth, D.E. Daney, D.D. Hill, L.A. Worl, D.D. Padilla, H.J. Boenig, W.L. Hults, J.Y. Coulter and D.E. Peterson, LANL; J.A. Selvaggi, D.L. Cottrell and T.H. Falconer, Eriez Magnetics)

A series of HGMS experiments was performed to show that HTS magnetic separators are capable of separations currently being performed with low temperature superconducting and conventional HGMS systems.

A sample of Kaolin clay was obtained from J.M. Huber Corp. The clay was prepared for magnetic separation tests by the supplier. Sample preparations immediately prior to testing included stirring the clay for several hours to ensure proper dispersion and screening with a 325 mesh sieve to remove any foreign matter. Equipment used for the tests included the HTS magnetic separation system, canisters packed with stainless steel wool, a peristaltic pump and miscellaneous items for testing. Three canisters were used for testing. These consisted of 1" OD PVC tubing which was used to hold the matrix. The ends were sealed to retain the matrix, which consisted of 35-µm-diameter stainless-steel wool packed to a density of 6%. The matrix lengths were 6”, 4”, and 2” (15, 10, and 5 cm). These canisters were inserted into the warm bore of the separator and clamped into position.

While the magnet was energized, the clay was pumped through the bottom of the vertically installed canister with a peristaltic pump operating at a constant feed rate. A total of 10-canister volumes were collected for each test. After the clean clay was collected, the magnet was de-energized and the magnetic impurities were rinsed from the matrix with water until clean water was observed at the end of the canister. Two magnetic field strengths were utilized, 1.6 and 2.0 T; these strengths are similar to those used in actual field applications. Figure 67 shows results of testing performed by J.M. Huber Corp., a large customer for this type of commercial product. The brightness of the feed was found to be approximately 81. Testing shows that the largest brightness increase, after 10 canister volumes, was obtained with the 6" matrix at 2.0 T. The trend that was discovered is that as the matrix length is reduced, the brightness increase is reduced. From Fig. 67 it is observed that the brightness level for a 2" matrix at 2.0 T is approximately the same as the 6" matrix at 1.6 T. This further substantiates earlier work performed by Eriez Magnetics.

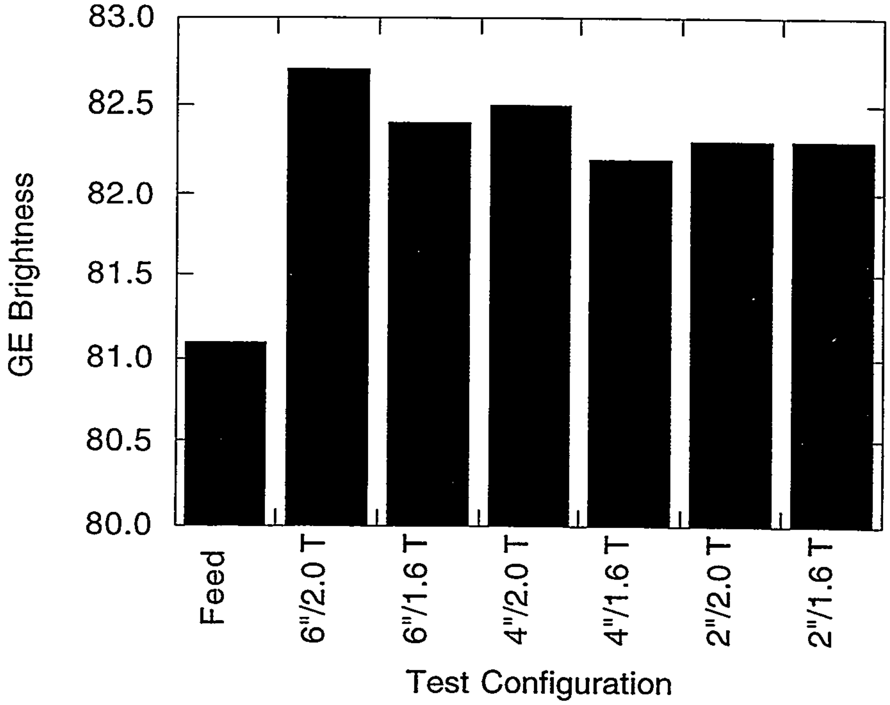

Figure 67. Separation (brightness) test results for kaolin clay using different configurations of magnetic field and matrix length.

We conclude that the separation achieved with this separator is similar to the separation that clay producers are achieving now with conventional and low temperature superconducting HGMS systems. The level of brightness increase is lower due to the shorter matrices tested in the prototype. Current HGMS designs use a 20" matrix height to achieve an average brightness improvement of 2 to 2.5 points higher than the feed.

This machine, which is economically cooled using a simple and inexpensive cryocooler, represents a positive future for HGMS. A HTS HGMS will offer kaolin producers lower operating costs and the possibility of cleaner clay by going to higher fields economically, which ultimately means a larger profit per ton of clay.

We have prepared the Applications Laboratory at the STC for tests and demonstrations of the HTS high gradient magnetic separator using depleted uranium. We will conduct experiments on the effectiveness of the separation of depleted uranium from water and/or soil mixtures to simulate environmental remediation applications. The required industrial and radiation safety procedures and controls have been implemented and the necessary safety approvals have been obtained. The tests and demonstrations will be conducted during the next quarter.

High-gradient magnetic separation tests were conducted on mixtures of depleted uranium in water and in water with kaolin clay added to simulate soil. The tests were run in an 8-inch (20-cm)-long matrix of magnetic stainless steel wool at a superficial velocity of 1 cm/s. The HTS magnet was operated at a temperature of 30 K and a field of 1.7 T.

The initial uranium concentrations were 200 ppm for the water sample and 494 ppm for the water with kaolin sample. On each run a sample of the feed was reserved for analysis. The feed was then run through the matrix with the magnet energized and the output of the first pass was collected. The magnet was then de-energized and the matrix was cleaned by back flushing with deionized water. A portion of the output from the first pass was then run through the matrix again to obtain the second pass sample.

The samples were analyzed using an IPC mass spectrometer. As shown in Fig. 68 the concentrations after one separation pass for both samples are near the lower detection limit of 1 ppm. Reductions in concentration of greater than two orders of magnitude were thus achieved in one pass. Because the samples after the first pass are near the detection limit it is difficult to determine the effectiveness of the second separation pass. A representative flow chart for the separation tests is shown in Fig. 69.

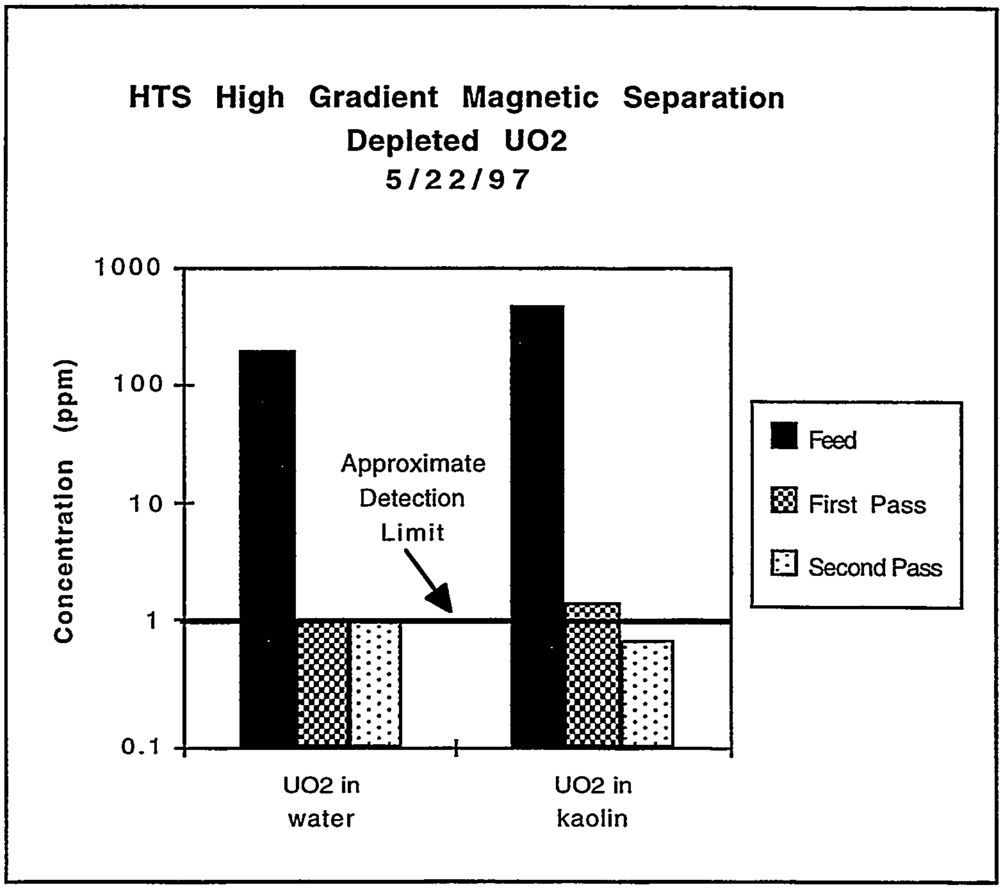

Figure 68. Depleted uranium oxide (UO2) high-gradient magnetic separation test results (5/22/97) as analyzed by mass spectrometry.

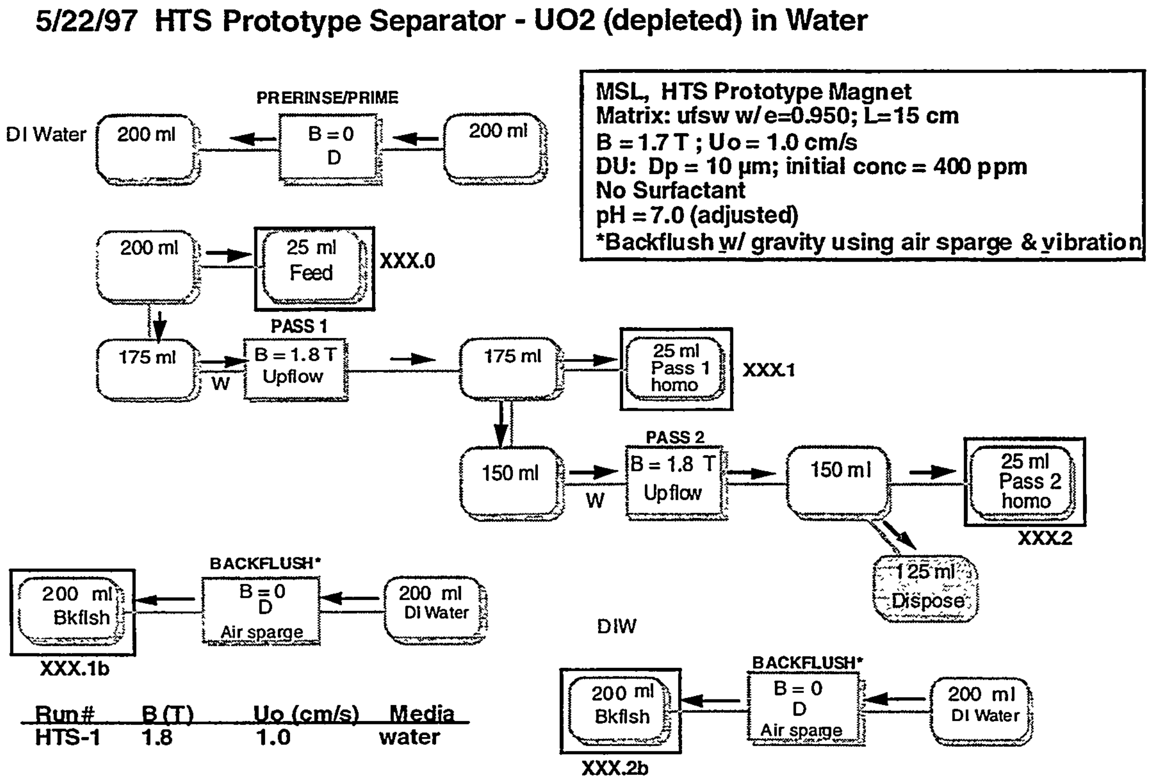

Figure 69. Flow chart for operation of magnetic separation of uranium oxide.

We are upgrading the current leads on the high gradient magnetic separator from the original 100-A design. The design target for the new leads is 150 A for the copper upper leads and the heat pipe thermal intercept. The new design will allow us to operate at higher magnetic fields (up to ~2.5 T compared with the present 1.7 T at 100 A) without overheating the copper components of the current leads. As part of the upgrade we have also completed a redesign of the epoxy electrical isolation joint on the heat pipe thermal intercept. A prototype of the new design is under fabrication and will be used to test the assembly procedures for the epoxy joint. The new design is shown in Fig. 70.

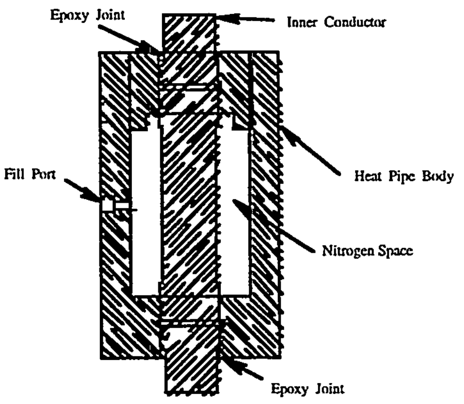

Figure 70. Heat pipe schematic showing epoxy joint.

4. This Year's Publications

4.1 Refereed Papers Submitted

"Cryogenic Equipment (62 pages of text, 83 references and 72 figures),"
D.E. Daney,
Submitted to **Handbook of Cryogenic Engineering**, J.G. Weisend II, ed., (Taylor & Francis, London).

"Powder Diffraction Data of $SmBa_4Cu_3O_{8.5+d}$,"
Y.T. Zhu, P.S. Baldonado, E.J. Peterson, D.E. Peterson, and F.M. Mueller,
Submitted to *Powder Diffraction* (publ. in Vol. 12, pp. 242-244, Dec 1997).

"Influence of Deposition Rate on the Properties of Thick $YBa_2Cu_3O_{7-d}$ Films,"
S.R. Foltyn, E.J. Peterson, J.Y. Coulter, P.N. Arendt, Q.X. Jia, P.C. Dowden, M.P. Maley, X.D. Wu, and D.E. Peterson,
Submitted to *J. Materials Res.* (publ. in Vol. 12, pp. 2941-2946, Nov 1997).

"The Effects of Variable Oxygen Partial Pressures During Bi-2223 Tape Processing,"
T.G. Holesinger, J.F. Bingert, J.O. Willis, V.A. Maroni, A.K Fischer, and K.T. Wu,
Submitted to *J. Materials Res.* (publ. in Vol. 12, pp. 3046-3054, Nov 1997).

"Single and Three-Phase Ac Losses in HTS Superconducting Power Transmission Line Prototype Cables,"
D.E. Daney, H.J. Boenig, M.P. Maley, J.Y. Coulter, and S. Fleshler,
Submitted to Proc. of Intl. Cryogenic Materials Conf., Portland, July 28-Aug 1 1997; To appear in Advances in Superconductivity, Vol.44.

"YBCO/YSZ Coated Conductors on Flexible Ni Alloy Substrates,"
P.N. Arendt, S.R. Foltyn, J.R. Groves, R.F. DePaula, P.C. Dowden, J.M. Roper, and J.Y. Coulter,
Submitted to *Appl. Superconductivity.*

"Optimization on Processing Parameters for Bi(Pb)-2223 Superconducting Tapes,"
N.V. Vo, J.O. Willis, D.E. Peterson, H.K. Liu, and S.X. Dou,
Submitted to *Physica C* (publ. in Vol. 299, pp. 315-326, Apr 20, 1998).

"Variation of Oxygen Content and Crystal Chemistry of $YBa_4Cu_3O_{8.5+d}$,"
Y.T. Zhu, P.S. Baldonado, E.J. Peterson, Y.S. Park, A. Manthiram, D.P. Butt, D.E. Peterson, and F.M. Mueller,
Submitted to *Physica C* (publ. in Vol. 298, pp. 29-36, Mar 20, 1998.)

"Fabrication and Characterization of High-T_c Superconducting Continuous-Tube-Forming/Filling Bi(Pb)-2223/Ag Composites and Coils,"
E.W. Collings, N.V. Vo, J.O. Willis, D.E. Peterson, H.K. Liu, and S.X. Dou,
Submitted to *Materials and Mfg. Processes* (publ. in Vol. 13, pp. 337-357, 1998).

"Evidence of pair-breaking Pr(Ba) in $Y_{1-y}Pr_yBa_2Cu_3O_7$,"
H.A. Blackstead, J.C. Cooley, J.D. Dow, S.K. Malik, W.L. Hults, D.B. Pulling, J.L. Smith, and W.B. Yelon,
Submitted to *J. Phys. Chem. Solids.*

4.2 Other Publications and Conference Abstracts

"'Secure Bus' Disturbance-Free Power at the Utility Substation Level,"
H.J. Boenig and W.H. Jones,
Paper for the 49th Annual Power Distribution Conf., Oct 21-23, 1996, Univ. of Texas at Austin (unpubl.).

"Continuous Processing of YBCO/IBAD Coated Conductors in Flexible Substrates,"
S.R. Foltyn, P.N. Arendt, P.C. Dowden, J.R. Groves, J.Y. Coulter, and E.J. Peterson, Extended Abstracts for *the 1997 Intl. Workshop on Superconductivity*, Big Island, Hawaii, June 15-18, 1997, p. 68.

"Critical Current and Flux Pinning in Biaxially Textured YBCO Thick Film Conductors,"
J.O. Willis, M.P. Maley, J.Y. Coulter, P.N. Arendt, S.R. Foltyn, and H. Safar,
Abstract for the Materials Res. Soc. 1997 Spring Meeting, Apr 1-2, 1997, San Francisco.

"Critical Current Density Dependence on Angle of Heavy Ion Irradiation for YBCO Coated Conductors,"
J.Y. Coulter, M.P. Maley, P.N. Arendt, S.R. Foltyn, H. Safar, K.E. Gray, and D.G. Steel,
Abstract for the Materials Res. Soc. 1997 Spring Meeting, Apr 1-2, 1997, San Francisco.

"X-Ray Diffraction Analysis of BSCCO and YBCO Superconducting Films,"
E.J. Peterson, P.N. Arendt, J.Y. Coulter, P.C. Dowden, S.R. Foltyn, J.R. Groves, W.L. Hults, J.L. Smith, J.O. Willis, and P.J. Kung,
Abstract for the Amer. Ceramic Soc. 99th Annual Mtng., Cincinnati, May 4-7, 1997.

"Superconductivity the Market - A Description of the Road Map of Hurdles and Promises,"
J.L. Smith,
Abstract for talk, Royal Institute of Technology, Stockholm, May 15-16, 1997.

"Single and Three-Phase AC Losses in HTS Superconductive Power Transmission Line Prototype Cables,"
D.E. Daney, H.J. Boenig, M.P. Maley and S. Fleshler,
Abstract for the Intl. Cryogenic Materials Conf., Portland, July 28-Aug 1, 1997.

"Longer Length Fabrication Issues for Production of Biaxially Aligned YBCO/YSZ/Ni Tapes Using the IBAD Method,"
J.R. Groves, P.N. Arendt, S.R. Foltyn, R.F. DePaula, P.C. Dowden, V. Gurule, J.M. Roper, E.J. Peterson, and J.Y. Coulter,
Abstract for the Materials Res. Soc. 1997 Fall Meeting, Boston, Dec 1-5, 1997.

"Commercialization Issues for YBCO/IBAD Coated Conductors,"
S.R. Foltyn, P.N. Arendt, P.C. Dowden, J.R. Groves, J.M. Roper, J.Y. Coulter, E.J. Peterson, W.L. Hults, Q.X. Jia, M.P. Maley, J.L. Smith, and D.E. Peterson,
Abstract for the Materials Res. Soc. 1997 Fall Meeting, Boston, Dec 1-5, 1997.

"Compressive Annealing of BSCCO 2223 Superconductive Tapes,"
Y.T. Zhu, P.S. Baldonado, J.F. Bingert, T.G. Holesinger, and D.E. Peterson,
Abstract for the 1998 Spring Meeting of The Minerals, Metals, & Materials Soc., San Antonio, Feb 15-19, 1998.

"High Temperature Superconductors: Ion-Beam Assisted Deposition of Biaxially Aligned Template Films of YSZ for Long Length Coated Conductors,"
J.M. Roper, P.N. Arendt, R.F. DePaula, P.C. Dowden, S.R. Foltyn, J.R. Groves, and B.T. Rael,
Abstract submitted to the NM Network of Women in Science and Eng. Tech. Symposium and Annual Meeting, Las Cruces, NM, Oct 17-19, 1997.

"High Field, High Temperature Performance of Bi-2223 Tapes with Splayed Columnar Defects,"
J.O. Willis, J.Y. Coulter, M.P. Maley, T.G. Holesinger, J.L. Ullmann, H.F. Safar, S. Fleshler, and G.N. Riley, Jr.,
Abstract for the Materials Res. Soc. 1997 Fall Meeting, Boston, Dec 1-5, 1997.

"Isothermal Melt Processing of Bi-2212 Wires & Tapes with MgO and Al_2O_3 Additions for Grain Refinement in the Partial Melt,"
T.G. Holesinger, N.V. Vo, P.S. Baldonado, J.F. Bingert, B.L. Bingham, J.Y. Coulter, J.O. Willis, and D.E. Peterson,
Abstract for the Materials Res. Soc. 1997 Fall Meeting, Boston, Dec 1-5, 1997.

"Magnetic and Transport Behavior of Isothermal melt Processed MgO and Al_2O_3-Doped Bi-2212 Composites,"
N.V. Vo, T.G. Holesinger, J.F. Bingert, J.Y. Coulter, J.O. Willis, and D.E. Peterson,
Abstract for the Materials Res. Soc. 1997 Fall Meeting, Boston, Dec 1-5, 1997.

"Microstructural and Transport Properties of Bi-2223 AgCuPbAu/Mg Composites with Ag Particle Additions,"
N.V. Vo, T.G. Holesinger, J.F. Bingert, B.L. Bingham, W.L. Hults, J.L. Smith, R. Zhou, J.Y. Coulter, J.O. Willis, and D.E. Peterson,
Abstract for the Materials Res. Soc. 1997 Fall Meeting, Boston, Dec 1-5, 1997.

4.3 Refereed Papers Published

"Quantitative Analysis of the Effects of Strain-State on the Microstructure and J_c of BSCCO Tapes,"
W.R. Blumenthal, Y.T. Zhu, R.J. Sebring, T.C. Lowe, and R.J. Asaro,
in **High Temperature Superconductors: Synthesis, Processing, and Large-Scale Applications**, U. Balachandran, P.J. McGinn, and J.S. Abell, eds. (The Minerals, Metals, & Materials Soc., Warrendale, PA), 1996, p.71.

"Alternative Sheath Materials for Bi-2223 Tapes,"
J.D. Cotton, G.N. Riley, Jr., and M.D. Teplitsky,
in **High Temperature Superconductors: Synthesis, Processing, and Large-Scale Applications**, U. Balachandran, P.J. McGinn, and J.S. Abell, eds. (The Minerals, Metals, & Materials Soc., Warrendale, PA), 1996.

"Al_2O_3 Additions for Isothermal Melt Processing of $Bi_2Sr_2CaCu_2O_y$,"
T.G. Holesinger,
J. Materials Res. **11**, 2135 (1996).

"Bi-2212/Ag Tape Conductor and Coil Development,"
G.W. Albert, R. Zhou, E.M. Leung, K.V. Salazar, T.G. Holesinger, M.A. Daugherty, and J.O. Willis,
Advances in Cryogenics Engineering - Materials, Vol. 41A, P. Kittel, ed., (Plenum Press, New York, 1966), p. 419 (1996).

"Assembly and Testing of a Composite Heat Pipe Thermal Intercept for HTS Current Leads,"
M.A. Daugherty, D.E. Daney, F.C. Prenger, D.D. Hill, P.M. Williams, and H.J. Boenig,
Advances in Cryogenics Engineering - Materials, Vol. 41A, P. Kittel, ed., (Plenum Press, New York, 1966), p. 579 (1996).

"Bose Glass Vortex Phase-Transition in Twinned $YBa_2Cu_3O_{7-}$_ Superconductors,"
H. Safar, S.R. Foltyn, Q.X. Jia, and M.P. Maley,
Phil. Mag. B **74**, 647 (1996).

"Interaction of Pancake Vortices with c-Axis Plasmon in Josephson-Coupled Layered Superconductors,"
L.N. Bulaevskii,
J. de Physique **6**, 2355 (1996).

"Line Width of c-Axis Plasma Resonance in Josephson-Coupled Superconductors,"
L.N. Bulaevskii, D. Dominguez, M.P. Maley, A.R. Bishop, O.K.C. Tsui, and N.P. Ong, *Phys. Rev. B* **54**, 7521 (1996).

"Processing Factors for High Critical-Current Density in Bi-2223/Ag Tapes,"
J.O. Willis, R.D. Ray II, J.F. Bingert, D.S. Phillips, R.J. Beckman, M.G. Smith, R.J. Sebring, P.A. Smith, B.L. Bingham, J.Y. Coulter, and D.E. Peterson,
Physica C **278**, 1 (1997).

"NMR and Vortex Lattice Melting in $YBa_2Cu_3O_7$,"
C.H. Recchia, J.A. Martindale, C.H. Pennington, W.L. Hults, and J.L. Smith,
Phys. Rev. Lett. **78**, 3543 (1997).

"Vortices and Plasmons in Inductive Periodic Josephson-Junction Arrays,"
R. Sasik, L.N. Bulaevskii, A.R. Bishop and M.P. Maley,
Phys. Rev. B **55**, 11688 (1997).

"Magneto-Optical Imaging and Current Distributions in High-T_c Superconductors,"
A. Polyanskii, A. Pashitski, A. Gurevich, J.A. Parrell, S. Polak, D.C. Larbalestier, S.R. Foltyn, and P.N. Arendt,
in **Advances in Superconductivity IX**, S. Nakajima and M. Muakami, eds., (Springer-Verlag, Tokyo), pp.469-474 (1997).

"AC Loss Calorimeter for Three-Phase Cable,"
D.E. Daney, H.J. Boenig, M.P. Maley, D.E. McMurry, and B.G. DeBlanc,
IEEE Trans. Appl. Superconductivity **7**, 310 (1997).

"HTS High-Gradient Magnetic Separation System,"
M.A. Daugherty, J.Y. Coulter, W.L. Hults, D.E. Daney, D.D. Hill, D.E. McMurry, M.C. Martinez, L.G. Phillips, J.O. Willis, H.J. Boenig, F.C. Prenger, A.J. Rodenbush, and S. Young,
IEEE Trans. Appl. Superconductivity **7**, 650 (1997).

"Magnetic-Field and Orientation Dependence of the J_c in Bi-2212 Round Wires,"
J.O. Willis, T.G. Holesinger, J.Y. Coulter, and M.P. Maley,
IEEE Trans. Appl. Superconductivity **7**, 2022 (1997).

"Progress in Superconducting Performance of Rolled Multifilamentary Bi-2223 HTS Composite Conductors,"
Q. Li, G.N. Riley, Jr., R.D. Parella, S. Fleshler, M.W. Rupich, W.L. Carter, J.O. Willis, J.Y. Coulter, J.F. Bingert, V.K. Sikka, J.A. Parrell, and D.C. Larbalestier,
IEEE Trans. Appl. Superconductivity **7**, 2026 (1997).

"Studies of Flux Pinning by Proton-Induced Fission Tracks in Multifilamentary Tapes of $(Bi,Pb)Sr_2Ca_2Cu_3O_{10}/Ag$ Superconductors,"
R.C. Budhani, J.O. Willis, M. Suenaga, M.P. Maley, J.Y. Coulter, H. Safar, J.L. Ullmann, and P. Haldar,
J. Appl. Phys. **82**, 3014 (1997).

"Phase Diagram for 1/2 Yb_2O_3-BaO-CuO,"
E. Oniyama, P.G. Wahlbeck, D.E. Peterson, J.Y. Coulter, and E.J. Peterson,
Physica C **288**, 151 (1997).

"NMR Spin Echo Experiments as Probes of Vortex Dynamics in $YBa_2Cu_3O_7$,"
C.H. Recchia, J.A. Martindale, C.H. Pennington, W.L. Hults, and J.L. Smith,
Physica C **282**, 2065 (1997).

5. Patent and License Activity (April 1988 to Present)

5.1 Invention Disclosures and Patent Applications

Designation	Date	Subject	Submitted by
DOE S-80,447 S.N.08/226,624	Opened 4/12/94	Enhancement of Persistent Currents in High T_c Superconductors	P.W. Lisowski et al. (Filed by IBM)
DOE S-80,453 S.N.08/308,034 (continuation) DOE S-87,243	Opened 5/23/94 Filed 9/15/94 Opened 6/12/97	Process of High T_c Powder in Tube Tapes with the Addition of Ag Particles	R. Zhou and J.L. Smith
DOE S-82,620 S.N.08/425,752	Opened 1/06/95 Filed 04/19/95	High-Temperature Superconducting Thick Films	P.N. Arendt, X.D. Wu, and S.R. Foltyn
DOE S-82,621 S.N.08/608,342	Opened 1/06/95 Filed 02/28/96	Bi-2223 PIT Superconductor	T.G. Holesinger
DOE S-82,623 S.N.08/608,069	Opened 1/06/95 Filed 02/28/96	Melt Processing of Superconductors Using Alumina	T.G. Holesinger
DOE S-82,681 S.N.08/508,736 Div.S-87,232 S.N.08/814,306	Opened 7/27/95 Filed 7/28/95 Filed 03/10/97	Cryogenic Deformation of High Temperature Superconductive Composite Structures	P.R. Roberts and W. Michels (ASC); J.F. Bingert (LANL)
DOE S-84,942 S.N.08/597,061	Filed 02/05/96	Structure for HTS Composite Conductors and Manufacture of Same	J.D. Cotton (LANL); G.N. Riley, Jr (ASC)
DOE S-84,959 S.N.60/013,894 Full Application S.N.08/821,264	Filed 03/22/96 Filed 03/20/97	Irradiation Processing of Superconductor Material	J.O. Willis, M.P.Maley, H.F. Safar (LANL); G.N. Riley, Jr. and S. Fleshler (ASC)
DOE S-84,965	Opened 4/8/96	Solid Source MOCVD Delivery System	B.N. Hubert and X.D. Wu
DOE S-87,201 S/.N.08/717,986	Opened 8/23/96 Filed 9/23/96	High Temperature Superconducting Composite Conductor and Method for Manufacture of Same	J.D. Cotton and T.G. Holesinger (LANL); G.N. Riley, Jr.(ASC)
DOE S-87,202	Opened 8/23/96	Process for Enhancement of Properties of Superconducting Composite Materials	T.G.Holesinger (LANL) and G.N.Riley, Jr. (ASC)

5.2 Patents Granted

Designation	Date	Subject	Issued to
DOE S-68,042 S.N.07/276,188 US Pat 4,873,444	Filed 11/23/88 Issued 10/10/89	Detection of Surface Impurity Phases in High Temperature Superconductors Using Thermally Stimulated Luminescence	D.W. Cooke and M.S. Jahan
DOE S-68,086 S.N.07/311,998 US Pat 4,992,696	Filed 02/17/89 Issued 02/12/91	Apparatus Having Reduced Mechanical Forces for Supporting High Magnetic Fields	M.L. Prueitt, F.M. Mueller and J.L. Smith
DOE S-68,041 S.N.07/330,329 US Pat 5,006,672	Filed 03/29/89 Issued 04/09/91	Apparatus for Storing High Magnetic Fields Having Reduced Mechanical Forces and Reduced Magnetic Pollution	M.L. Prueitt, F.M. Mueller and J.L. Smith
DOE S-68,098 S.N.07/324,264 US Pat 5,015,952	Filed 03/14/89 Issued 05/14/91	Apparatus for Characterizing Conductivity of Materials by Measuring the Effect of Induced Shielding Currents Therein	J.D. Doss
DOE S-71,082 S.N.07/671,231 US Pat 5,102,863	Filed 03/19/91 Issued 04/07/92	Process for Producing Clad Superconducting Materials	R.B. Cass, (HiT$_c$ Superconco, Inc.); K.C. Ott, and D.E. Peterson(LANL)
DOE S-71,084 S.N.07/670,111 US Pat 5,134,360	Filed 03/15/91 Issued 07/28/92	Apparatus and Method for Critical Current Measurements	J.A. Martin and R.C. Dye
DOE S-72,899 S.N.814,355 US Pat 5,252,551	Filed 12/27/91 Issued 10/12/93	Superconductive Articles	X.D. Wu and R.E. Muenchausen
DOE S-72,861 S.N.813,726 US Pat 5,262,394	Filed 12/27/91 Issued 11/16/93	Superconductive Compositions Including Cerium Oxide Layer	X.D.Wu and R.E. Muenchausen
DOE S-72,816 S.N.07/690,725 US.Pat 5,268,646	Filed 04/24/91 Issued 12/07/93	Apparatus and Method for Characterizing Conductivity of Materials	J. D. Doss
DOE S-72,899 S.N.813,727 US Pat 5,270,294	Filed 12/27/91 Issued 12/14/93	Free-Standing Superconductive Articles	X.D. Wu and R.E. Muenchausen
DOE S-72880, S.N.07/774,748 US Pat 5,278,138	Filed 10/11/91 Issued 01/11/94	Aerosol Chemical Vapor Deposition of Metal Oxide Films	K.C. Ott and T.T. Kodas
DOE S-75,081 S.N.08/067,911 US Pat 5,300,486	Filed 05/27/93 Issued 04/05/94	Synthesis of BiPbSrCaCuO Superconductor	W.L. Hults, K.A. Kubat-Martin, K.V. Salazar, D.S. Phillips, and D.E. Peterson
DOE S-80,400 S.N.08/168,331 US Pat 5,434,128	Opened 3/23/92 Filed 12/17/93 Issued 7/18/95	Superconducting Wire	D.A. Korzekwa, J.F. Bingert, D.E. Peterson, and H. Sheinberg
DOE S-75,023 S.N.08/419,485 US.Pat 5,569,641	Filed 3/31/94 Issued 9/10/96	Substrate Heater for Thin Film Deposition	S.R. Foltyn

DOE S-78,394 S.N.08/419,485 US Pat.5,569,641	Opened11/05/93 Filed 04/10/95 Issued 10/29/96	Preparation of Superconducting Bi-2223 Wire	M.G. Smith, J.O. Willis, and D.E. Peterson

5.3 Licenses Granted

Designation	Date	Subject	Issued to
Lic.89-41-0000-1 (Terminated 11/94)	Issued 12/28/88	Apparatus for Characterizing Conductivity of Materials by Measuring the Effect of Induced Shielding Currents Therein	Lakeshore Cryotronics

6. Agreements in Progress (11 Active, all types)

6.1 Superconductivity Pilot Center Agreements

Organization	Topic	PI	Funding (K$)		Dates
			DOE	Partner	
American Superconductor Corporation	Bi2223 Conductors HTS Composite Conductors	Peterson Peterson Willis Willis	170.5 587.1 1500 2300	179 350 950 1100+ 550 FI to LANL	Phase 1: 6/89 Phase 2: 11/91 Phase 3: 2/94-3/96 Phase 4: 3/25/96- 3/24/98
Nuclear Metals / SNL/ AT&T	HTS Co-extrusion	Wallace Bingert	239.2 239.2	760.5 285.0 NM 190.0 ATT	Phase 1: 8/90-8/93 Phase 2: 10/93 - 10/96

6.2 CRADA Agreements

Organization	Topic	PI	Funding (K$)		Dates
			DOE	Partner	
Oxford Superconducting Technology	Bi-2212 HTS Tapes	Smith	290	290	11/93 - 11/96
Lockheed Martin	HTS Current Limiter	Peterson	400	400	11/95-10/97
The BOC Group, Inc.	Superconducting Coated Materials	Peterson	70	70	2/23/96-11/22/96
EURUS Technologies, Inc.	Development of HTS Current Leads and Solders	Peterson	80	140	2/6/96-2/5/97
Eriez Magnetics	HT Superconducting Magnetic Separation	Daugherty	70	52	4/2/96-4/1/97
Power Superconducting Devices, Inc.	Development of HTS Fault Current Limiter	Peterson	250	250	7/96-7/98
The Boeing Company	Superconducting Electromagnetic Devices	Peterson	240	240	9/96-9/97
Lockheed Martin	Bridge-Type Fault Current Limiter	Boenig			11/95-9/98
General Atomics	Bridge-Type Fault Current Limiter	Peterson	In	negotiation	9/98-5/99
3M Corporation	Coated Conductors	Peterson	960	1375	3/97-3/99

6.3 Funds In / Funds Out Agreements

Organization	Topic	PI	Type	Value $K	Dates
EPRI	Thick Films on Flexible Substrates	Wu	Funds In	25 200	7/95-9/95 10/95-10/96

6.4 Other Collaborations

Organization	Topic	PI	Dates
ASC/ ANL/ ORNL/ U. Wisconsin/ NIST-Gaithersburg	Bi-2223 Wire Development (Wire Development Group)	Willis	11/91-
3M/ORNL/ Southwire / Stanford University	Coated Conductor Group	E.Peterson	3/97-3/99
ASC/ ORNL/ LBNL/U. Wisconsin/ Stanford U./ TCSUH/ MIT/ Wright-Patterson AFB/ EPRI	Coated Conductor Development Group	Willis	2/96-
Tektronix	Cryogenic Materials Characterization	Smith	11/89 -
Oak Ridge National Laboratory	HTS Information Exchange	Peterson	In Progress
Argonne National Laboratory	HTS Information Exchange	Peterson	In Progress
Sandia National Laboratories	HTS Information Exchange	Peterson	In Progress
Brookhaven National Laboratory	HTS Information Exchange	Peterson	In Progress

6.5 Staff Exchanges

Organization	Technology Area	Name	Status
Wichita State University	Thallium based HTS Powder Synthesis	P.G. Wahlbeck	In Progress
American Superconductor Corp.	Bi-2223 Wire Development	P. Roberts	In Progress

7. Completed Agreements

7.1 Superconductivity Pilot Center Agreements–Completed

Organization	Topic	PI	Funding (K$) DOE	Funding (K$) Partner	Dates
CPS Superconductor	Metal-Ceramic Interfaces	Mitchell	102.6	80.8	9/89 - 9/90
DuPont / Hewlett-Packard	HTS Electronic Components	Peterson	3777.0	7200.0	10/89 - 10/92
Space Industries, Inc.	Microgravity Processing	Peterson	205.0	247.0	4/90 - 4/91
Cryopower Associates	Improvement of Bulk HTS Materials	Maley Maley	45.2 199.4	60.0 485.9	Phase 1: 2/90 Phase 2: 1/92-1/94
HiT$_c$ Superconco	Optimizing Performance of HTS Cavities and Targets	Wu Wu	136.6 101.9	125.0 100.0	Phase 1: 9/89 Phase 2:12/91
Ceracon, Inc	Bulk HTS Consolidation	Foltyn	237.5	300.0	Phase 1: 6/91

7.2 CRADA Agreements–Completed

Organization	Topic	PI	Funding ($K) DOE	Funding ($K) Partner	Dates
Lockheed Martin	Coil Development	Peterson	330	210	7/93 - 7/96
Plastronic, Inc.	Liquid Cryogen Free HTS Magnet System	Daugherty	100 (+33 Funds In)	67	6/95 - 5/96

7.3 Funds In / Funds Out Agreements-Completed

Organization	Topic	PI	Type	Value $K	Dates
Superconductor Technologies, Inc.	Rutherford Backscattering	Maggiore	Funds In	1.0	5/88 - 5/89
Public Service Company of New Mexico	HTS Theory	Parkin	Funds In	357.1	6/88 - 6/90
EPRI	Assessments for Utilities	Newkirk	Funds In	99.8	6/88 - 6/89
AMP, Inc.	RF Characterization of Tl-based HTS Films	Wallace	Funds In	102.9	1/89 - 5/89
EPRI	Heat Pipe Switch	Merrigan	Funds In	150.0	1/89 - 1/90
Univ. Missouri, Rolla	HTS Fibers	Maestas	Funds Out	111.0	1/89 - 1/90
Bechtel	SMES Systems/Hot to Cold Transitions	Maestas	Funds Out	10.0	2/89 - 2/90
Rocketdyne Corp.,Rockwell, Intl.	Synthesis of Tl HTS	Peterson	Funds Out	95.3	5/89 - 5/90
EPRI	New Families of HTS	Smith	Funds In	120.0	2/90 - 2/92
Underground Systems	Transmission Systems	Stewart	Funds In	48.0	5/91 - 5/92
W.J. Schafer Assoc.	SMES Assessment	Peterson	Funds Out	89.9	5/92 - 5/93
University of California-San Diego	Hydrocode Models	Peterson	Funds Out	63 57	12/92 - 12/93 6/94 - 5/95
Intermagnetics General Corporation	Tl-based HTS coils	Peterson	Funds Out	400	10/92 - 10/96
MIT	Bitter Magnets	Peterson	Funds In	50	5/93 - 4/96
EPRI	ac Loss Measurements in HTS Cables	Maley	Funds In	150	9/5/95-9/4/96
Midwest Super-conductivity, Inc.	IBAD Coated Flexible Substrates	Peterson	SBI Tech Consulting Agreement	5	3/95 - 3/96